

The Phase Behavior of Amphiphilic Surfactants and Polymers: A Dissipative Particles Dynamics Study

Dissertation

zur Erlangung des Grades eines
Doktors der Naturwissenschaften (Dr. rer. nat.)
des Fachbereichs Chemie
der Universität Duisburg-Essen
(Campus Essen)

von

Sarah Gwendolyn Schulz
aus Duisburg

Essen 2004

Vorsitzender: Prof. Dr. V. Buß

1. Gutachter: Prof. Dr. G. Schmid

2. Gutachter: Prof. Dr. G. Jansen

3. Gutachter: Prof. Dr. R. Strey

Mündliche Prüfung: 23.03.2005

Herrn Prof. Dr. Günter Schmid möchte ich an dieser Stelle besonders danken für seine stetige Unterstützung und die Möglichkeit der Promotion an seinem Institut.

Mein ganz herzlicher Dank gilt besonders Herrn Dr. Hubert Kuhn, der mir das interessante und herausfordernde Thema dieser Arbeit zur selbständigen Bearbeitung überlassen hat und mir in zahlreichen Diskussionen beratend zur Seite stand. Außerdem möchte ich mich für die Möglichkeit und die fachliche sowie mentale Unterstützung der zahlreichen Vorträge während der Promotion bedanken.

Der Firma AlCove Molecular Dynamics GmbH, insbesondere Herrn Dr. Hubert Kuhn, danke ich für die Förderung meiner Promotion und die interessanten Einblicke in die chemische Industrie.

Bei Herrn Dr. Christian Mund und Herrn Dr. Joachim Venzmer bedanke ich mich besonders für zahlreiche Diskussionen und Anregungen.

Herrn Dr. Felix Müller danke ich für die tatkräftige Unterstützung dieser Arbeit.

Herrn Prof. Dr. Reinhard Strey möchte ich herzlich für die anregenden Diskussionen, die Unterstützung bei der Veröffentlichung und die Übernahme des Drittgutachtens danken.

Herrn Prof. Dr. Georg Jansen möchte ich herzlich für die Übernahme des Zweitgutachtens danken.

Herrn Dipl.-Chem Ulf Frieske gilt mein besonderer Dank für die Programmierungsarbeiten an der DPD-Software und die Administration der Hardware.

Bei der gesamten Arbeitsgruppe möchte ich mich außerdem für die gute Zusammenarbeit, die nette Atmosphäre und eine schöne Zeit bedanken.

Table of Contents

1	<i>Introduction.</i>	4
2	<i>Theory</i>	8
2.1	Mesoscopic Simulations	8
2.1.1	Dissipative Particle Dynamics	8
2.1.1.1	Introduction	8
2.1.1.2	Integration Scheme	13
2.1.1.3	Calculation of the Surface Tension with DPD	15
2.1.1.4	DPD Units Conversion into Physical Units	15
2.1.2	DPD-Parameter Calculation	18
2.1.2.1	Introduction	18
2.1.2.2	Flory-Huggins Parameter Calculation	23
2.1.2.3	Pair Interaction Energies E_{AB}	25
2.1.2.4	Calculation of the Coordination Number Z	27
2.1.2.5	The COMPASS Force Field	29
2.1.3	Other Mesoscopic Simulation Methods	31
2.1.3.1	Lattice-Boltzmann Method	31
2.1.3.2	Brownian Dynamics	32
2.1.3.3	MesoDyn	33
2.2	Phase Behavior of Amphiphilic Surfactants and Polymers	34
2.2.1	Mesoscopic Structures in Water	34
2.2.2	Microemulsions	38
2.2.3	Surface Tension and Critical Micelle Concentration	41

3	<i>Results and Discussion.</i>	45
3.1	Self-Aggregation in Water	45
3.1.1	Poly (ethylene oxide)- <i>block</i> -poly (propylene oxide)- <i>block</i> -poly (ethylene oxide) in Water	45
3.1.1.1	Simulation Conditions	45
3.1.1.2	Results	48
3.1.2	C ₁₀ E ₄ and C ₁₂ E ₅ in Water	52
3.1.2.1	Simulation Conditions	52
3.1.2.2	Simulation of the Phase Behavior	54
3.1.2.3	Structural Investigation	64
3.2	Self-Aggregation in Water and Oil	67
3.2.1	C ₁₀ E ₄ in Water and n-Decane	67
3.2.1.1	Simulation Conditions	67
3.2.1.2	Microemulsion Formation	72
3.2.1.3	L _α -Phase	76
3.2.1.4	The Boosting Effect – Addition of PEP5-PEO5	80
3.2.1.5	Mechanism of the Boosting Effect	83
3.2.1.6	Addition of PPO5-PEO5	87
3.2.2	Poly (ethylene butylene)- <i>block</i> -poly (ethylene oxide) in Water and Methyl Cyclohexane	89
3.2.2.1	Simulation Conditions	89
3.2.2.2	Results	92

3.3	Self-Aggregation at the Water-Air Surface	95
3.3.1	Simulation of the Surface Tension of $C_{10}E_4$, $C_{12}E_5$ and $C_{12}E_6$	95
3.3.1.1	Simulation Conditions	95
3.3.1.2	Calculation of the Surface Tension	97
3.3.1.3	Calculation of the Minimum Area per Molecule	103
4	<i>Summary</i>	104
5	<i>Outlook</i>	108
6	<i>Appendix</i>	109
6.1	Hard- and Software	109
6.2	Concentration Conversions	109
6.3	Abbreviations and Variables	110
6.4	Molecules	114
6.5	Beads and Interaction Energies	117
6.6	List of Figures	119
6.7	List of Tables	125
7	<i>References.</i>	126

1 Introduction.

Amphiphilic surfactants and polymers are due to their wide range of applications important components in the cosmetic, detergent, food, industry. This great interest is being reflected in the large number of experimental studies¹⁻¹⁵. The simulation of the self-aggregation means an immense step forward in understanding these systems. Complex nanostructured self-assemblies such as colloidal suspensions, micelles, immiscible mixtures, microemulsions, etc., represent a challenge for conventional methods of simulation due to the presence of different time scales in their dynamics. For this reason Molecular Dynamic simulations are not suitable to predict the self-aggregation of such systems. It still has been used to simulate some details¹⁶⁻¹⁸. Therefore, one has to use mesoscopic computer simulation methods. Mesoscopic simulation methods are e. g. Langevin Dynamics, the Lattice-Boltzmann method, MesoDyn, or Dissipative particle Dynamics. Langevin Dynamics, the Lattice-Boltzmann method, and MesoDyn showed all problems – either in the performance as Langevin Dynamics and the Lattice-Boltzmann method or the practicability as MesoDyn. Dissipative Particle Dynamics is the method with the best practicability and performance.

The method used in the present work is Dissipative Particle Dynamics. DPD is a mesoscale simulation technique that has been introduced in order to simulate three-dimensional structures of organic polymer aggregates¹⁹⁻²⁴. In DPD the polymer is modeled using particles, which are interacting by conservative, dissipative and random forces. Particles are not regarded as molecules but rather as droplets or clusters of molecules. With these simplifications bigger systems and longer simulation times can be gained.

The aim of this work was to extend the applicability of DPD. The parameter calculation has been tested previously on a simple, marked amphiphilic surfactant²⁵. The simulation of new systems like microemulsions and the calculation of surface tensions would be of great interest.

The parameter calculation formerly introduced has been tested in this work on more complicated systems: the phase behavior of a poly (ethylene oxide) *-block-* poly (propylene oxide) *-block-* poly(ethylene oxide) triblock copolymer has been investigated. These triblock copolymers show an amphiphilic behavior and their phase behavior in water has not yet been simulated. The similarity of the two blocks of poly (ethylene oxide) and poly (propylene oxide) cause difficulties in the DPD-parameter calculation and demonstrate a challenge for DPD simulations. In this work, the results of the DPD simulation of the phase behavior of the poly (ethylene oxide) *-block-* poly (propylene oxide) *-block-* poly(ethylene oxide) $\text{EO}_{13}\text{PO}_{30}\text{EO}_{13}$ are being presented. The results are in good agreement with the experimental phase diagram^{26,27} and demonstrate the applicability of the DPD parameter calculations even for such complicated systems.

With the application of this technique to simulate the three-dimensional structures of the phase behavior of the non-ionic surfactant C_{10}E_4 , C_{12}E_5 , and C_{12}E_6 it was possible to characterize the structure of the different phases. The bilayer thickness of the lamellar phase and the micellar aggregation number for C_{10}E_4 , C_{12}E_5 and C_{12}E_6 have successfully been calculated with DPD and compared with the experiment²⁸⁻³³. These structural characteristics are in good agreement with the experimental values. The structural correspondence with the experimental structures proved the DPD parameter calculation to be reliable and applicable for many different systems.

After the successful demonstration of the applicability of the DPD simulations to the complicated triblock copolymer-water system and the structural agreement, the primary aim of this work is to investigate microemulsions with the use of DPD. It can provide data for the structure and stability of such microemulsions in order to avoid extensive experimental procedures as well as to obtain experimentally unavailable data.

The second aim of this work is the introduction of air in the DPD model which has so far just treated condensed matter. The treatment of the air-water surface is a completely new task in Dissipative Particle Dynamics and offers a great potential of a large variety of simulations.

Therefore, the first step is to evaluate the method of DPD to obtain reliable data for the structural formation of microemulsions. $C_{10}E_4$ was used as a model surfactant to investigate the structures in microemulsions with DPD because it is used in numerous applications in industry. The formation of microemulsions of the $C_{10}E_4$ /water/n-decane systems is experimentally well known³⁴⁻³⁶.

However, the mesoscopic structure of the microemulsions has not been explored in detail. In this work, surfactant/water/oil as well as surfactant/water/oil/polymer systems are described and simulated with the help of DPD models. The different microemulsions like oil/water-, water/oil-microemulsions as well as a bicontinuous sponge-like phase of $C_{10}E_4$ in water and n-decane were simulated successfully with DPD. The lamellar $L\alpha$ phase of $C_{10}E_4$ in water and n-decane which occurs at high surfactant concentrations was found in remarkable agreement with the experimental phase diagram as published³⁷. The theoretical examination of the so called boosting-effect, which describes the shift of the X-point to lower concentrations³⁴, was possible with Dissipative Particle Dynamics

The so-called X-point, where the one phase region and the three-phase region coincide, is a landmark of the efficiency of a surfactant and its precise prediction is of great value for industrial applications. The aim of all simulations is to get a better understanding of phenomena. The mechanism of the boosting-effect could not be investigated with experimental methods. With the help of DPD simulations it was revealed that the polymer PEP5-PEO5 smoothes the interface. This induces the boosting-effect. A different polymer PPO5-PEO5, with different properties did not induce it. The DPD simulation showed that the replacement of surfactant molecules by the polymer plays just a minor role in the mechanism of the boosting-effect. Hence, DPD has been used to get a better understanding and gave experimentally unavailable insights.

The DPD study of microemulsions of the $C_{10}E_4$ /water/oil system has illustrated that Dissipative Particle Dynamics is suitable to simulate the formation of such structures. This has not been previously reported in the literature.

Respectively, it was not just possible to reproduce the formation of microemulsions of the o/w, w/o as well as the bicontinuous microemulsion of C₁₀E₄ in water and n-decane with an excellent accuracy but to predict the experimentally not investigated emulsion formation of a poly(ethylene butylene)-*block*-poly(ethylene oxide) in water and methyl cyclohexane.

In this work the phase behavior of a poly(ethylene butylene)-*block*-poly(ethylene oxide)diblock copolymer in water and methyl cyclohexane was characterized. The different structures like oil/water-, water/oil phases as well as a bicontinuous microemulsion (a sponge-like phase) of the polymer/water/oil system were effectively simulated with DPD.

The second aim, the introduction of an air-water surface, has been reached by the calculation of the surface tension of C₁₀E₄, C₁₂E₅, and C₁₂E₆ in water. The characteristics of the surface tension of the surfactant –water – air systems could be reproduced. The minimum areas per molecule on the water – air surface have been obtained through the simulations. The qualitative as well as the quantitative investigations have shown that the introduction of an air-water surface into the DPD method has been carried out successfully.

In this work first the systematic testing of the parameter calculation on complicated systems and the comparison of structural quantities is explained. It is followed by the application of the DPD method on microemulsion systems and the introduction of the air-water surface.

Hence, this work proved that the Dissipative Particle Dynamics method is a suitable technique to characterize properties of amphiphilic polymers and surfactants in solution and at the air-water surface. It is easily possible to predict the phase behavior and self-assembly of such compounds and thus to avoid expensive experiments this way by suggesting promising candidates for certain industrial applications.

2 Theory

2.1 Mesoscopic Simulations

2.1.1 Dissipative Particle Dynamics

2.1.1.1 Introduction

Dissipative Particle Dynamics is a “coarse grained” computer simulation method. The properties of condensed matters between atomistic and macroscopic scales can be simulated with this mesoscopic method¹⁹. Dissipative Particle Dynamics already proved to be a reliable tool for the simulation of e.g. polymer melts^{20,21} as well as the simulation of the phase behavior of polymers^{22,23} and surfactants^{24,25,38}, formation of membranes³⁹ and bilayers⁴⁰, calculations of interfacial tensions between two immiscible solvents⁴¹⁻⁴⁴, polymer brushes⁴⁵⁻⁴⁷.

Dissipative Particle Dynamics (DPD) does not calculate the interactions of atoms and molecules, as atomistic models do but between regions of a fluid⁴⁸⁻⁵¹. A liquid in the DPD-model is described by a set of particles of known mass and size, which are interacting through soft potentials. Single atoms lose their identity in a group and represent therefore the average of the atomistic structure. This simulation technique describes the hydrodynamic behavior correctly and is a tool to calculate the behavior of surfactants and polymers in solution on a mesoscopic level.

DPD has been derived from the Molecular Dynamic (MD) and Brownian Dynamic (BD) or Langevin Dynamic (LD) simulation techniques⁵². Dissipative Particle Dynamics is based on the Langevin equation and hence closely related to Brownian Dynamics but conserves momentum and satisfies Newton's third law of motion, which is important to reproduce hydrodynamic behavior. This violation to Newton's law can lead to metastable states that never reach the equilibrium. Due to the reproduced hydrodynamic behavior in DPD this problem cannot occur here which makes DPD superior to Brownian Dynamics. It is also similar to Molecular Dynamics⁵² simulations. Molecular Dynamics simulations

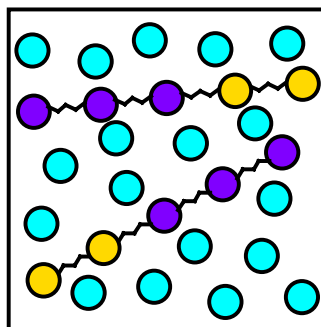
were also used to calculate the phase behavior of surfactants¹⁶⁻¹⁸ but due to the expensive calculations on the atomistic scale it is not comparable with DPD. The small system sizes of about 50 surfactant molecules cannot be compared to the big systems in DPD simulations. The MD calculation is too expensive to start with an arbitrary bead distribution. For the final configuration such as a lamellar phase, the starting configuration has to be set to a bilayer. This is a great disadvantage towards Dissipative Particle Dynamics which is superior to Molecular Dynamics simulation for the calculation of the self-assembly of condensed systems.

Dissipative Particle Dynamics was first introduced by Hoogerbrugge und Koelman^{54,53}. It allows the simulation of big systems of complex liquids in long time scales even up to microseconds. DPD simulations from S. Jury *et al.*⁵⁵ proved that the experimental phase behavior of non-ionic surfactants can be reproduced.

In DPD the fluid is modeled with point particles that interact through conservative, dissipative, and random forces. The forces due to individual solvent molecules are lumped together to yield an effective friction and a fluctuating force between moving particles. These point particles are not regarded as the fluid molecules but rather as droplets or clusters of molecules. Figure 1 shows the DPD-model of a polymer in water.

The hydrophobic chain of the polymer is represented by purple beads, which are connected by harmonic springs and the hydrophilic chain is represented by yellow beads which are as well connected by harmonic springs. Water is represented by one bead (blue).

Figure 1. Schematic DPD-model of an amphiphilic polymer in water.



Dissipative Particle Dynamics is based on the conventional Molecular Dynamics simulation method. A system which contains pair-wise interacting particles, moves through the space in discrete time steps dt . Its dynamical evolution can be described by Newton's laws of motion:

$$\frac{dr_i}{dt} = v_i, \frac{dv_i}{dt} m_i = F_i \quad 1$$

Where r_i is the coordinate of the particle i , m_i its mass, t the time, v_i the velocity and F_i the total force on the beads (Equation 1).

In DPD the fluid is modeled with point particles that interact through conservative F^C , dissipative F^D , and random forces F^R (Equation 2):

$$F_i = \sum_{i \neq j} \left(F_{ij}^C + F_{ij}^D + F_{ij}^R \right) \quad 2$$

The forces are pair-wise additive and the sum between all DPD-particles (beads) is calculated within a *cut-off* radius r_c .

The conservative component is taken to be linear up to a cut-off radius in particle separation r_c , and zero outside of this (Equation 3).

$$F_{ij}^C = \begin{cases} a_{ij} \cdot \hat{r}_{ij} \cdot \left(1 - \frac{r_{ij}}{r_c} \right) & (r_{ij} < r_c) \\ 0 & (r_{ij} > r_c) \end{cases} \quad 3$$

Where $\hat{r}_{ij} = r_{ij} / |r_{ij}|$, and a_{ij} is the repulsion parameter (DPD-parameter).

Beads that belong to the same molecule are connected by harmonic springs and the interactions are described by the force F_{ij}^S :

$$F_{ij}^S = K_s \cdot r_{ij} \quad 4$$

The spring constant K_s has to be chosen that the average distance between two connected beads correlates with the maximum of the radial distribution function. The flexibility of the chains decreases with the increase of the spring constant⁵⁶.

The dissipative force F_{ij}^D is proportional to the relative velocities ($v_{ij} = v_i - v_j$) of two beads and is described by Equation 5:

$$F_{ij}^D = -\gamma_{DPD} \cdot \omega^D(r_{ij}) \cdot (\hat{r}_{ij} \cdot \hat{v}_{ij}) \cdot \hat{r}_{ij} \quad 5$$

If particle j moves into the opposite direction of particle i , the scalar product $\hat{r}_{ij} \cdot \hat{v}_{ij}$ is positive and the particles i and j attract each other with the force (F_{ij}^D), which is proportional to v_{ij} . If both particles are moving into the same direction the attraction changes to a repulsion and acts as to reduce their relative momentum. The DPD coefficient γ_{DPD} in Equation 5 controls the magnitude of the dissipative force and can be seen as a friction constant.

The random force F^R provides an energy input into the system (Equation 6) and builds together with the dissipative force a thermostat .

$$F_{ij}^R = \sigma \cdot \omega^R(r_{ij}) \cdot \theta_{ij} \cdot \hat{r}_{ij} \quad 6$$

σ is the amplitude of the statistical noise, θ a random variable, which is generated from the Gaussian distribution independently for each particle per time step. ω^D and ω^R are the weight functions and depend on the particle distances.

Español and Warren⁵⁷ proved that the DPD system is being simulated in the canonical NVT ensemble if the two weight functions are chosen as shown in Equation 7:

$$\gamma_{DPD} = \frac{\sigma^2}{2k_B T} \quad \text{and} \quad \omega^D(r_{ij}) = [\omega^R(r_{ij})]^2 \quad 7$$

where k_B is the Boltzmann constant und T the temperature.

Equation 7 describes the so called *fluctuation-dissipation theorem* for the Dissipative Particle Dynamics method and sets the DPD temperature to $k_B T = \sigma^2 / (2\gamma_{\text{DPD}})$. It makes the dissipative and random force to interact and build a thermostat and therefore remain in the thermodynamic equilibrium. The particular functional forms of the friction and random forces ensure that all forces obey action-equals-reaction, and therefore the model conserves momentum. This is essential for recovering the correct “hydrodynamic” (Navier-Stokes) behavior on sufficiently large length and time scales.

2.1.1.2 Integration Scheme

The integration scheme in Dissipative Particle Dynamics is based on Newton's law of motion. For a system consisting of N particles the Equation of motion is solved with a numerical integration scheme. A particle i with the mass m_i follows Newton's second law (Equation 8):

$$F_i(t) = m_i \cdot a_i(t) \tag{8}$$

where F_i is the applied force and a_i the acceleration of the particle. The time dependent differential equation describes the dynamic behavior:

$$\frac{\partial^2 r_i}{\partial t^2} = \frac{F_i}{m_i} \tag{9}$$

With the knowledge of the coordinates, velocities and forces of a particle it is possible with the equations of motion to calculate the coordinates and velocities at any future point of time.

Numerical mathematics provides a great range of procedures to integrate the equation of motion⁵⁸. A capable procedure for molecular simulations has to provide fast calculations, large time steps, and has to follow the energy conservation equation. The commonly used algorithm for DPD-simulations is a modified *velocity-verlet* algorithm^{59,60}.

The temperature control of a DPD simulation is so far an unsolved problem. Español and Warren showed in their theoretical work that the conservative and dissipative forces have to fulfill the *dissipation-fluctuation theorem* (Equation 7) to make the simulation with a thermodynamically defined temperature possible.

For the original Hoogerbrugge-Koelman algorithm⁵⁴ (an Euler-type algorithm) Marsh und Yeomans⁶¹ derived the expression of the equilibrium temperature of an ideal gas and found that the DPD temperature is always greater than the thermodynamic temperature of the

system. To prevent this increase in temperature Groot and Warren⁶² suggested a modified integration algorithm. Different integration schemes have been discussed by Novik and Coveney⁶³. The best results for DPD simulations were obtained with the algorithm suggested by Groot and Warren ($\lambda=1/2$), a modified *velocity-verlet* algorithm⁶⁴.

$$\begin{aligned} r_i(t + \Delta t) &= r_i(t) + \Delta t v_i(t) + \frac{1}{2}(\Delta t)^2 f_i(t), \\ \tilde{v}_i(t + \Delta t) &= v_i(t) + \lambda \Delta t f_i(t), \\ f_i(t + \Delta t) &= f_i(r_i(t + \Delta t), \tilde{v}_i(t + \Delta t)) \\ v_i(t + \Delta t) &= v_i(t) + \frac{1}{2} \Delta t f_i(t) + f_i(t + \Delta t) \end{aligned} \tag{10}$$

This algorithm, in opposite to the non-modified version of the *velocity-verlet* algorithm, contains a calculation scheme analogous to the predictor-corrector procedure⁶⁵ with an estimated value for the velocity $\tilde{v}_i(t + \Delta t)$ at a time $(t + \Delta t)$ to calculate the total force $f_i(t + \Delta t)$ at that time. In the last integration step the velocity $v_i(t + \Delta t)$ is being corrected. The theoretical work showed that the value of $\lambda=1/2$ leads to a better temperature control in DPD simulations^{60,65,66}, hence this algorithm and value were used in this work.

2.1.1.3 Calculation of the Surface Tension with DPD

In computer simulations the surface tension, of the surface perpendicular to the x -axis of the system is being computed through Equation 11: The pressure tensors⁶⁷, $p_{xx}(x)$, $p_{yy}(x)$ and $p_{zz}(x)$, of the simulation box define the calculated surface tension σ_{DPD} .

$$\sigma_{DPD} = \int p_{xx}(x) - \frac{1}{2}(p_{yy}(x) + p_{zz}(x)) dx = A^{-1} \sum_{i < j} \left(F_{ij,x} x_{ij} - \frac{1}{2} (F_{ij,y} y_{ij} + F_{ij,z} z_{ij}) \right) \quad 11$$

A is the area in the yz -plane, p the pressure, x, y, z are the cartesian coordinates and F_{ij} is the force between the two particles i and j .

The pressure tensors $p_{xx}(x)$, $p_{yy}(x)$ and $p_{zz}(x)$ can be calculated from Equation 12⁶⁷:

$$p_{xx}(r) = k_B \cdot T \cdot \rho(r) \cdot \delta_{xx} - \frac{1}{2} \cdot \sum_i \sum_{j \neq i} \left\langle \frac{r_{ijx}}{r_{ij}} \frac{dv(r'_{ij})}{dr_{ij}} \int_{C_{ij}} d'_x \delta(r - r') \right\rangle \quad 12$$

where r_{ij} is the position of particle i relative to particle j , k_B is the Boltzman constant, T the temperature, $\rho(r)$ the probability distribution function of r , v the velocity and C_{ij} any contour joining bead i and j . The simplest choice of the contour C_{ij} is to use the straight line between the two particles.

2.1.1.4 DPD Units Conversion into Physical Units

All DPD units can be easily converted into physical units⁶⁸ The conversion from DPD units to physical units is in principle based on the cut-off radius r_c as introduced in Chapter 2.1.1.1. The cut-off radius r_c defines the box side lengths a , b , and c , the box volume V_{box} and the box surface area A_{box} .

The cut-off radius can be calculated through Equation 13⁶⁸:

$$r_c = \sqrt[3]{V(\textit{smallest}) \cdot X \cdot \rho_{DPD}} \quad 13$$

The molecular volume of the smallest bead $V(\textit{smallest})$ in this work is the molecular volume of water $V(W)$. It has been determined experimentally and through Molecular Dynamics simulations to 30\AA^3 . The number of these smallest bead in one surfactant or oil bead X can be calculated with Equation 14.

$$X = \frac{1}{n} \cdot \sum_A^Z n_A \cdot K(A) \quad 14$$

where n is the total number of beads in the molecule and n_A the number of beads A in this molecule.

The relation $K(A)$ between the calculated volume of water $V_c(W)$ and the calculated volume of the other beads $V_c(A)$ etc is defined by Equation 15:

$$K(A) = \frac{V_c(A)}{V_c(W)} \quad 15$$

Equation 16 shows the side lengths of the simulation box a , b and c calculated by multiplying the DPD side lengths a_{DPD} , b_{DPD} and c_{DPD} with the cut-off radius r_c :

$$a = a_{DPD} \cdot r_c, \quad b = b_{DPD} \cdot r_c, \quad \text{and} \quad c = c_{DPD} \cdot r_c \quad 16$$

The surfaces area of the box A_{box} is defined in an analogous way (Equation 17).

$$A_{box} = a_{DPD} \cdot b_{DPD} \cdot r_c^2 \quad 17$$

as well as the box volume V_{box} in Equation 18:

$$V_{box} = a_{DPD} \cdot b_{DPD} \cdot c_{DPD} \cdot r_c^3 \quad 18$$

The multiplication of the time step size $t_{step}=0.5$ with the number of simulation steps n_{step} gives the simulation time t_{DPD} in DPD units (Equation 19)

$$t_{DPD}(n_{step}) = t_{step} \cdot n_{step} \quad 19$$

The simulation time in DPD units t_{DPD} can be converted into physical time t through Equation 20,

$$t(n_{step}) = t_{DPD}(n_{step}) \cdot r_c \cdot 10^{-9} \cdot \sqrt{\frac{m \cdot au}{k_B \cdot T}} \quad 20$$

while the average mass of all beads m is defined through Equation 21:

$$m = \frac{\sum_A^Z m(A)}{n} \quad 21$$

The calculated surface tension σ_{DPD} can be converted from DPD units to physical units σ_{phys} (mN m^{-1}) by applying Equation 22⁴⁴:

$$\sigma_{phys} = \frac{k_B \cdot T}{r_c^2} \cdot \sigma_{DPD} \quad 22$$

where k_B is the Boltzmann constant, T the temperature and r_c the cut-off radius.

2.1.2 DPD-Parameter Calculation

2.1.2.1 Introduction

The *dissipation fluctuation theorem* shows that the dissipative constant γ_{DPD} and the constant of the statistical noise σ are connected. Therefore, there is just one variable in the DPD simulation changeable. Groot and Warren⁶² proved the integration scheme to be unstable if the amplitude of σ exceeds a value of 8. They also proved that the system quickly relaxed in a temperature range from $k_B T = 1$ and $k_B T = 10$ for $\sigma = 3$. For a reliable simulation the statistical noise σ should not exceed 3, which limits the choice of the dissipative coefficient and the simulation temperature.

Groot und Warren⁶² demonstrated that for a simulation time step of $\Delta t = 0,04$, $\sigma = 3$ and the modified *velocity-verlet* algorithm ($\lambda=1/2$) a stable system could be found at reasonable simulation times and with a quickly relaxed temperature equilibrium. Marsh und Yeomans³¹ observed that the temperature of a DPD-system becomes instable at time steps Δt greater than a critical value Δt_c .

$$\Delta t_c = \frac{2 \cdot A_1}{\rho \cdot A_1^2 + A_2} \quad 23$$

with

$$A_1 = \frac{\gamma_{DPD}}{m \cdot d} \cdot [\omega_D] \quad \text{and} \quad A_2 = \frac{2 \cdot \gamma_{DPD}^2}{m^2 \cdot d} \cdot [\omega_D^2] \quad 24 \text{ and } 25$$

ρ is the density, γ_{DPD} the friction coefficient, m the mass of the DPD-particle (for simplicity set to 1) and d the spatial dimensions of the system. The magnitude of the critical time step can be obtained through Equations 23-25 for DPD simulation with a distinct parameter set.

Since the dissipative constant γ_{DPD} and the constant of the statistical noise σ are not arbitrarily changeable the remaining parameter is the repulsion parameter a_{ij} .

The use of “soft-potentials” for F^C in the DPD method makes larger time steps possible than in common molecular dynamics simulations. DPD particles do not represent atoms but liquid elements. The use of “soft potential” was introduced by Forrest and Sutter⁶⁴. The suggested procedure starts with the calculation of the atomistic interactions, which are later on substituted with effective potentials between the centers of mass of the particles. These effective potentials were systematically determined through the average of the potential field of fast fluctuating atoms in short time intervals.

The forces, on the atomistic level in physical systems, are represented in DPD by the conservative force F^C which depends on the repulsion or DPD parameter a_{ij} . In order to get a correct description of the thermodynamic state, the density fluctuations of the liquid have to be exact. The dimensionless reciprocal compressibility represents the macroscopic state correctly if it is defined as shown Equation 26:

$$k^{-1} = \frac{1}{nk_B T k_T} = \frac{1}{k_B T} \left(\frac{\partial p}{\partial n} \right)_T \quad 26$$

n is the numerical density of the molecules, k_T is the isothermal compressibility of the liquid.

Groot und Warren⁶² proved that for small densities of DPD liquids (3 to 10 particles per volume unit) and interaction parameter of $a=15$ to 30 that the Equations of state of the DPD liquid can be described as:

$$p = \rho k_B T + \alpha a \rho^2 \quad 27$$

ρ is the density of the DPD liquid, k_B the Boltzmann constant, T the absolute temperature, a the interaction parameter, and α ($0,101 \pm 0,001$) a constant. Water at room temperature (300K) has a dimensionless compressibility of $k^{-1}=15,9835$. Equation 28 describes the equation of state after differentiation:

$$\left(\frac{\partial p}{\partial \rho}\right) = k_B T + 2\alpha a \rho \quad 28$$

Equation 28 and 27 compared show that the interaction parameter of pure liquids (a_{AA}) is reciprocal to the density of DPD liquids:

$$a_{AA} = \frac{75k_B T}{\rho} \quad 29$$

Equation 29 makes the calculation of the DPD interaction parameter of equal beads possible.

Furthermore the calculation of the interaction parameter a_{AA} of different beads has to be carried out for the DPD simulation. The Flory-Huggins parameter χ can be used in polymer chemistry to describe the interaction between polymer segments⁷⁰.

The Flory-Huggins lattice theory describes the phase separation of a thermodynamic mixture of a binary system. The free mixing energy F_{mix} according to the Flory-Huggins theory for a binary system which contains the two components A and B equals:

$$\frac{F_{mix}}{k_B T} = \frac{\phi_A}{N_A} \ln \phi_A + \frac{\phi_B}{N_B} \ln \phi_B + \chi \phi_A \phi_B \quad 30$$

ϕ_A and ϕ_B are the mole fractions of the components A and B, N_A and N_B are the numbers of monomer segments in each molecule A and B, and χ is the Flory-Huggins interaction parameter. For a completely occupied lattice follows: $\phi_B + \phi_A = 1$.

The equilibrium state of the mixture can be obtained by a minimization of the free mixing energy with $\frac{\partial F}{\partial \phi_A} = 0$ and $N_A = N_B$. The localization of the minima can be obtained through

Equation 31:

$$\chi N_A = \frac{\ln[(1-\phi_A)/\phi_A]}{1-2\phi_A} \quad 31$$

A phase separation occurs if the χ parameters changes from negative to positive. The critical value of χ can also be determined by searching for a minimum of the free mixing energy. At this critical χ value the first and second derivative of the free mixing energy have to be zero.

Equation 32 describes this critical point:

$$\chi^{crit} = \frac{1}{2} \left(\frac{1}{\sqrt{N_A}} + \frac{1}{\sqrt{N_B}} \right)^2 \quad 32$$

The density of the free energy f_v of a one component DPD liquid equals:

$$\frac{f_v}{k_B T} = \rho \ln \rho - \rho + \frac{\alpha \rho^2}{k_B T} \quad 33$$

and for a two component system:

$$\frac{f_v}{k_B T} = \frac{\rho_A}{N_A} \ln \rho_A + \frac{\rho_B}{N_B} \ln \rho_B - \frac{\rho_A}{N_A} - \frac{\rho_B}{N_B} + \frac{\alpha(a_{AA}\rho_A^2 + 2a_{AB}\rho_A\rho_B + a_{BB}\rho_B^2)}{k_B T} \quad 34$$

For $a_{AA}=a_{BB}$, and $x = \rho_A/(\rho_A + \rho_B)$ and the assumption that $\rho_A + \rho_B = constant$ Equation 34 can be transferred into Equation 35:

$$\frac{f_v}{(\rho_A + \rho_B)k_B T} \approx \frac{x_A}{N_A} \ln x_A + \frac{(1-x)}{N_B} \ln(1-x) + \chi \cdot x \cdot (1-x) + K \quad 35$$

where K is a constant.

The definition of χ is shown in Equation 36:

$$\chi = \frac{2\alpha(a_{AB} - a_{AA})(\rho_A + \rho_B)}{k_B T} \quad 36$$

The Flory-Huggins free mixing energy in Equation 30 and the density of the free energy in Equation 35 correspond if the χ parameter is proportional to the DPD interaction parameter a as shown in Equation 36.

Groot and Warren determined a linear dependency between the Flory-Huggins interaction parameter χ and the DPD interaction parameter a_{AB} :

$$a_{AB}(T) = a_{AA} + K_D(\rho_{DPD}) \cdot \chi_{AB}(T) \quad 37$$

The proportional constant $K_D(\rho_{DPD})$ is not linearly depending on the density ($K_D(3)=3,497$, $K_D(5)=1,451$).

According to Equation 28 and 37 for the repulsion between different DPD-particles at a DPD temperature $k_B T = 1$ and a DPD density of $\rho_{DPD} = 3$ follows (Equation 38):

$$a_{AB}(T) = 25 + 3.497 \cdot \chi_{ij}(T) \quad 38$$

where a_{AB} (repulsion parameter between particles of different bead types) are linearly related to the Flory-Huggins interaction parameter χ ⁵⁷ Therefore the knowledge of the Flory-Huggins parameters implies the knowledge of the DPD interaction parameters.

2.1.2.2 Flory-Huggins Parameter Calculation

The Flory-Huggins parameter χ can be obtained by different methods, for example through the interpolation of experimental data (solubilization parameters, heat of vaporization, etc.) or computer simulations. The calculation of χ can be performed by Quantitative-Structure-Activity-Relationship (QSAR) calculations, Molecular Dynamics (MD) simulations, or Monte Carlo (MC) simulations.

The QSAR methods correlates experimentally known data with the structure of the compounds. With theses information the prediction of χ of unknown systems can be performed⁷¹.

The free energy can be obtained with MD simulations through the cohesive energies of the two components separately and the mixture of both. Through the comparison of the cohesive energies of the components in the gas and condensed phase the χ parameter can be calculated by calculating the free mixing energy. In the Molecular Dynamics simulation all atomistic details as well as hydrogen bonds are taken into account, hence MD provides the most accurate χ parameter calculation. The disadvantage of this method is long simulation times based on the complex systems on the atomistic scale.

The method used in this study is the MC simulation of the χ parameter. This method is based on the calculation of the free mixing energy of a two-component system in the Flory-Huggins theory. The χ parameter of a mixture of two components A and B represents the repulsive energy of the molecule pair AB and it is assumed that this pair AB is just affected by the average energetic field of the bulk phase. Therefore the pair contact interaction energies E_{AB} have to be calculated with Monte Carlo computer simulations. The loss in accuracy in comparison to the Molecular Dynamics simulation is countervailed by the shorter simulation times.

The Flory-Huggins parameter χ was defined as in Equation 39⁷⁰:

$$\chi = \frac{Z \cdot \Delta E_{AB}}{RT} \quad 39$$

Z is the coordination number and ΔE_{AB} the differential pair interaction energy⁷² as shown in Equation 40:

$$\Delta E_{AB} = \frac{1}{2}(E_{AB} + E_{BA}) - \frac{1}{2}(E_{AA} + E_{BB}) \quad 40$$

As the result of their definition the two energies E_{AB} and E_{BA} have the same value but due to the statistics different values may be calculated. The combination of modified Flory-Huggins theory and Monte Carlo simulations yields a method for the calculation of interaction parameters.

The algorithm was first introduced by Fan *et al.*⁷² In opposite to the original Flory-Huggins theory a *off-lattice* calculation is used, which implies that the molecules are not arranged in a regular lattice. The coordination numbers are calculated for all different pairs and the temperature dependency of χ is taken into account by fitting to various analytical models (e.g. $\chi(T) = A + B \cdot T + C / T^2$).

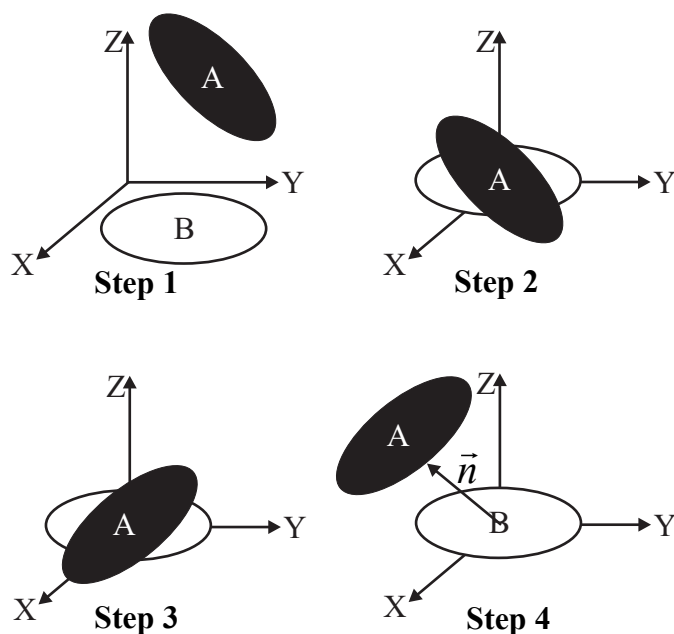
All calculations were carried out using the COMPASS force field (Condensed-Phase Optimized Molecular Potentials for Atomistic Simulation Studies)⁷³⁻⁷⁵, which is especially parameterized to model fluids.

According to Equation 39 and 40 the coordination number Z and the pair interaction energies E_{AA} , E_{BB} , E_{AB} and E_{BA} have to be calculated to first obtain χ and then a_{AB} .

2.1.2.3 Pair Interaction Energies E_{AB}

The pair interaction energies are calculated with the pair method, which is based on the creation of thousands of different configurations of the molecular pairs AA , BB , AB and BA with Monte Carlo Simulations. The energies of all pairs are calculated as shown in Figure 2. The procedure used in this *excluded-volume constraints* method follows a modified Blanco algorithm^{76,77}.

Figure 2. Pair interaction energy calculation.



In the first step the geometries of the two molecules A and B are calculated and then in the second step moved into the origin. The orientation of molecule A in step three is defined through three randomly chosen Euler angles. In the final step 4 molecule A is moved along a defined vector \vec{n} so the two *van-der-Waals* surfaces do not overlap. The two molecules are now slid apart until an energy minimum has been found. Repeating

these steps several thousand times gives a great number of possible pair interaction energies and a probability function is formed. $P(E_{AB})$.

The influence of temperature is taken into account through the Boltzmann distribution law. Equation 41 shows the calculation of the average Energy E_{AB} in dependence on the temperature $\langle E_{AB}(T) \rangle$.

$$\langle E_{AB}(T) \rangle = \frac{\int dE_{AB} P(E_{AB}) E_{AB} e^{\left(\frac{-E_{AB}}{k_B T}\right)}}{\int dE_{AB} P(E_{AB}) e^{\left(\frac{-E_{AB}}{k_B T}\right)}} \quad 41$$

The Boltzmann distribution of the pair contact energies E_{AA} , E_{AB} , E_{BA} and E_{BB} was obtained through the Monte Carlo simulations as described in Figure 2.

2.1.2.4 Calculation of the Coordination Number Z

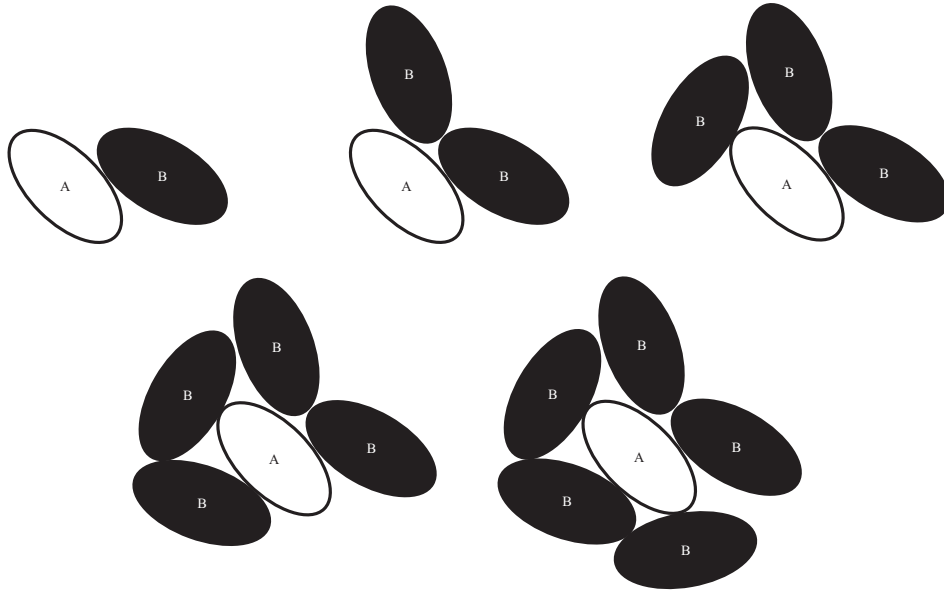
The next step, after the calculation of the pair interaction energies, to obtain the Flory-Huggins parameter as described in Equation 39 is the calculation of the coordination number Z for all possible molecular pairs, where the overlap of van-der-Waals surfaces is not allowed. For the coordination number calculation four different pairs are possible as listed in Table 1:

Table 1. Possibilities of Coordination numbers Z .

Coordination Number	Central Molecule	Neighbor Molecules
Z_{AA}	Component A	Component A
Z_{AB}	Component A	Component B
Z_{BA}	Component B	Component A
Z_{BB}	Component B	Component B

This simulation method creates clusters of molecules where as many neighbors are packed around a central molecule as possible, without an overlap of the van-der-Waals surfaces. Figure 3 shows an example of the coordination number calculation. The molecules are represented by their van-der-Waals surface and the different steps are depicted. An overlap of the van-der-Waals surfaces has to be avoided, while all molecules (black) need to have contact to the van-der-Waals surface of the central molecule (white). The first picture shows the addition of one molecule, then two three, four and five. After five molecules are surrounding the central molecule the addition of one more molecule without an overlap of the van-der-Waals surfaces is impossible. Therefore, this configuration has the coordination number of 5. The algorithm for this calculation was published by Fan *et al*72.

Figure 3. Coordination Number Calculation Z_{AB} .



The average coordination numbers obtained through several thousands of different configurations, together with the calculated average Energy $\langle E_{AB}(T) \rangle$ (in dependence on the temperature) (Equation 41) can now be used to calculate the temperature depended parameter, the mixing energy $E_{mix}^{AB}(T)$ (Equation 42):

$$E_{mix}^{AB}(T) = \frac{[Z_{AB} \langle E_{AB}(T) \rangle + Z_{BA} \langle E_{BA}(T) \rangle - Z_{AA} \langle E_{AA}(T) \rangle - Z_{BB} \langle E_{BB}(T) \rangle]}{2} \quad 42$$

Finally the χ parameter can be calculated (Equation 43):

$$\chi(T) = \frac{E_{mix}^{AB}(T)}{RT} \quad 43$$

The inaccuracy caused by calculating the mixing energy of condensed matters through pair contact energies is compensated by averaging several thousands of configurations⁷².

2.1.2.5 The COMPASS Force Field

The Monte Carlo calculations for the pair interaction energies and coordination numbers are based on force field calculations.

The calculation with force field methods is based on the parameterization of inter atomic interactions. The quality of these parameters controls the accuracy of the calculation results^{78,79}. Atoms in different chemical environments are divided into different atom types and the direct electron-electron and electron-nucleus interactions are neglected.

In force field methods the energy is written by a parametric function of the nuclear positions. The parameters are fitted to experimental or higher level computational data. The molecules are modeled as atoms held together by bonds. The bonds are represented by bond potentials in the force field e.g. potentials for bond lengths, angles and torsion angles. Inter molecular interactions are calculated by potentials described through van-der-Waals and Coulomb forces. The total potential energy E_{total} is the sum of all bond potentials (E_{intra}) and non-bond potentials (E_{inter}):

$$E_{total} = E_{intra} + E_{inter} \quad 44$$

Modern class 2 force fields include additional coupling terms, which describe the coupling between bond lengths and bond angles as well as between bond angles and torsion angles. These additional coupling terms improve the accuracy of the force field and the application of the force field parameters on new chemical environments.

The choice of the right force field is of great importance for the DPD interaction parameter calculation. The force field used for the Monte Carlo simulations was the COMPASS force field⁷³. The COMPASS (condensed-phase optimized molecular potentials for atomistic simulations studies) force field is the most accurate for calculations of molecular interactions in solvent systems. It is a class 2 force field and was parameterized with *ab initio* and empirical methods. The valence parameters as well as atomistic partial charges were derived from *ab initio* data. The van-der-Waals parameters were obtained from experimental cohesive energies and equilibrium densities of liquids.

Equation 45 describes the functional form of the terms to calculate the total energy E_{total} :

$$\begin{aligned}
 E_{total} = & \underbrace{\sum_b [k_2(b-b_0)^2 + k_3(b-b_0)^3 + k_4(b-b_0)^4]}_1 + \\
 & \underbrace{\sum_\theta [k_2(\theta-\theta_0)^2 + k_3(\theta-\theta_0)^3 + k_4(\theta-\theta_0)^4]}_2 + \\
 & \underbrace{\sum_\phi [k_1(1-\cos\phi) + k_2(1-\cos 2\phi) + k_3(1-\cos 3\phi)]}_3 + \\
 & \underbrace{\sum_{\mathcal{G}} [k_2\mathcal{G}^2]}_4 + \underbrace{\sum_{b,b'} [k(b-b_0)(b'-b_0')]}_5 + \underbrace{\sum_{b,\theta} [k(b-b_0)(\theta-\theta_0)]}_6 + \\
 & \underbrace{\sum_{b,\phi} [(b-b_0)(k_1\cos\phi + k_2\cos 2\phi + k_3\cos 3\phi)]}_7 + \\
 & \underbrace{\sum_{\theta,\phi} [k(\theta-\theta_0)(\theta'-\theta'_0)(k_1\cos\phi + k_2\cos 2\phi + k_3\cos 3\phi)]}_8 + \underbrace{\sum_{\theta,\phi} [k(\theta-\theta_0)(\theta'-\theta'_0)\cos\phi]}_9 + \\
 & \underbrace{\sum_{i,j} \frac{q_i q_j}{r_{ij}}}_{10} + \underbrace{\sum_{i,j} E_{ij} \left[2 \left(\frac{r_{ij}^0}{r_{ij}} \right)^9 - 3 \left(\frac{r_{ij}^0}{r_{ij}} \right)^6 \right]}_{11}
 \end{aligned} \tag{45}$$

The first terms 1-4 represent the interactions depending on the internal coordinates as bonds b (term 1), angles θ (term 2), torsion angles ϕ (term 3), and out-of-plane vibrations \mathcal{G} (term 4). The next five terms (5-9) are the coupling terms including the combination of internal coordinates as bond-bond b - b' (term 5), bond-angle b - θ (term 6), bond-torsion angle b - ϕ (term 7), angle-angle θ - θ' , and torsion angle-angle ϕ - θ (term 8 and 9) coupling. Term 10 and 11 represent the non-bond interactions. Term 10 describes the electrostatic interactions with a Coulomb function and term 11 the van-der-Waals interactions with a Lennard-Jones-9-6-potential⁸⁰.

The validation studies based on 178 isolated molecules, 102 liquids and 69 molecular crystals demonstrated that the COMPASS force field is capable to predict different properties of great number of isolated molecules as well as condensed matters^{50,74}.

2.1.3 Other Mesoscopic Simulation Methods

Besides the Dissipative Particle Dynamics method which has been used for the present studies there exist many more coarse-grained mesoscopic simulation methods to model the self-assembly of molecules in the condensed phase^{19,64}. The aim of all mesoscopic simulation methods is to provide a computationally cheap representation of mesoscopic fluids. In this chapter three other methods will be briefly introduced: the Lattice-Boltzmann method, the MesoDyn method and the Brownian Dynamics method.

2.1.3.1 Lattice-Boltzmann Method

The Lattice-Boltzmann method is, as the name suggests, a lattice scheme⁸¹⁻⁸³. It is based on the lattice gas cellular automaton model of a fluid⁸⁴. The fluid in such a model is represented by a regular lattice. Every lattice point has n nearest neighbors and there can be at most one particle moving to any given nearest neighbor. In the first simulation step a particle moves along its link from its original lattice point to the corresponding link to the nearest-neighbor lattice point. The next simulation step is the collision during which the total number of particles and the total momentum on a given lattice is maintained. Apart from this constraint all particles can change their velocities. With this simple model, it is possible to reproduce hydrodynamic behavior and it can be used for many applications⁸⁵. But due to the simplicity of lattice model this method suffers from a number of practical problems.

2.1.3.2 Brownian Dynamics

Brownian Dynamics (BD) or Langevin Dynamics (LD) is the basis of Dissipative Particle Dynamics and therefore closely related to this method. It is being used to simulate e.g. polymer solutions⁸⁶. The method of Brownian Dynamics computer simulations has been first introduced by Ermak in 1976^{87,88}. The relevant dynamic equation is called the Langevin equation of motion⁸⁹:

$$m \frac{d^2 r}{dt^2} = -\zeta \frac{dr}{dt} + F_{intra} + F_{random} \quad 46$$

where m is the mass, r the coordinates, t the time and F_{intra} the intra molecular force, F_{random} a random force and ζ the friction coefficient. It defines that the total force $m \frac{d^2 r}{dt^2}$ equals the sum of a frictional or dissipative force $-\zeta \frac{dr}{dt}$, the force of the intramolecular interactions F_{intra} and a random force F_{random} . It is the equivalent to Equation 2 in DPD. However, in Brownian Dynamics the frictional and random forces do not conserve momentum and the only property that is conserved is the total number of particles. In DPD the random and dissipative force are connect by the *fluctuation-dissipation theorem*³⁸, which ensures that the forces obey the principle action=equals=reaction. This is essential to reproduce hydrodynamic behavior. Groot *et al.*⁹⁰ compared the results of Langevin Dynamics and DPD simulations of the phase formation of a block copolymer melt. While the DPD simulations reproduce the experimental lamellar phase, the system in the Brownian Dynamics simulation remains in a metastable state due to the missing hydrodynamic behavior.

2.1.3.3 MesoDyn

The basic idea of the MesoDyn method differs from the other introduced mesoscopic simulation techniques. It is not particle-based but a density functional theory, where the free energy F of an inhomogeneous liquid is a function of the local density function ρ_{local} . From the free energy, all thermodynamic functions can be derived so that for instance phase transitions can be investigated as a function of the density distribution in the system

The dynamic mean-field density functional method used in MesoDyn is based on the generalized Ginzburg-Landau theory⁹¹⁻⁹⁴ for conserved order parameters. The numerical calculation involves time-integration of functional Langevin equations. The thermodynamic driving forces are obtained from a Gaussian chain molecular model.

The MesoDyn method has been applied e.g. to polymer melts⁹⁵⁻⁹⁷ and the simulation of the phase behavior of amphiphilic polymers in solution^{98,99}.

The input parameters for the MesoDyn simulations can be calculated e.g. from Scatchard-Hildebrand solubility parameters^{100,101}. MesoDyn gives comparable results to DPD in mesoscopic simulations. But since the parameterization depends on experimental data it is often complicated and limited to available systems. This means a big limitation of this method. The parameter calculation for the DPD simulations is universal and independent from experimental data.

2.2 Phase Behavior of Amphiphilic Surfactants and Polymers

2.2.1 Mesoscopic Structures in Water

Amphiphilic compounds are commonly known as detergents and find many applications in everyday life. Their use can be followed from the ancient world to the present. However, the understanding of the activity of amphiphilic surfactants and polymers began in the past decades.

The characterization of surfactants by their hydrophilic head groups leads to four different groups¹:

a) Anionic surfactants:

Surfactants with a hydrophobic group and a negatively charged head group.

b) Cationic surfactants:

Surfactant with a hydrophobic group and a positively charged head group.

c) Nonionic surfactants:

Surfactants with a hydrophobic group and a hydrophilic head group with a strong dipole moment. Nonionic surfactants have no formal charge.

d) Amphoteric surfactants

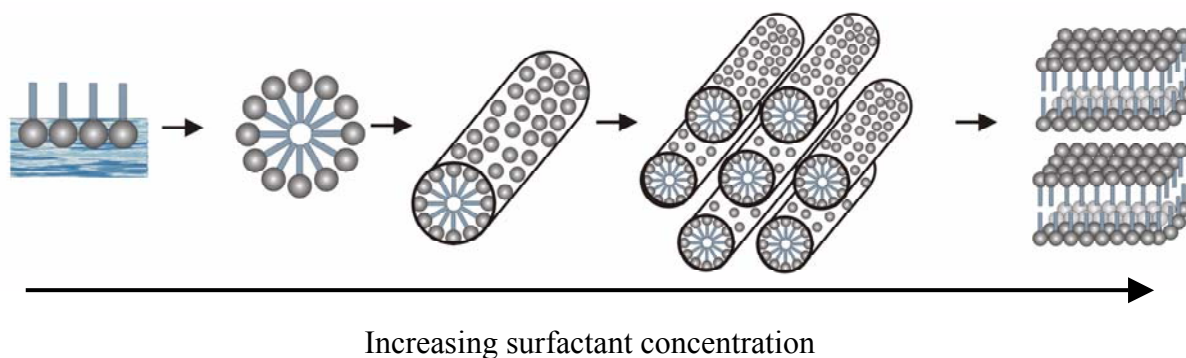
Surfactants with a hydrophobic group and a hydrophilic head group with a positive and a negative charge.

In this work the phase behavior and self-aggregation of nonionic surfactants and amphiphilic polymers has been investigated.

Based on the various phase behavior amphiphilic surfactants and polymers possess a wide range of applications in different areas such as organic and physical chemistry, biochemistry, polymer chemistry, mining, cosmetics, food additives and environmental chemistry. The variety of practical applications leads to many experimental and theoretical studies²⁻⁷.

Besides the wide range of applications in everyday life amphiphilic compounds are also taking part in nature, e.g. lipids in cell membranes. The combination of hydrophilic (polar) and hydrophobic (non-polar) parts marks the amphiphilic properties – the hydrophobic chain favors the oil phase, while the hydrophilic chain favors the aqueous phase. The behavior of surfactants on the molecular level depends on the lengths and flexibility of the hydrophobic hydrocarbons.

Figure 4. Phase behavior of surfactants in aqueous solution at different concentrations.



The different properties of the two parts of the molecule cause a complicated phase behavior based on the self-assembly of the amphiphilic molecules in solution. The aggregation and phase behavior of amphiphilic surfactants and polymers can be described as shown in Figure 4^{1,8}.

With the addition of an amphiphilic surfactant to water the surfactant molecules first dissolve as single molecules and then in the second step form an adsorption layer at the surface. If the surfactant concentration exceeds the *critical micelle concentration (cmc)* the surface cannot take more surfactant molecules and micelles are formed. At first the formation of spherical micelles takes place and then with the addition of even more surfactant the structure changes to rod like micelles. The formation of micelles controls the solubilization properties, which are responsible for the cleaning processes. With the addition of even more surfactant molecules the rod like micelles arrange in a hexagonal mesophase and if the concentration increases cubic, nematic or lamellar mesophases occur.

The surfactant aggregation, as all spontaneous processes, is controlled by the decrease of Gibb's free enthalpy G . The change of the free energy in an isothermic – isobaric system can be divided in enthalpic ΔH and entropic ΔS terms:

$$\Delta G = \Delta H - T\Delta S$$

47

The micelle formation enthalpy in aqueous systems is usually positive, compensated by an increase of the entropy which leads to a negative Gibb's free enthalpy ΔG . The increase of the entropy is mainly caused by the water molecules. The highly ordered cage-like structure is being destroyed by the isolated hydrophobic parts of the surfactants molecules. Liquid water has a structure of a room filling, isotropic network of hydrogen bonds^{9,10} The solution of a non-polar compound, e.g. alkyl chains, causes just a local change in the structure of the hydrogen bonds.

The so-called *hydrophobic effect*¹¹ depends on the size difference between water and the dissolved compound¹¹ as well as on the change of the dipole properties of the water molecules at the interface¹². The attraction of hydrocarbon chains in aqueous solution plays just a minor role^{9,10,13} in the aggregation behavior of amphiphilic molecules at normal temperatures.

The phase behavior of binary surfactant/water systems has been investigated by various experimental methods. Table 2 shows the most important investigation methods and structural properties of the different phases.

The different aggregation structures of amphiphilic surfactants characterize the possible structures and the associated properties of these structures. The experimental investigation of the phase behavior of amphiphilic surfactants and polymers is demanding and therefore the simulation of the different structures is a great advantage and useful for many applications.

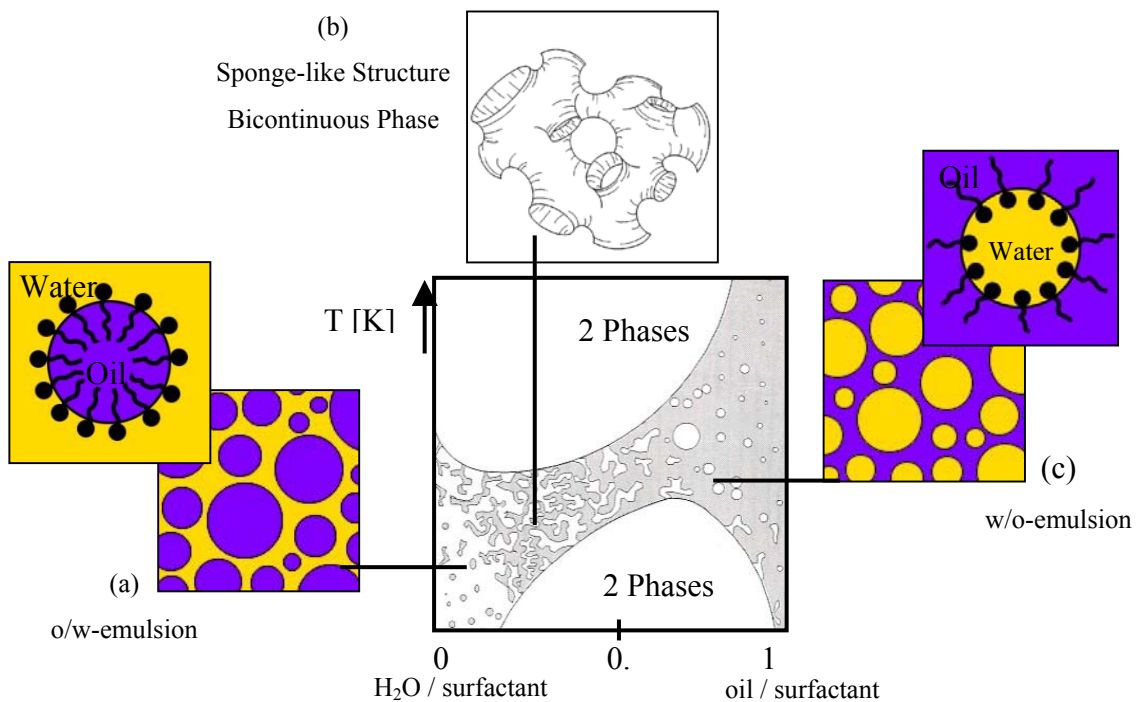
Table 2. Experimental investigation methods of mesophases¹⁴.

Method	Information
X-Ray Diffraction	conformation of alkyl chains
Polarization Microscopy	Identification of phases
Electron Microscopy	structure (lamellar, hexagonal, cubic)
IR-, Raman-, Fluorescence Spectroscopy	Head-group conformation; conformation of alkyl chains
NMR-Spectroscopy	Head-group conformation; Molecular rotation; complexation; Ion/ Head-group interaction
ESR- Spectroscopy	Phase transitions; lateral molecular distances; lateral Diffusion

2.2.2 Microemulsions

An emulsion is a dispersed system of two or more insoluble liquids. An emulsion is a phase inside a phase in form of small droplets. The size of droplets as well as the type of stabilization controls whether it is a micro- or macroemulsion. The macroemulsion is characterized by a particle size above 100nm and is kinetically stabilized, while a microemulsion is a colloidal dispersed system with a particle size below 100nm and a thermodynamic stabilization¹.

Figure 5. Theoretical phase behavior of a water-oil-surfactant system at a constant surfactant concentration¹.



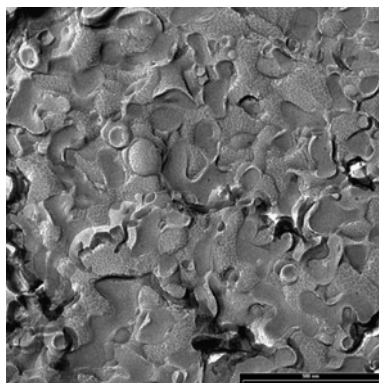
Microemulsions are optical isotropic, macroscopic homogeneous and thermodynamic stable mixtures of at least two immiscible components and a surfactant. The surfactant separates the two immiscible liquids by adsorbing at the interface. The adsorption at the interface reduces the water/oil interfacial tension.

A water-oil-surfactant (polymer) system can build three different types of microemulsions, depending on the water/oil ratio at a fixed surfactant concentration. Figure 5 shows the theoretical phase behavior. At an excess of water oil droplets in the water phase are formed with the amphiphilic surfactant at the interface (o/w-emulsion). The hydrophilic part of the surfactant reaches into the water phase and the hydrophobic part is inside the oil droplet and covers this way the oil and protects it from contact with water.

The opposite situation takes place at an excess of oil. Water droplets are now in the oil phase and are covered with the surfactant (w/o-emulsion).

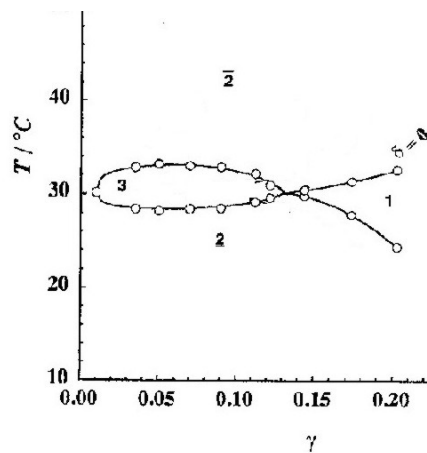
At an equal ratio of water and oil a bicontinuous structure is formed. The water and oil phase are both having the shape of tubes and penetrate each other. The surfactant is again at the interface with the hydrophilic part pointing towards the water and the hydrophobic part pointing towards the oil. Figure 6 shows an electron microscopy picture of the schematic draw of a bicontinuous phase in Figure 5 (b)

Figure 6. Electron microscopy picture of bicontinuous microemulsion¹.



Natural and technical emulsions usually consist of water and oil or fat. One of the two phases is the dispersing agent and the other the dispersed phase. Commonly known o/w-emulsions are e.g. milk and ice-crème and w/o – emulsions e.g. butter and lotions. Figure 5 shows the phase behavior of a water/oil/surfactant system with constant surfactant concentration and a varying water/oil ratio. For a given water/oil ratio the phase behavior depends on the surfactant concentration and the phase diagram¹⁵ is depicted in Figure 7.

Figure 7. Phase behavior of a water-oil-surfactant system at constant water/oil ratio.



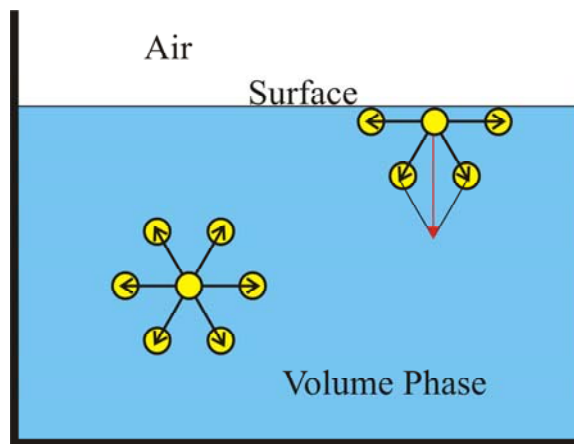
At a given water/oil ratio four different structures are possible depending on the surfactant concentration. $\bar{2}$ and $\underline{2}$ are two phase regions. At higher temperatures ($\bar{2}$) water separates and the two phases are an excess water phase and a microemulsion of the w/o-type. At lower temperatures ($\underline{2}$) the opposite is happening and the two phases are an excess oil phase and a microemulsion of the o/w-type. In between these two two-phase regions a three-phase region (3) occurs with water as well as oil separating from a bicontinuous microemulsion. The water and oil phase shrink with increasing surfactant concentration and at the so-called X-point the on-phase region begins (1). The only existing phase is now the bicontinuous microemulsion. The X-point is a landmark for the efficiency of a detergent and therefore important for many applications.

2.2.3 Surface Tension and Critical Micelle Concentration

Another property besides the self-organization of amphiphiles in the volume phase is the adsorption at a surface or interface. The adsorption of amphiphilic molecules at surfaces causes a change in the physical properties, especially the reduction of the surface tension.

Molecules at surfaces or interfaces are in a specific energetic condition. The interaction between single molecules can be explained through a vector diagram. As shown in Figure 8 are all intermolecular forces in the volume phase of a liquid being compensated. At the surface the compensation is not taking place caused by the absence of the neighbors at the outside. A force pointing inside the volume phase occurs.

Figure 8. Forces at the surface and in the volume phase.



Interfaces of two immiscible condensed phases consist of the surface layers of the two phases. To increase the surface the molecules have to be moved from the volume phases to the surface. During this process energy is needed to overcome the cohesive forces in the liquid.

The surface tension σ_{exp} is the force acting on a liquid-gas interface. It can be quantified as the force acting normal to the interface per unit length at equilibrium. Equation 48 defines the work w which produces the surface A :

$$w = \int_0^A \sigma \cdot dA = \sigma \cdot A \quad 48$$

As described in Figure 4, surfactants in solution form at low concentrations adsorption layers at the surface. This causes a reduction of the surface tension with increasing surfactant concentration until the adsorption layer is densely packed. Figure 9 shows schematically the adsorption of the surfactant molecules at the surface until the *critical micelle concentration (cmc)*. At the *cmc* the surface is completely covered with surfactant molecules and increasing the surfactant concentration causes the formation of micelles.

Figure 9. Schematic adsorption of surfactants at the surface.

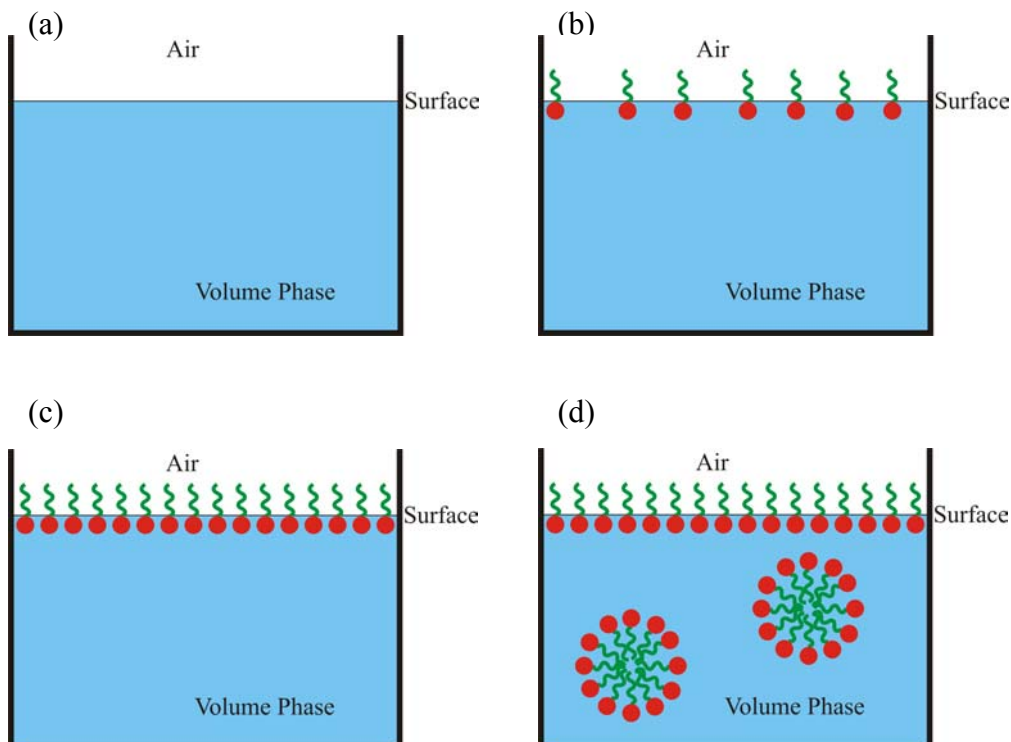
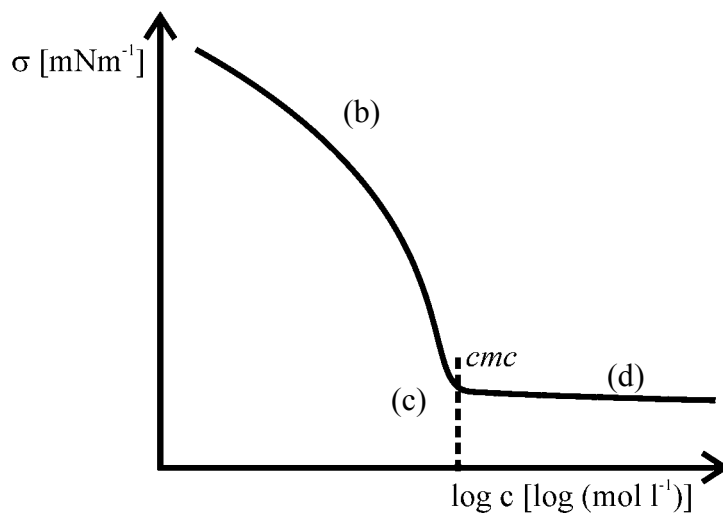


Figure 9 (a) shows the system without any surfactant in the solution and (b) with a surfactant concentration below the *critical micelle concentration* and an incomplete adsorption layer at the surface. Figure 9 (c) is the system at the *cmc* and with a completely adsorbed surface. At concentrations above the *cmc* (Figure 9 (c)) micelles are formed in the volume phase.

Figure 10. Schematic graph of the surface tension.



Through the process of adsorption the surface tension decreases constantly until the *critical micelle concentration* is reached and the surface has a complete adsorption layer. At concentrations above the *cmc* the surface tension has a constant value and does not decrease anymore due to the complete layer at the surface. The additional surfactants molecules are now forming micelles and therefore do not affect the surface tension anymore.

Figure 10 shows the schematic graph of the surface tension. The part of the graph with a gradient in the surface tension corresponds to Figure 9 (b). With reaching the *cmc* a complete adsorption layer is formed (c) and at higher concentrations the surface tension remains constant.

3 Results and Discussion.

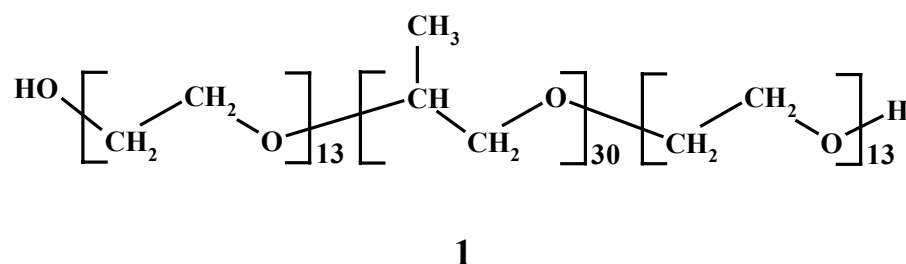
3.1 Self-Aggregation in Water

3.1.1 Poly (ethylene oxide)-*block*-poly (propylene oxide)-*block*-poly (ethylene oxide) in Water

3.1.1.1 Simulation Conditions

Dissipative Particle Dynamics (DPD) has been previously introduced¹⁶ to calculate different surfactant/water systems at room temperature. The system investigated was dodecyl dimethyl amine oxide (DDAO), which has a distinct hydrophilic head group with the dimethyl amine oxide and a hydrophobic alkyl chain. For the DDAO-water system the phase behavior as described in Figure 4 was simulated and the results were in good agreement with the experimental phase diagram. According to the clear difference of the interaction with water of the two parts (hydrophobic – alkyl chain and hydrophilic dimethyl amine oxide) the DPD-parameter calculation for this system was unproblematic¹⁶.

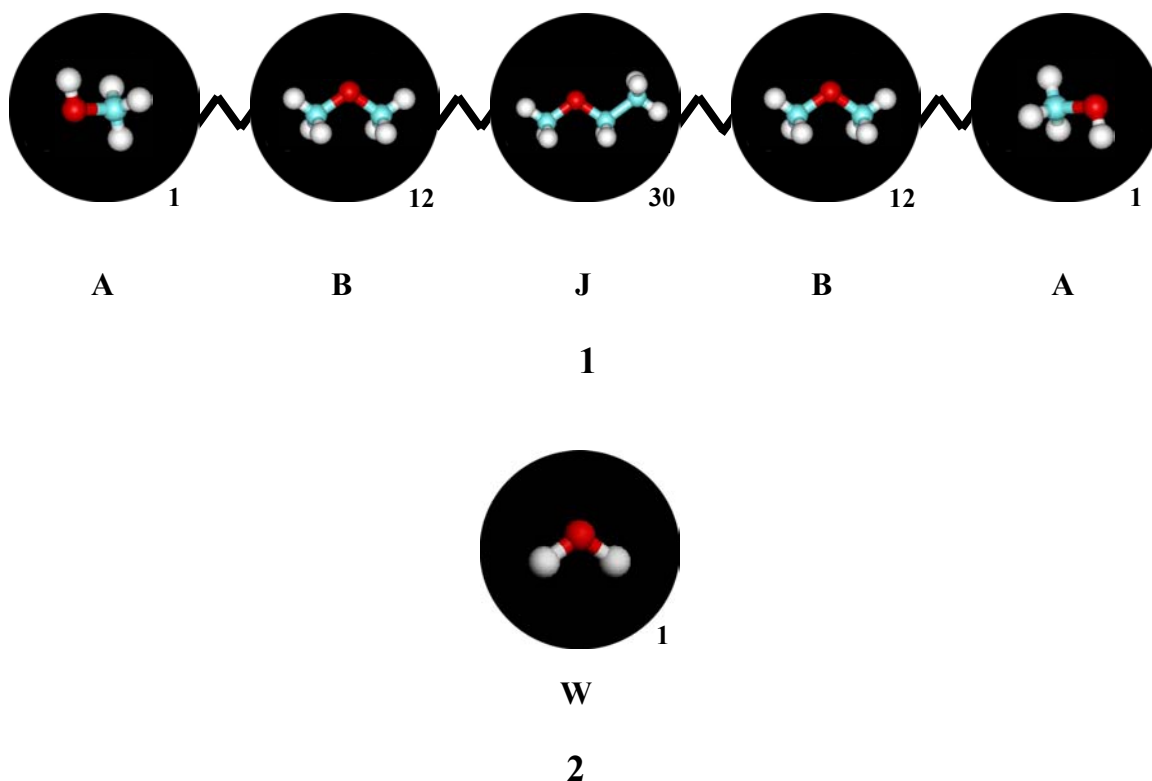
Figure 11. Structure of poly (ethylene oxide) -*block*- poly (propylene oxide) -*block*-poly (ethylene oxide) $\text{EO}_{13}\text{PO}_{30}\text{EO}_{13}$ (1).



More difficult are the poly (ethylene oxide) *-block-* poly (propylene oxide) *-block-* poly (ethylene oxide) triblock copolymers. They show an amphiphilic behavior and demonstrate a challenge for DPD calculations. The similarity of the two blocks of poly (ethylene oxide) and poly (propylene oxide) causes difficulties in the DPD-parameter calculation, which could be solved with the method described in Chapter 2.1.2.

The simulated system is a poly (ethylene oxide) *-block-* poly (propylene oxide) *-block-* poly (ethylene oxide) of the composition: $\text{EO}_{13}\text{PO}_{30}\text{EO}_{13}$ as shown in Figure 11.

Figure 12. DPD-model of poly (ethylene oxide)- *block* -poly (propylene oxide)- *block* -poly (ethylene oxide) $\text{EO}_{13}\text{PO}_{30}\text{EO}_{13}$ (1) in water (2).

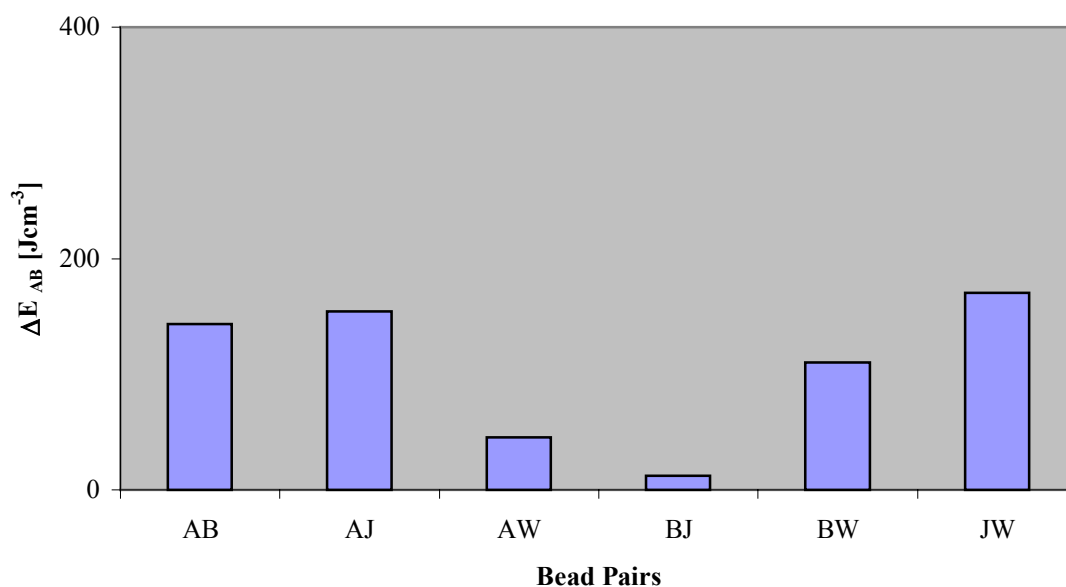


The DPD-model in Figure 12 contains three types of beads for 1. The beads at the end of the chain represent the most hydrophilic beads with the OH-group. The poly

(ethylene oxide) chain **B** is represented by the second hydrophilic bead and each poly (ethylene oxide) chain contains twelve of these “EO-beads” (**B**). The hydrophobic poly (propylene oxide) chain is represented by thirty beads (**J**). As mentioned before the DPD parameter calculation for the interaction of these three beads with water is difficult. The EO- and PO-beads **B** and **J** shown in Figure 12 just differ in one methyl group and are still supposed to show a hydrophilic behavior for the EO-bead and a hydrophobic behavior for the PO-bead (**J**). The method of parameter calculation described in the Theory section was capable to calculate these interactions with water correctly and appropriate parameters were obtained.

All simulations were carried out at a temperature of 300K and a box side length of about 35nm with a DPD density of $\rho_{\text{DPD}}=3$, which equals a normal density of $\rho=1\text{gcm}^{-3}$. The starting geometry was an arbitrary bead distribution in the box.

Figure 13. Pair interaction energies ΔE_{AB} in Jcm^{-3} for all bead pairs of the $\text{EO}_{13}\text{PO}_{30}\text{EO}_{13}$ - water system.



The differential pair interaction energies ΔE_{AB} were obtained by Monte Carlo simulations⁷⁶ and are diagrammed in Figure 13, where the x-coordinate shows the different bead pairs and the y-coordinate shows the energy ΔE_{AB} in Jcm^{-3} . The energies for pairs of equal beads were very close to 0 and therefore estimated as such. The very hydrophilic beads **A** have lower positive interaction energies with water than the other two beads **B** and **C** and mix therefore better with water. The more hydrophobic propylene oxide beads **J** have the highest positive values with water **W** due to their slightly repulsive behavior. The pair interaction energies of water beads **W** with the three beads **A**, **B** and **J** reflect the mixing behavior well. The interaction energy of **B** and **J** is almost zero which emphasizes the similarity of the two beads. The interaction energy of **A** and **B** is slightly lower than the one of **A** and **J**. The most hydrophilic beads **A** mix of course better with the more hydrophilic beads **B** than with the slightly hydrophobic beads **J**. For all bead pairs an average coordination number of 6.5 was estimated as obtained by Monte Carlo simulations⁷⁶.

3.1.1.2 Results

The self-assembly of poly (ethylene oxide) *-block-* poly (propylene oxide) *-block-* poly (ethylene oxide) triblock copolymers, also known as Pluronics[®] from BASF, are of great interest in many applications. Many different chain lengths of the poly (ethylene oxide) and the poly (propylene oxide) parts are possible which opens a wide range of structures and properties. Due to the great variety of applications the interest in the investigation of these system was immense. The phase behavior of such systems has been extensively discussed in the literature experimentally¹⁰²⁻¹⁰⁸, and theoretically with MesoDyn^{98,99}(see Chapter 2.1.3.3).

$\text{EO}_{13}\text{PO}_{30}\text{EO}_{13}$ has been experimentally investigated by Malka *et al.*²⁶ and shows four characteristic regions. At concentrations lower than 40wt% of $\text{EO}_{13}\text{PO}_{30}\text{EO}_{13}$ a micellar phase (L_1) has been found, which changes to a hexagonal phase (H) region between 40wt% and 60wt%. At even higher concentration a lamellar (L_α) phase is formed

until the concentration reaches 80wt% of $\text{EO}_{13}\text{PO}_{30}\text{EO}_{13}$, where the lamellar phase changes to the isotropic phase L_2 .

Figure 14 shows the experimental phase diagram²⁶ and the simulation results at distinct concentrations. The hydrophilic “end bead” **A** as defined in Figure 11 is shown in white and it is clearly visible that these most hydrophilic beads are always reaching in the water phase. The second hydrophilic bead, the “EO”-bead **B** is colored in red and covers in all simulations the hydrophobic “PO”-bead **J** (yellow) and acts this way like a spacer between water and the poly (propylene oxide) chain. This behavior has been investigated experimentally²⁶ and the simulation results agree nicely and proof the calculated DPD-parameters to be appropriate.

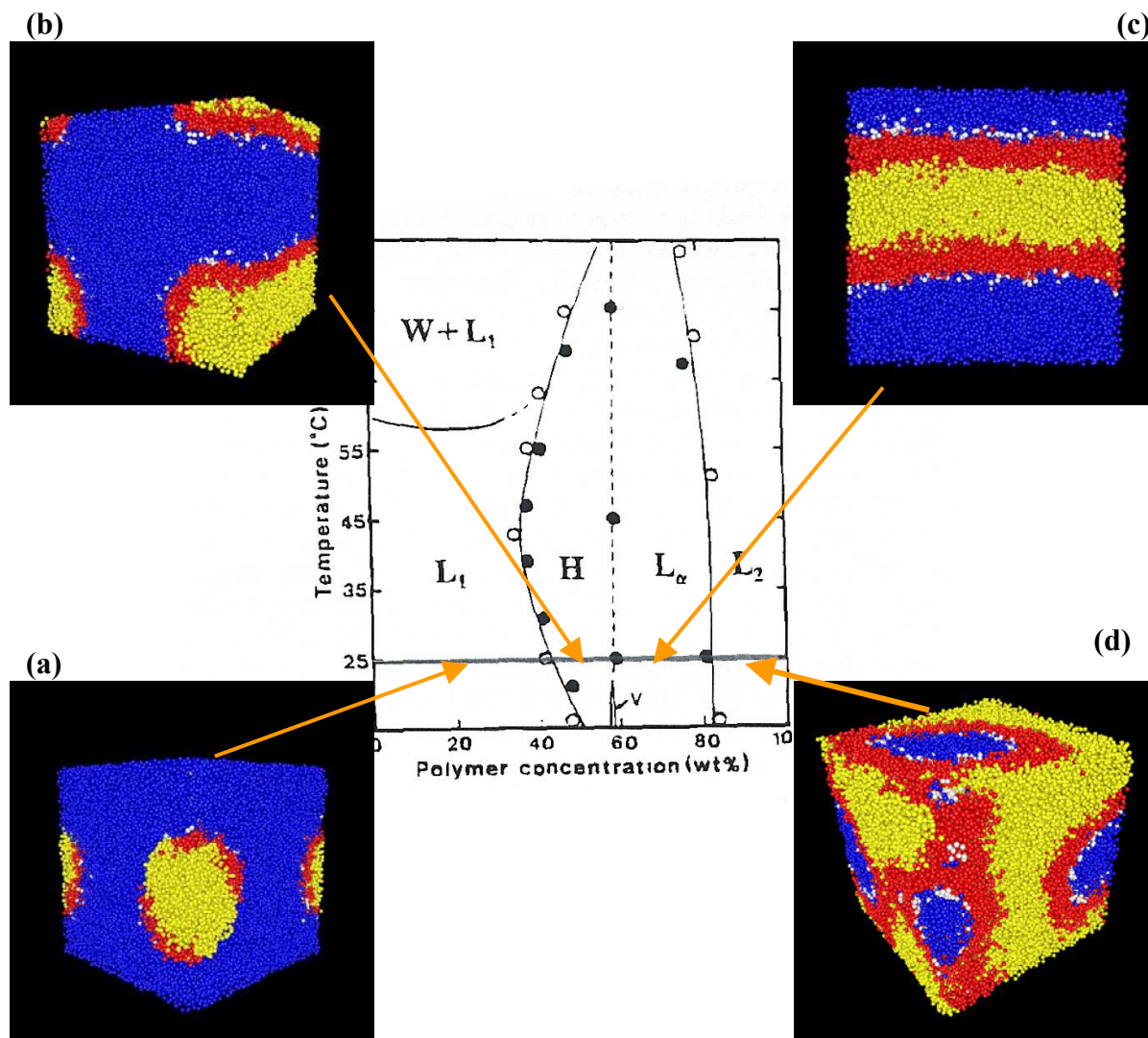
All simulations carried out at concentrations below 40wt% of $\text{EO}_{13}\text{PO}_{30}\text{EO}_{13}$ showed the experimentally found L_1 phase. Figure 14 (a) shows the simulation result at 20wt%, where micelles in the water phase are formed. Each micelle has a core, which contains the poly (propylene oxide) and a rim. The rim is the poly (ethylene oxide) protecting the poly (propylene oxide) against the contact with water.

Figure 14 (b) shows the result of the calculation in the next experimental region: the hexagonal phase (H). A change in the shape of the structure from spherical micelles to rods can be observed. This indicates the formation of a hexagonal phase, which could not be observed in entirety because of the limitation in the box size.

The same problem occurred in Figure 14 (c) where the lamellar phase is just implied by the appearance of one lamella. The structure of the simulation at 70wt% shows nicely how a bilayer of the polymer has been formed.

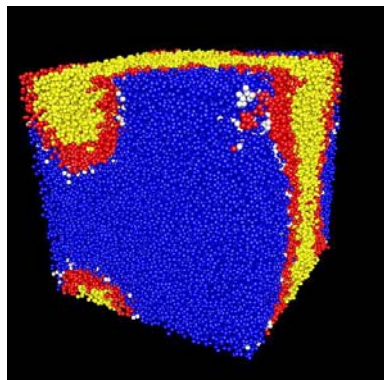
The experimentally found L_2 phase at very high polymer concentrations was determined at concentrations higher than of 85wt%. Figure 14 (d) shows how water droplets are dissolved in the polymer phase and form inverse micelles.

Figure 14. $\text{EO}_{13}\text{PO}_{30}\text{EO}_{13}$ (1) experimental phase diagram and simulation results at 300K at (a) 20wt%, (b) 50wt%, (c) 70wt% and (d) 90wt% polymer in water.

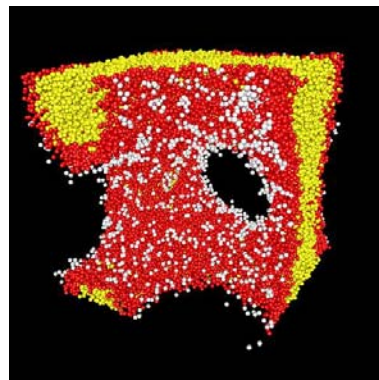


The experimental phase diagram of Malka *et al.*²⁶ showed just the described four regions, while Alexandridis *et al.*²⁷ found a bicontinuous phase (L') at about 60 wt% polymer concentration. The simulation reproduced these results with remarkable agreement. Figure 15 represents the simulation results at a polymer concentration of 60wt% and shows nicely the water tubes in the polymer structure as well as the poly (propylene oxide) tubes covered with the poly (ethylene oxide) in the water phase.

Figure 15. Simulation results at 60 wt% $\text{EO}_{13}\text{PO}_{30}\text{EO}_{13}$. (a) shows the L' phase with water and (b) without.



(a)



(b)

3.1.2 C₁₀E₄ and C₁₂E₅ in Water

3.1.2.1 Simulation Conditions

The phase behavior of the two nonionic surfactants C₁₀E₄ (**3**) and C₁₂E₅ (**4**) (Figure 16) in water (**2**) at different surfactant concentrations has been simulated. The surfactant C₁₂E₆ has been simulated at distinct points of the phase diagram to carry out structural investigations.

Figure 16. Structure of C₁₀E₄ (**3**) and C₁₂E₅ (**4**).

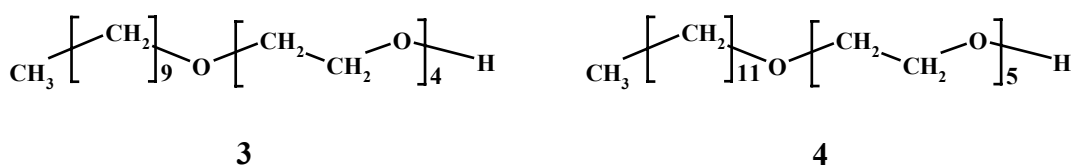
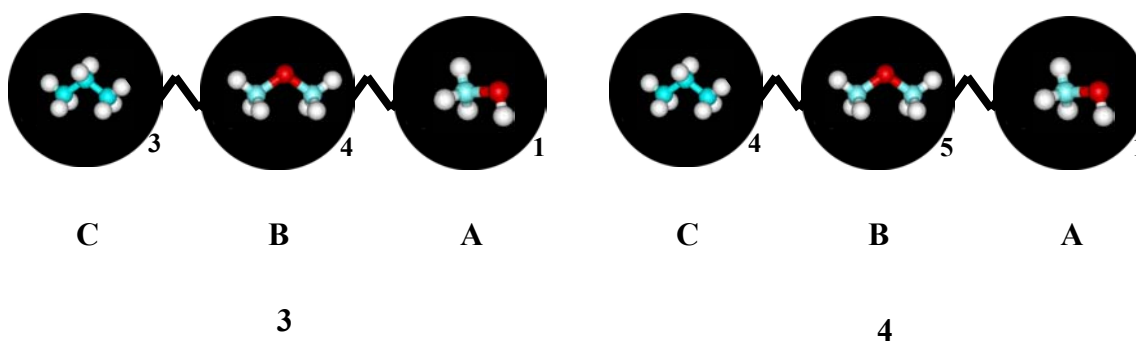


Figure 17 shows the DPD-particles (beads) for the investigated systems. Water (**2**) is always represented by one bead. The surfactants C₁₀E₄ (**3**) and C₁₂E₅ (**4**) are divided into two parts, the hydrophobic and the hydrophilic chains, which are themselves represented by several beads. The surfactant C₁₂E₆ (**5**) has been represented by the bead chain **1 A** – **6 B** – **4 C**.

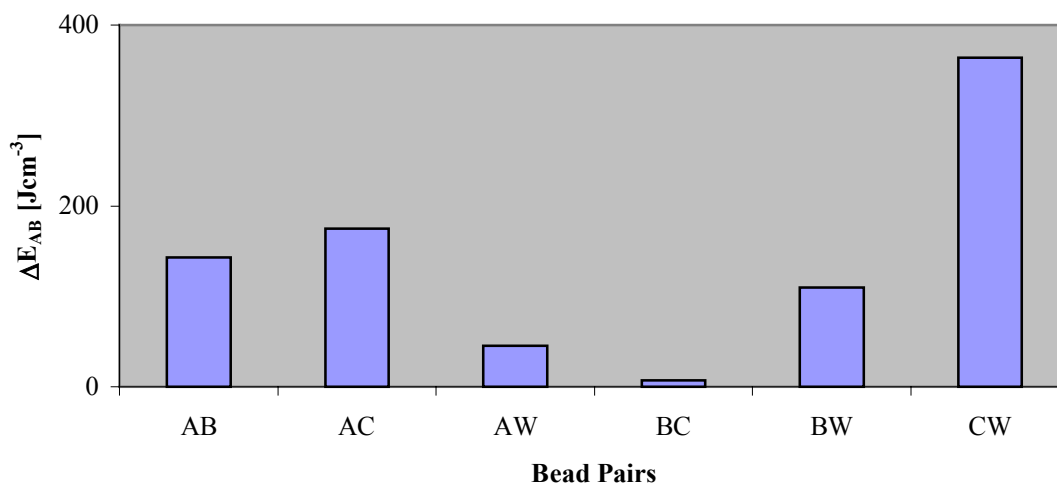
The simulation temperature was 300K and the box side length for the C₁₀E₄ system was about 17nm and for C₁₂E₅ about 25nm with a DPD density of $\rho_{\text{DPD}}=3$, which equals a normal density of $\rho=1\text{gcm}^{-3}$. All simulations were carried out with a starting geometry of an arbitrary bead distribution in the box. For all bead pairs an average coordination number Z of 6.5 was estimated as obtained by Monte Carlo simulations⁷⁶.

Figure 17. Schematic representation of the simulation model for $C_{10}E_4$ (3) and $C_{12}E_5$ (4).



The differential pair interaction energies ΔE_{AB} were obtained by Monte Carlo simulations⁷⁶ and are diagrammed in Figure 18, where the x-coordinate shows the different bead pairs and the y-coordinate shows the energy ΔE_{AB} in Jcm^{-3} . The energies for pairs of equal beads were very close to 0 and therefore estimated as such. Figure 18 makes the differences in the behavior of different bead pairs visible. The interaction energy calculation has already been proved to be reliable for the complicated $EO_{13}PO_{30}EO_{13}$ system in Chapter 3.1.1.

Figure 18. Pair interaction energies ΔE_{AB} in Jcm^{-3} for all bead pairs of the $C_{10}E_4$, $C_{12}E_5$ and $C_{12}E_6$ - water system.

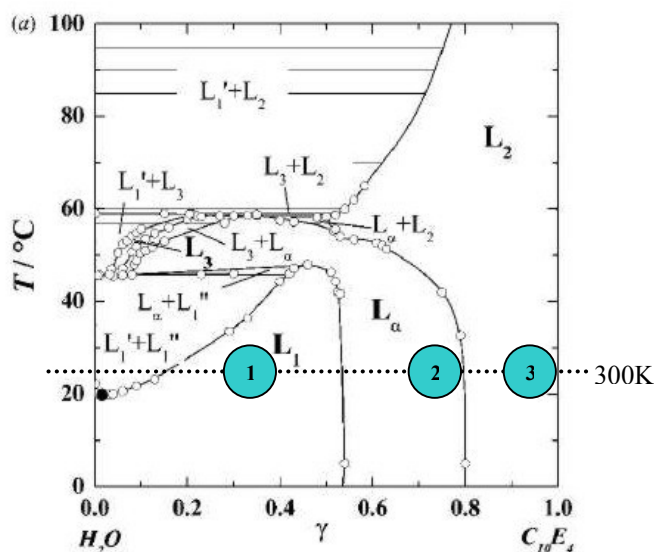


The hydrophobic bead (**C**) has a high positive value with water (**W**) due to their repulsive behavior. The hydrophilic beads (**A**, **B**) have lower interaction energies and mix therefore better with water. The bead **A** has the lowest interaction energy with water (**W**) and a higher interaction energy with the hydrophobic bead **C** due to its hydrophilicity. The less hydrophilic bead **B** has a very small interaction energy with the alkyl chain bead **C** which shows its almost hydrophobic character. For all bead pairs an average coordination number of 6.5 was estimated as obtained by Monte Carlo simulations⁷⁶.

3.1.2.2 Simulation of the Phase Behavior

The experimental phase diagram of a $C_{10}E_4$ /water mixture (Figure 19) shows three characteristic phases at a temperature of 300K^{28,29}. An isotropic L_1 phase, which changes into a lamellar L_α phase at concentrations between 55wt% and 80wt% of $C_{10}E_4$ and an isotropic L_2 phase at concentrations higher than 80wt% of $C_{10}E_4$.

Figure 19. Experimental phase diagram of $C_{10}E_4$ (3) in water²⁹.



The simulations reproduce all characteristic phases. Figure 20 shows the simulation results at three concentrations as assigned in Figure 19: (a) the isotropic L_2 phase at a surfactant concentration of 35wt%, (b) the lamellar L_α phase at 75wt% and (c) the isotropic L_1 phase at a $C_{10}E_4$ concentration of 95wt%.

Figure 20. Simulation results at a $C_{10}E_4$ concentration of (a) 35wt%, (b) 75wt% and (c) 95wt%.

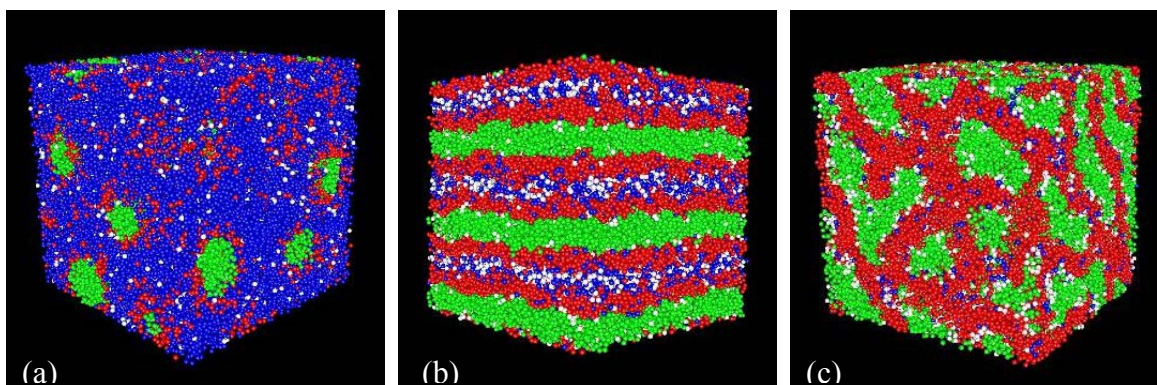


Figure 21 follows the formation of the lamellar phase in the dynamics calculation at different calculation times. At the beginning of the simulation (0ns) all beads are homogeneously distributed in the box. During the simulation the surfactant domains steadily grow until the system reached the thermodynamic equilibrium. With equilibration an unordered phase at the beginning of the calculation forms bilayers, which finally become ordered in a lamellar phase at 472ns.

Figure 21. Formation of the lamellar phase at 75wt% $C_{10}E_4$ at different simulation times.

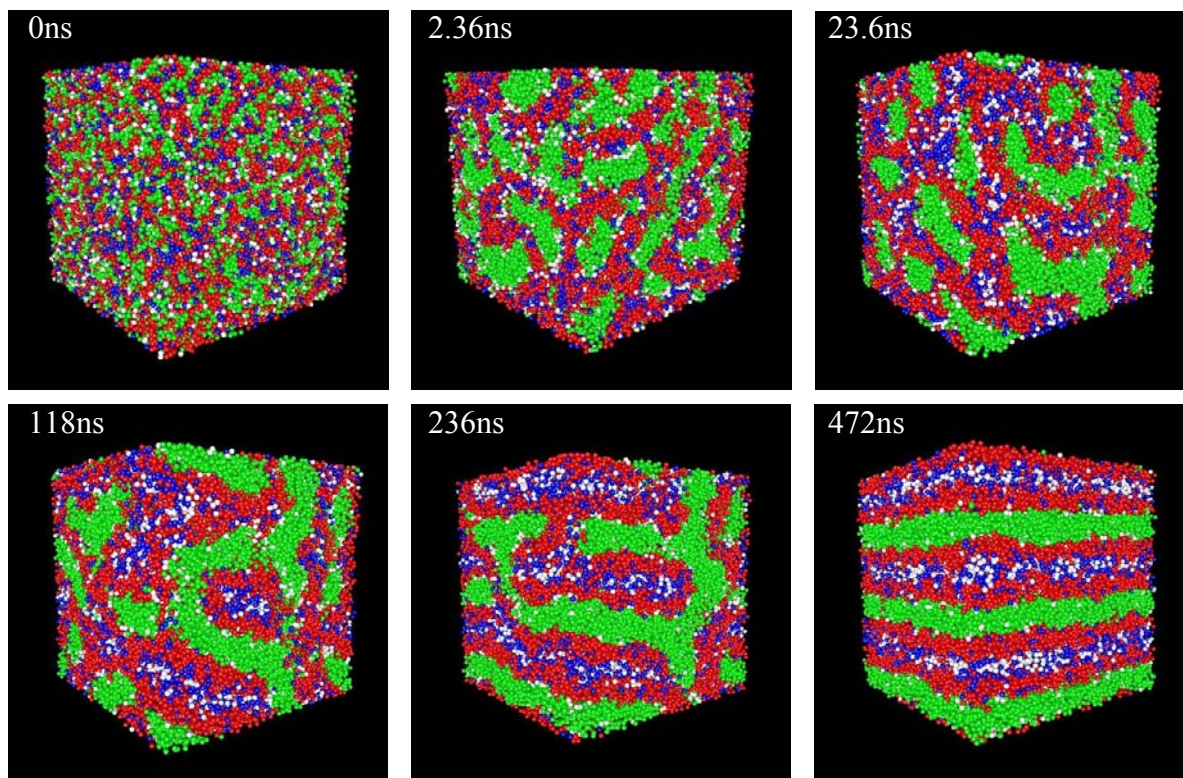
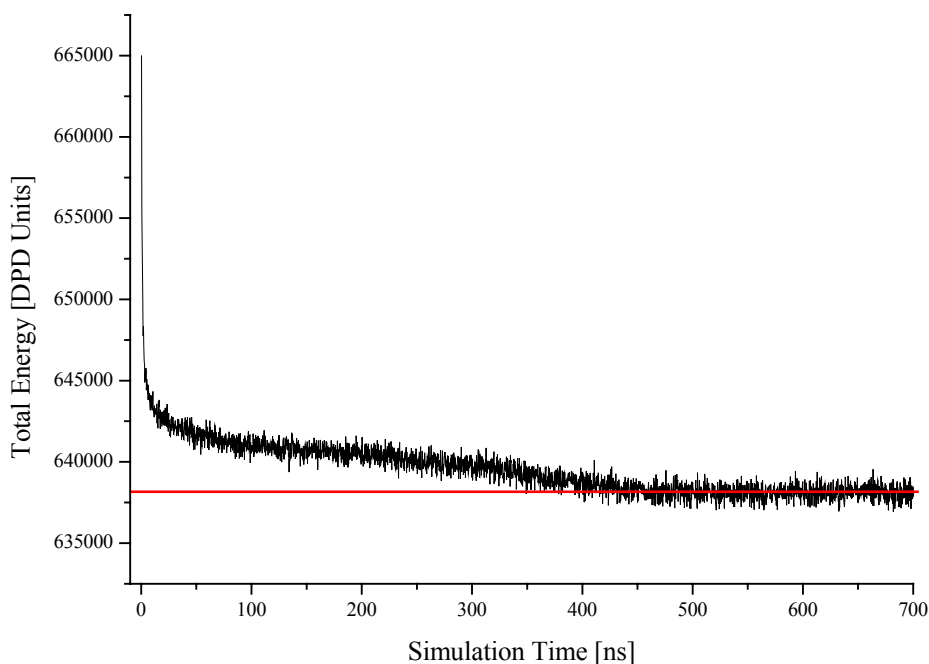


Figure 22 shows the total energy, the sum of potential and kinetic energy, of the system in DPD units during the lamellar formation. The arbitrary bead distribution in the box is energetically unfavored and has a very high total energy (0ns). As long as the system still undergoes the formation of the bilayers the energy decreases. After about 450ns the system converged to the thermodynamic equilibrium and the total energy fluctuates around a constant value. The steep descending curve at the beginning of the simulation can be explained with the highly unfavored starting configuration. After about 25ns the gradient decreases due to the formation of domains of bilayers as shown in Figure 21 (23.6ns). The final formation of the highly ordered lamellar phase out of the bilayer domains is slower and takes another 425ns.

Figure 22. Total energy [DPD Units] of the system shown in Figure 21.

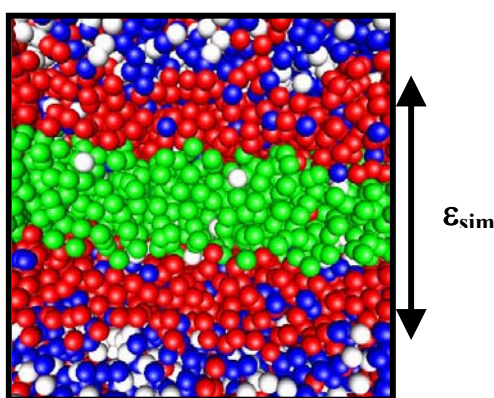
The equilibration of the system is reached in a short time in comparison to the experiment due to the high energy configuration at the beginning of the simulation. The arbitrary bead distribution equals a homogeneous distribution on the molecular level is never reached in the experiment, where always small micro domains of surfactants are left. These micro domains stabilize the system, the energy is not as high and the equilibration takes therefore longer.

The horizontal line in Figure 22 indicates the average energy of the system after reaching the equilibrium. The fluctuations are caused by the dynamics of the system which produces different (more or less stable) configurations. The total energy curve in Figure 22 corresponds with the pictures at different simulation times as shown in Figure 21, where the equilibrium has obviously been reached between 236ns and 472ns.

Figure 23 shows the zoom into the lamellar phase of Figure 20 (b) at a surfactant concentration of 75wt%. The $C_{10}E_4$ bilayer is nicely visible. The hydrophobic alkyl chains (C beads) form the inner part of the layer (green), while the hydrophilic ethylene oxide

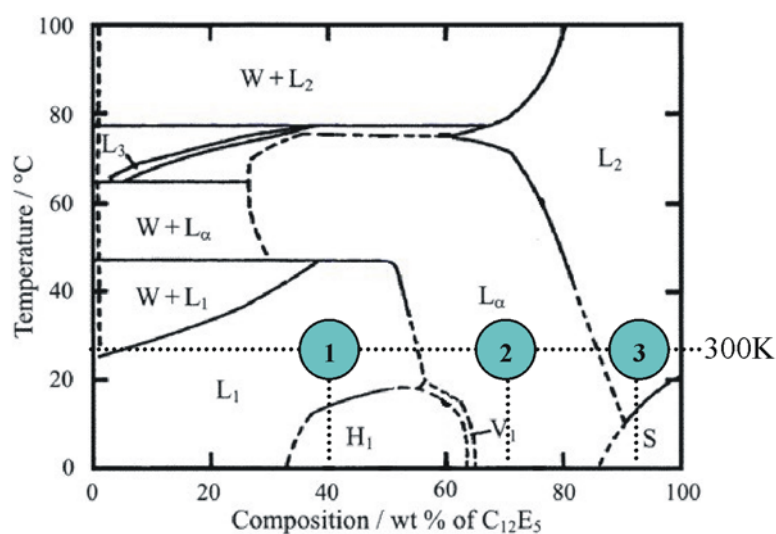
chains in red (**B** beads) shield the inner layer from the water (blue). The red ethylene oxide layer is penetrated by water molecules (blue) The most hydrophilic end beads (**A** beads, white) are mainly distributed in the water phase.

Figure 23. Snapshot of the bilayer of $C_{10}E_4$ at a surfactant concentration of 75wt%.



The experimental phase diagram of the $C_{12}E_5$ /water mixture³⁰ (Figure 24) shows similar characteristic regions as for $C_{10}E_4$ in Figure 19. An isotropic L_1 phase, which changes into a lamellar L_α phase at concentrations between 55wt% and 85wt% $C_{12}E_5$ and an isotropic L_2 phase at concentrations higher than 85wt% $C_{12}E_5$.

Figure 24. Experimental phase diagram of $C_{12}E_5$ in water³⁰.



The simulations showed all characteristic phases. Figure 25 shows the simulation results at three concentrations as assigned in Figure 24. (a) shows the isotropic L_1 phase at a surfactant concentration of 40wt%, (b) the lamellar L_α phase at 70wt% and (c) the isotropic L_2 phase at a $C_{12}E_5$ concentration of 95wt%.

The surfactant (4) alkyl chain beads (C) are green, the ethylene oxide beads (B) are red, the hydrophilic end-beads (A) are white and the water beads (W) are blue.

Figure 25 (a) shows $C_{12}E_5$ micelles in the blue water phase at a surfactant concentration of 40wt%. Figure 25 (b) shows a lamellar phase with $C_{12}E_5$ bilayers and water layers at a surfactant concentration of 70wt%. The interruption in one of the bilayers is caused by the dynamics of the system, which causes sometimes defects in the bilayers.

The isotropic phase in Figure 25 (c) at high surfactant concentrations (95wt%) shows small water domains (blue) in the surfactant phase.

Figure 25. Simulation results at a $C_{12}E_5$ concentration of (a) 40wt%, (b) 70wt%, and (c) 95wt%.

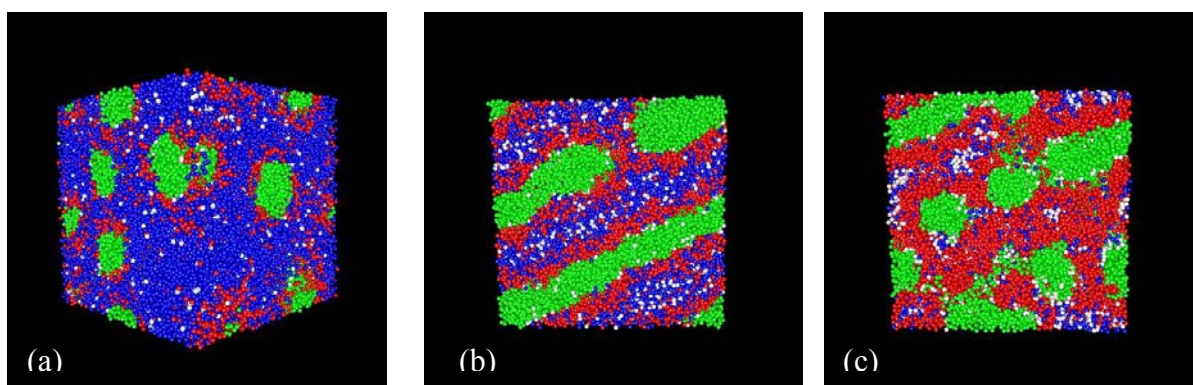


Figure 26 (a) shows one micelle. The core of the micelle is the hydrophobic alkyl chain (green) surrounded by the hydrophilic ethylene oxide chain (red). The ethylene oxide chain shields the hydrophobic alkyl chain from the water and are as for $C_{10}E_4$ penetrated with water. The most hydrophilic end beads (white) are distributed in the water phase.

Figure 26. Simulation results at a $C_{12}E_5$ concentration of (a) 40wt%, and (b) 70wt%.

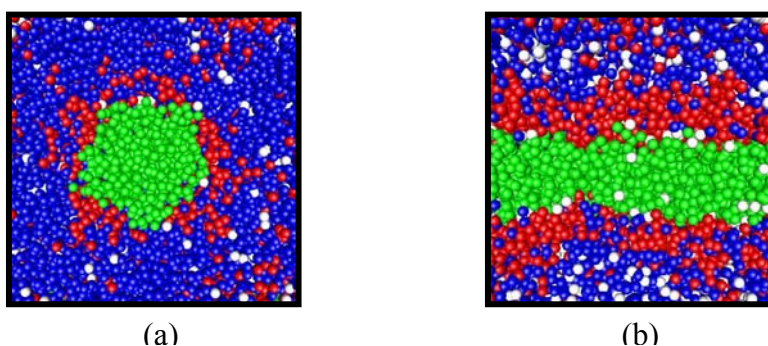


Figure 26 (b) shows one $C_{12}E_5$ bilayer. The hydrophobic alkyl chains form the inner part of the layer (green), while the hydrophilic ethylene oxide chains (red) cover the inner layer from the water (blue). The most hydrophilic end beads (white) are distributed in the water phase.

Figure 27. Formation of the micellar phase at 40wt% $C_{12}E_5$ at different simulation times.

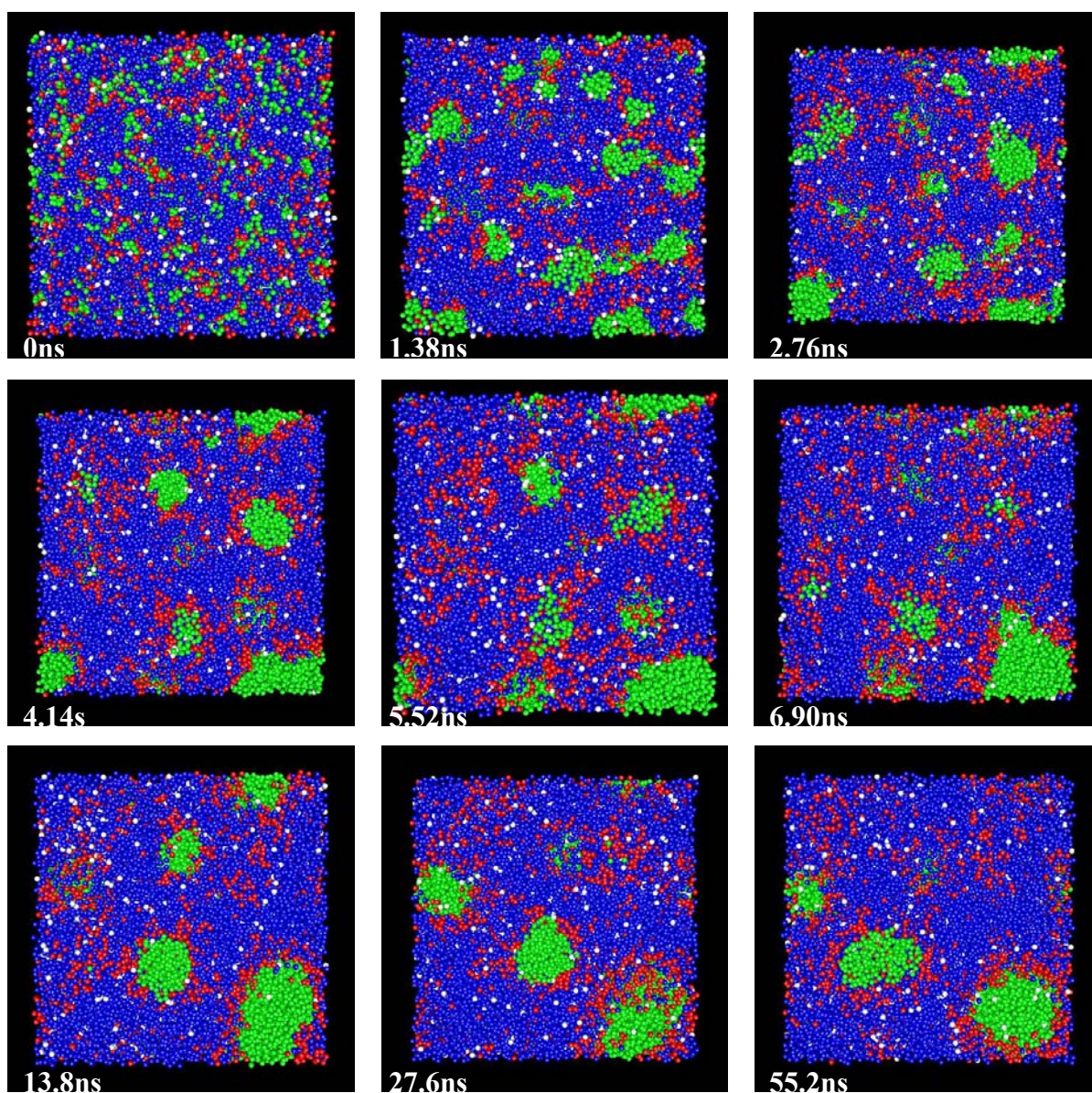
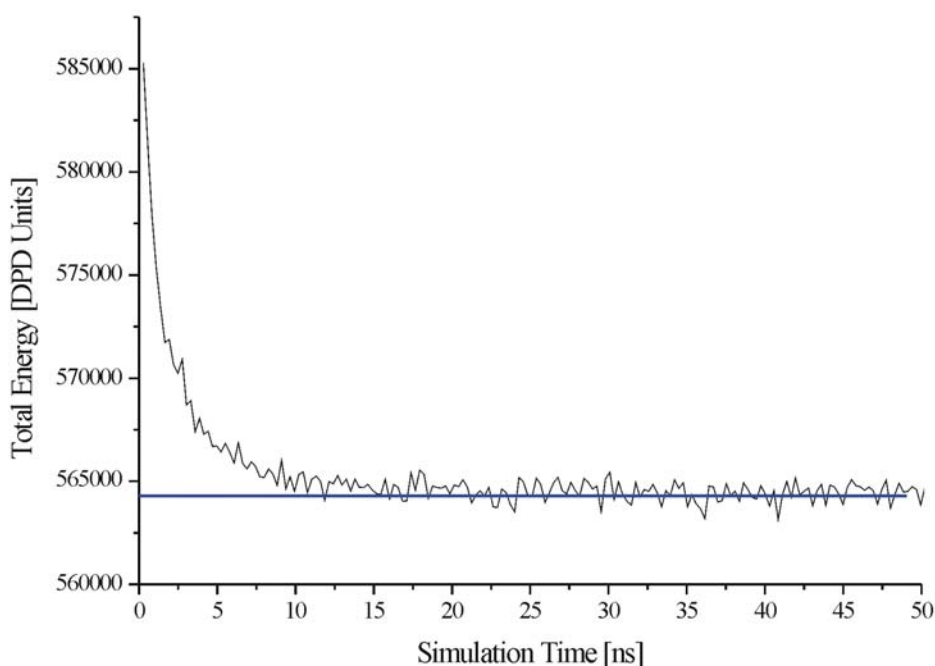


Figure 27 shows the dynamics of the micelle formation. At the beginning of the simulation (0ns) all beads are homogeneously distributed in the box. During the dynamics simulation the surfactant domains steadily grow until the system reached the thermodynamic equilibrium. With reaching the equilibrium the micelle size in the simulation converges to a constant value.

Even after a comparably short simulation time of 1.38ns the alkyl chains (green) of the surfactant build aggregates and are mostly shielded from the water phase (blue) by the hydrophilic ethylene oxide chains (red). Between 2.76ns and 13.8ns (Figure 27) varies the size of the “micelles” until after 27.6ns the equilibrium seems to be reached and the micelle size is almost constant (Figure 27, 55.2ns).

Figure 28 shows the total energy of the system in DPD units during the micelle formation. The arbitrary bead distribution in the box is energetically unfavored and has a very high total energy. As long as the system still undergoes the formation of the micelles the energy drops. After about 20ns the system reached the thermodynamic equilibrium and the total energy converged.

Figure 28. Total energy [DPD Units] of the system shown in Figure 27.



The equilibration of the system is fulfilled in a short time in comparison to the experiment due to the high energy configuration at the beginning of the simulation. The homogeneous distribution on the molecular level is never reached in the experiment, where always small micro domains of surfactants are left. These micro domains stabilize the system, the energy is not as high and the equilibration take therefore longer.

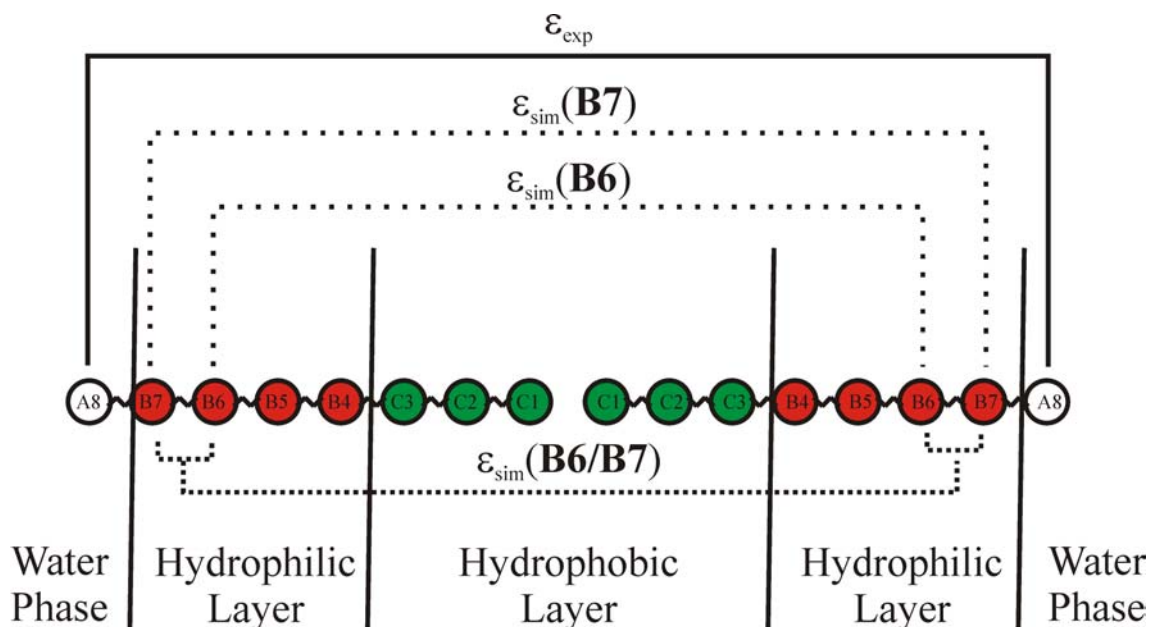
The blue line in Figure 28 indicates the average energy of the system after reaching the equilibrium. The fluctuations are caused by the dynamics of the system which produces different (more or less stable) configurations. The total energy curve corresponds with the pictures at different simulation times as shown in Figure 27, where the equilibrium has obviously been reached between 13.8ns and 27.6ns.

The equilibrium of the micellar formation has been reached after about 20ns. The formation of the lamellar structure of $C_{10}E_4$ in Figure 21 and 22 took 400ns – 20 times longer than the micellar formation due to the higher ordered structure.

3.1.2.3 Structural Investigation

The phase behavior as investigated with DPD for $C_{10}E_4$ and $C_{12}E_5$ can yield structural information of the obtained phases. The conversion of e.g. bilayer thickness from DPD units into physical units can prove the reliability of the Dissipative Particle Dynamics studies not just qualitatively as the phase behavior but quantitatively. Figure 29 shows schematically the bilayer represented by one molecule of each monolayer. The molecules are represented by 3 **C**, 4 **B**, and 1 **A** beads as defined in Figure 17. The layer thickness ϵ_{exp} as obtained by experimental measurements²⁹ contains all $C_{10}E_4$ beads from both molecule monolayers which means the distance between the two **A8** beads. The $C_{10}E_4$ bilayer thickness ϵ_{exp} was experimentally estimated by Stubenrauch *et al.*²⁹ to $\epsilon_{\text{exp}}=5.0\text{nm} \pm 0.5\text{nm}$.

Figure 29. Schematic draw of the $C_{10}E_4$ bilayer.



The bilayer in the simulation result is defined by the alkyl chains (green) and the ethylene oxide chains (red) as shown in Figure 23. The hydrophilic end beads (white) are already distributed in the water phase. Therefore the simulated bilayer thickness ϵ_{sim} was obtained from the average distance of the last ethylene oxide beads of each chain (**B7**), of the second last ethylene oxide beads of each chain (**B6**) and, of the last two ethylene oxide beads of each chain (**B6/B7**) of the two monolayers. The simulated bilayer thickness was calculated to $\epsilon_{\text{sim}}(\mathbf{B6})=4.3\text{nm}$, $\epsilon_{\text{sim}}(\mathbf{B7})=4.9\text{nm}$ and $\epsilon_{\text{sim}}(\mathbf{B6/B7})=4.6\text{nm}$. The longer distance of $\epsilon_{\text{sim}}(\mathbf{B7})$ can be explained by Figure 29. The beads **B7** are the last ones of the ethylene oxide chain and have therefore the largest distance and should correspond best to the experimental bilayer thickness. The calculated bilayer thickness is in good agreement with the experimental value of $\epsilon=5.0\text{nm} \pm 0.5\text{nm}^{29}$. The slightly smaller value can be explained by the negligence of the **A** beads in the calculation of ϵ_{sim} which are included in the experimental measurements.

Figure 30. Snapshot of the C_{10}E_4 micelle at a surfactant concentration of 35wt%.

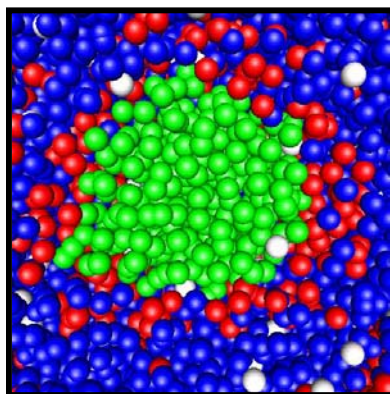


Figure 30 shows the zoom of one micelle in the L_1 phase. The core of the alkyl chains (green) is shielded by the ethylene oxide beads (red) from the water (blue). And the ethylene oxide layer is penetrated with water.

The calculation of the micellar and lamellar phases of C₁₀E₄ and C₁₂E₅ has been described in the previous chapter. The micellar and lamellar phase of C₁₂E₆ have been calculated at distinct concentrations as assigned in the experimental phase diagram³¹. The micellar aggregation number, of the micelle shown in Figure 30 and the bilayer thickness of C₁₀E₄, C₁₂E₅ and C₁₂E₆ have been calculated with DPD.

All values are in remarkable agreement with the experimental values as available. The micellar aggregation number of C₁₀E₄ has been calculated to 53 (±10), of C₁₂E₅ to 98 (± 14) and for C₁₂E₆ to 79 (± 16) in comparison to an experimental value³² of 87. The experimental bilayer thickness of C₁₀E₄ has been measured to 5.0 ± 0.5nm²⁹ and simulated to 4.9 nm as explained before. The thickness of the C₁₂E₅ bilayer has been calculated as described for C₁₀E₄ and was 6.3nm while the experimental bilayer was 6nm³³. The C₁₂E₆ bilayer has been calculated to 7.7nm. The bilayer thickness increase from C₁₀E₄ to C₁₂E₅ and C₁₂E₆ according to the growing of the chain lengths in this row. The structural data obtained from Dissipative Particle Dynamics calculations are designated in Table 3.

Table 3. Structural data of the surfactants C₁₀E₄, C₁₂E₅ and C₁₂E₆. The experimental values are put in parentheses.

Surfactant	Micellar Aggregation Number	Bilayer Thickness
C ₁₀ E ₄	53 ± 10	4.9 nm (5.0 ± 0.5nm ²⁹)
C ₁₂ E ₅	98 ± 14	6.3 nm (6 nm ³³)
C ₁₂ E ₆	79±16 (87 ³²)	7.7 nm

3.2 Self-Aggregation in Water and Oil

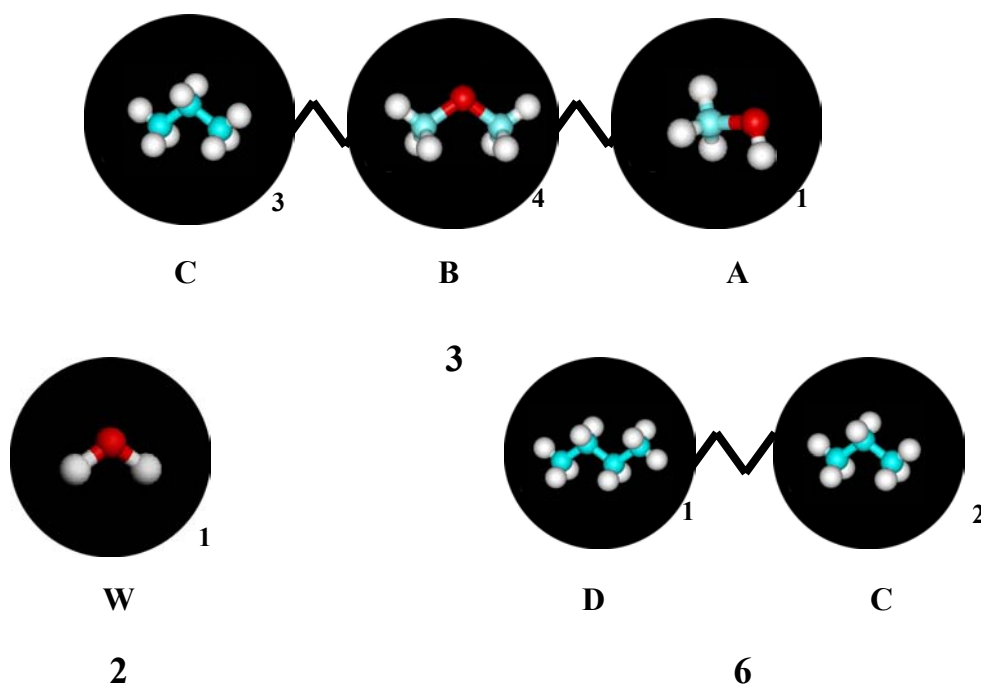
3.2.1 $C_{10}E_4$ in Water and n-Decane

3.2.1.1 Simulation Conditions

Representatively for the phase behavior of the self-aggregation in a water and oil mixture the phase behavior of $C_{10}E_4$ (3) in water (2) and n-decane (6) at different surfactant concentrations has been studied.

Figure 31 shows the DPD-particles (beads) for the investigated system. Water (2) is always represented by one bead and the oil (6) by three beads. The surfactant $C_{10}E_4$ (3) is divided into two parts, the hydrophobic and the hydrophilic chains, which are themselves represented by several beads as described before in Figure 17.

Figure 31. Schematic representation of the simulation model for $C_{10}E_4$ (3), water (2) and n-decane (6).



The block copolymer used in these investigations, PEP5-PEO5 (5), is a poly (ethylene propylene)-*block*-poly (ethylene oxide) with 70 ethylene, 70 propylene and 114 ethylene oxide units. The molecular weight of the hydrophobic and hydrophilic chain is each about 5000 g mol⁻¹. The molecular structure is shown in Figure 32.

Figure 32. Structure of PEP5-PEO5 (7).

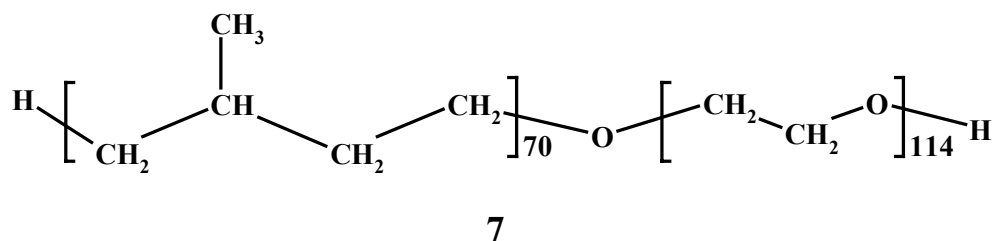
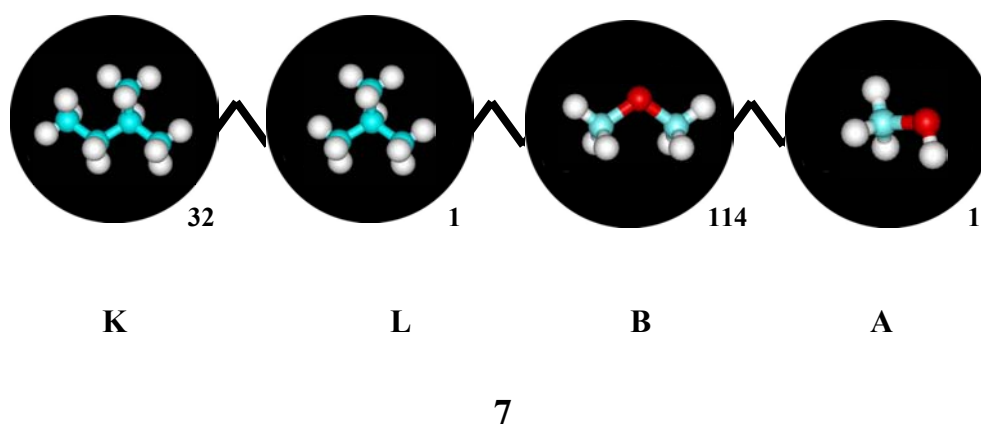


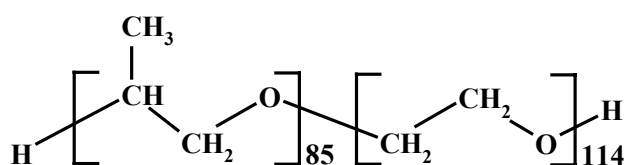
Figure 33 shows the DPD-model of 7. The polymer is divided into two parts, the hydrophobic and the hydrophilic chains, which are themselves represented by several beads analogous to the surfactant C₁₀E₄.

Figure 33. Schematic representation of the simulation model of 7.



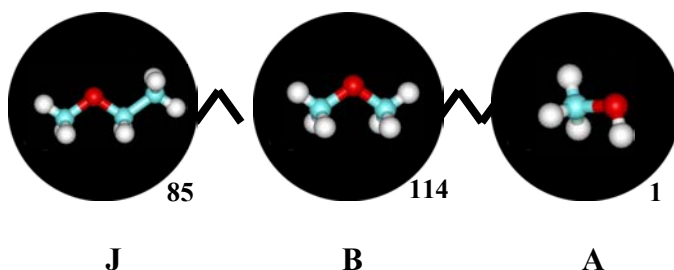
The second polymer used is a poly (propylene oxide) – *block* - poly (ethylene oxide) PPO5-PEO5 (**8**) (Figure 34) diblock copolymer with 85 propylene oxide and 114 ethylene oxide units. The molecular weight of the hydrophobic and hydrophilic chain is each about 5000 gmol⁻¹.

Figure 34. Structure of poly (propylene oxide) – *block* - poly (ethylene oxide) PPO5-PEO5 (**8**).



8

Figure 35. DPD-model of poly (propylene oxide) – *block* - poly (ethylene oxide) PPO5-PEO5 (**8**).



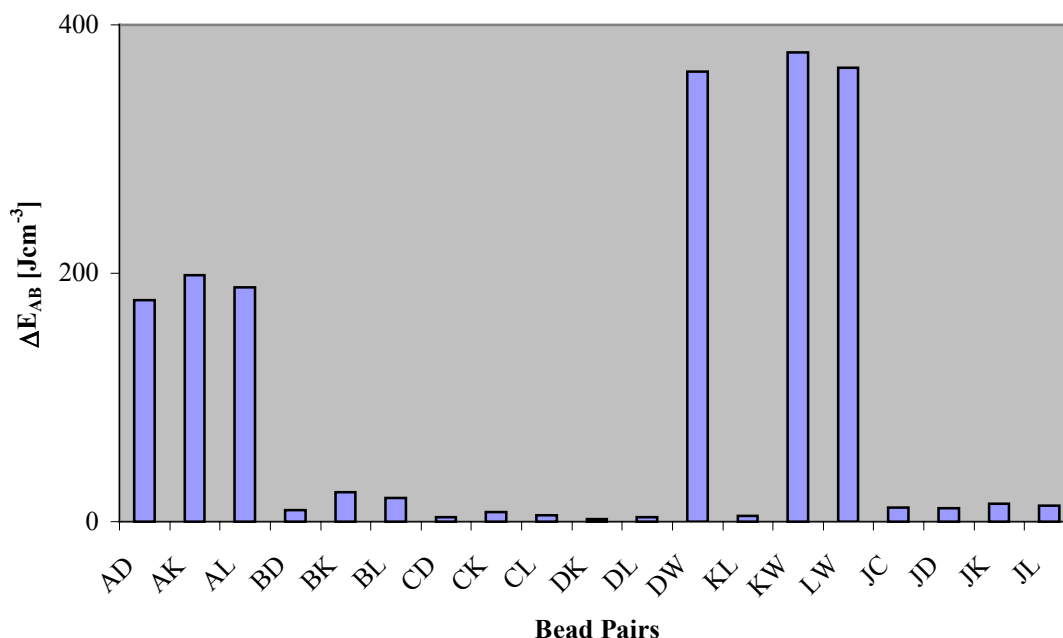
8

As described in Chapter 3.1.1.1 the DPD-model in Figure 35 the beads at the end of the chain represent the most hydrophilic beads with the OH-group (**A**). The poly (ethylene oxide) chain is represented by the second hydrophilic bead (**B**) and the poly (propylene

oxide) chain is presented with the most hydrophobic bead (**J**). The bead distribution is as for the EO₁₃PO₃₀EO₁₃ triblock copolymer in Chapter 3.1.1.

For all bead pairs an average coordination number of 6.5 was estimated as obtained by Monte Carlo simulations⁷⁶.

Figure 36. Pair interaction energies ΔE_{AB} in Jcm^{-3} for the bead pairs of the C₁₀E₄, n-decane, water, PEP5-PEO5 and PPO5-PEO5 system.



The differential pair interaction energies ΔE_{AB} were obtained by Monte Carlo simulations⁷⁶ and are diagrammed in Figure 36, where the x-coordinate shows the different bead pairs and the y-coordinate shows the energy ΔE_{AB} in Jcm^{-3} . The energies for pairs of equal beads were very close to 0 and therefore estimated as such. The interaction energies for the hydrophilic beads **A**, **B** and **J** and the hydrophobic bead **C** are the same as in Figure 13 and 18 and have been explained there. The additional beads **D**, **K**, and **L** are all hydrophobic alkyl chain beads and their behavior is therefore similar to bead **C**. They have high positive interaction energies with the hydrophilic bead **A** and even higher with the

water bead due to the repulsive forces. The hydrophobic beads with each other have very small interaction energies of almost zero because of their similarity. The interaction energies with the slightly hydrophilic **J** bead are still small but a little bit higher and with the even more hydrophilic **B** bead even higher.

All simulations for the boosting effect and the microemulsion formation were carried out at a box side length of about 35nm, all simulations of the lamellar phase with box dimensions of 12nm x 12nm x 57nm. The temperature was 300K and the DPD density was $\rho_{\text{DPD}}=3$, which equals a normal density of $\rho=1 \text{ gcm}^{-3}$. The oil-water-ratio was for all calculations $\alpha=0.422$ and the polymer/surfactant ratio $\delta=5\%$. All simulations were carried out with a starting geometry of an arbitrary bead distribution in the box and the “surfactant” fraction γ was varied.

3.2.1.2 Microemulsion Formation

The experimental phase diagram of such a surfactant/water/oil mixture as shown in Figure 37 shows four different phases at equal volume fractions of water and oil and an increasing surfactant concentration³⁴. The water-oil-ratio as defined in Equation 49 in this phase diagram is $\alpha=0.422$.

$$\alpha = \frac{m(n - decane)}{m(n - decane) + m(water)} \quad 49$$

The C₁₀E₄ (4) fraction γ is described by Equation 50:

$$\gamma = \frac{m(C10E4)}{m(C10E4) + m(n - decane) + m(water)} \quad 50$$

At temperatures lower than 28°C an o/w-microemulsion (2) with excess oil is formed, where oil droplets are covered with the polymer and dissolved in the large water phase. The opposite, a w/o-microemulsion ($\bar{2}$) with water droplets dissolved in the large oil phase occurs with an excess of water at temperatures higher than 32°C. At temperatures between 28°C and 32°C a three-phase region (3) exists, and an excess of water as well as oil and a microemulsion occurs. With increasing surfactant concentration the excess water and oil become less and at a C₁₀E₄ fraction of $\gamma=13.2\%$ (X-point) just one microemulsion phase (1) is visible.

The experimental phase diagram (Figure 37) shows that the three phase region changes to the one phase region at a fraction of 4 of $\gamma=13.2\%$. The simulation results did not reproduce the three-phase region but showed a simple phase separation of water (2) and oil (6). The differences between the simulation and the experimental result from the diverse system sizes. The experimentally found three phases are macroscopic while the phase separation occurs in a “nano-box” and therefore cannot be compared directly. Figure 38 shows the simulation result at a surfactant (alkyl chain beads (C) – green, ethylene

oxide beads (**A**, **B**) - red) (**3**) fraction of $\gamma=7.5\%$ (a) and $\gamma=12\%$ (b) at the interface of the water (blue) and n-decane (white).

Figure 37. Experimental phase diagram of $C_{10}E_4$ in water and n-decane³⁴.

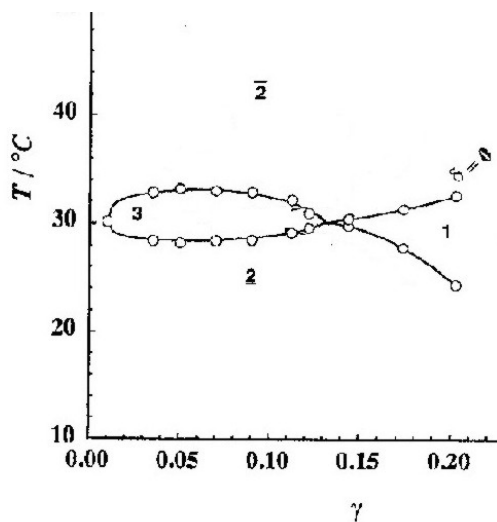
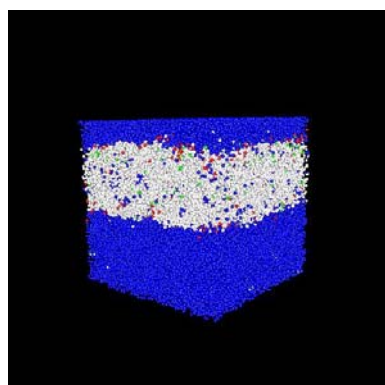
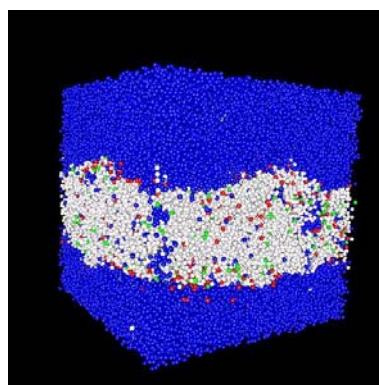


Figure 38. Phase separation of water and n-decane at a $C_{10}E_4$ fraction of $\gamma=7.5\%$ (a) and $\gamma=12.5\%$ (b).



(a)



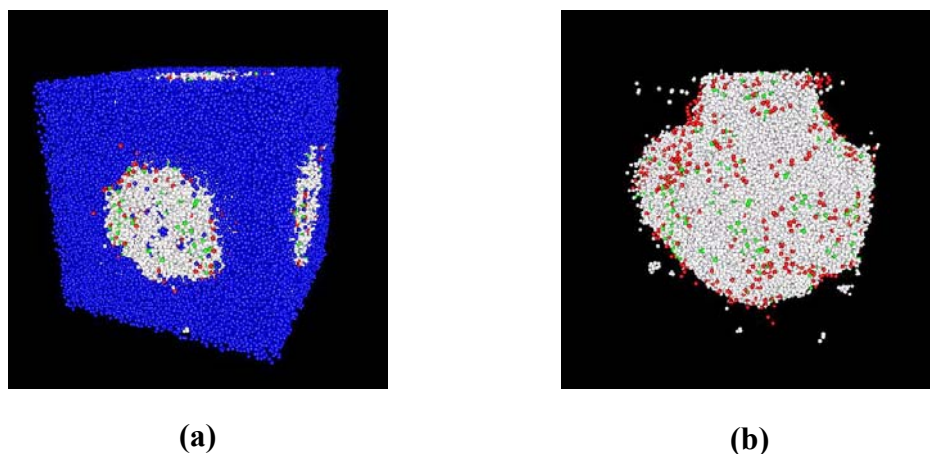
(b)

Figure 38 makes visible how the shape of the interface between oil (6) and water (2) changes with increasing surfactant concentration. While the interface at a $C_{10}E_4$ fraction of $\gamma=7.5\%$ (Figure 38 (a)) is still almost planar it changes with increasing surfactant fraction to a convoluted interface as visible in Figure 38 (b) at a polymer fraction of $\gamma=12.5\%$.

At even higher fractions than $\gamma=14\%$ the simple phase separation changes to a bicontinuous phase. In Figure 39 the structure of the first bicontinuous microemulsion phase is visible, which appears at the lowest $C_{10}E_4$ fraction of $\gamma=15\%$.

The sponge-like structure as shown in Figure 5 (b) is reproduced even though it is not completely visible. The box size limits the view of the bicontinuous phase because of the comparatively small dimensions.

Figure 39. Bicontinuous Phase at a polymer fraction of $\gamma=15\%$. (a) shows the bicontinuous microemulsion phase with water and (b) without.



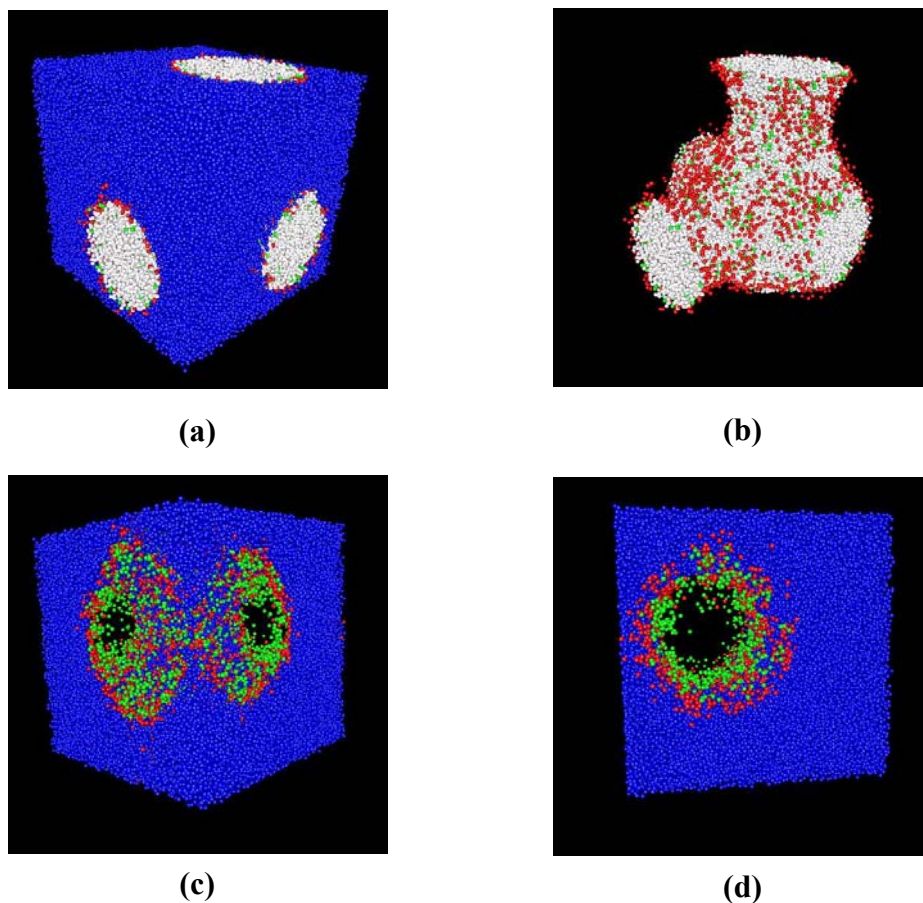
The theoretically found transition fraction from the three to the one phase region (X-point) is at $\gamma=15\%$, which is in remarkable agreement with the experimental value of $\gamma=13.2\%$ $C_{10}E_4$.

At even higher fractions of 3 the formation of the sponge-like structure is even more distinct. Figure 40 shows the bicontinuous microemulsion at a surfactant fraction of

$\gamma=20\%$. Figure 40 (b) points out the tube-like oil phase with the water masked. In Figure 40 (c) and (d) the oil is masked and the tubes in the water phase are visible.

The simulation results shown in Figure 39 and 38 make it now possible to change the molecular structure of either the polymer, the surfactant or the oil easily and investigate the influence on the microemulsion formation.

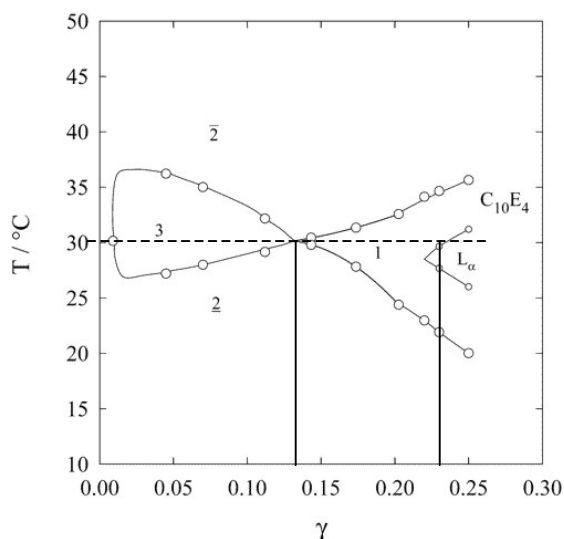
Figure 40. Bicontinuous Phase at a surfactant fraction of $\gamma=20\%$. (a) shows the bicontinuous microemulsion with water and oil and (b) with water masked and (c) and (d) with oil masked.



3.2.1.3 L_α -Phase

The phase behavior of $C_{10}E_4$ (4) (Figure 37) in water (2) and n-decane (6) at different surfactant fractions and the occurring microemulsion formation has been investigated by the means of Dissipative Particle Dynamics in good agreement with the experimental phase behavior³⁴.

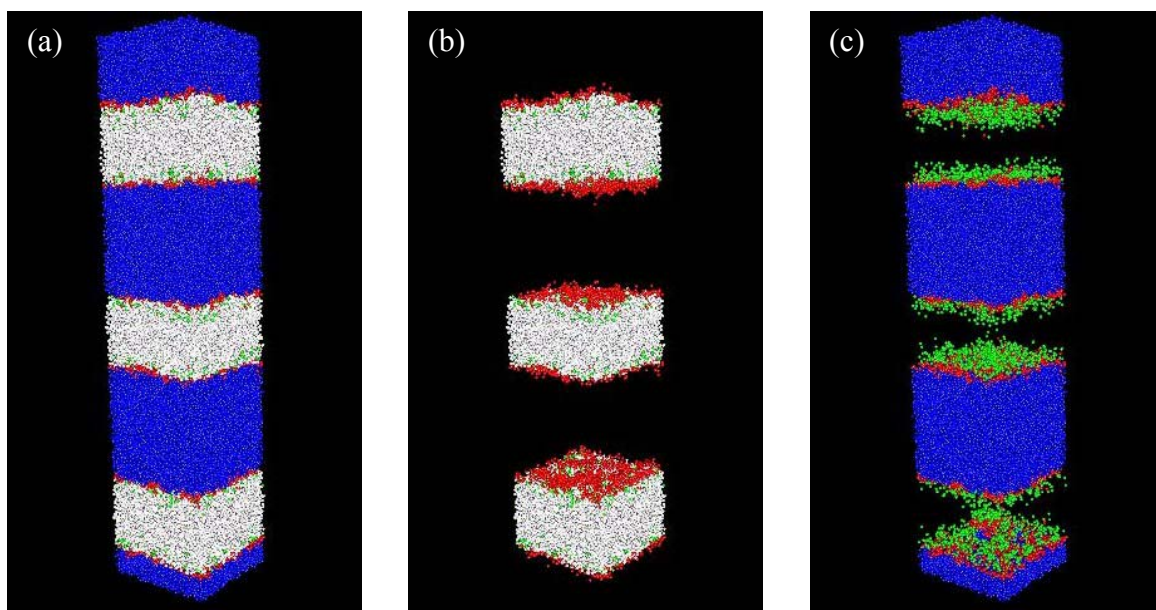
Figure 41. Experimental phase diagram of $C_{10}E_4$ in water and n-decane³⁵.



The experimental phase diagram in Figure 37 can be extended to a fourth phase region³⁵. The microemulsion region (1) changes to a lamellar phase L_α at surfactant fractions higher than $\gamma=23\%$ (Figure 41)³⁵.

The transition from a bicontinuous microemulsion (L_3) to a L_α lamellar phase first occurs in the simulation at a $C_{10}E_4$ fraction of $\gamma=25\%$ which is very close to the experimental value of $\gamma=23\%$. Figure 42 shows the lamellar phase obtained at a surfactant fraction of $\gamma=30\%$. The surfactant (4) alkyl chain beads are green, the ethylene oxide beads are red, the water is blue and the n-decane white.

Figure 42. Lamellar L_α phase at a $C_{10}E_4$ fraction of $\gamma=30\%$. (a) shows the L_α phase with water and oil and (b) with water masked and (c) with oil masked.



The thickness of the oil layer (white) averages to 7.3nm and of the water layer (blue) to 11.8nm, which are close to what might be the experimental values.

Figure 43 shows the formation of the lamellar phase through the DPD simulation. The $C_{10}E_4$ (1) fraction was $\gamma=30\%$ and the pictures are the simulation results taken every 1000 simulation steps which corresponds to 2.4ns. Figure 43 (a) shows the simulation box at the beginning of the DPD calculation with an arbitrary bead distribution. It changes within the first 1000 simulation steps to randomly distributed oil domains (Figure 43 (b)). These oil domains form slowly three indistinct oil layers in the water phase (Figures 43 (c)-(e)), which change to well-defined layers within the next 3000 simulation steps (Figure 43 (f)-(h)). After 7000 steps ≈ 16.5 ns (Figure 43 (h)) the completely developed lamellar phase occurs as already shown in Figure 42.

Figure 43. Formation of the lamellar L_α phase at a $C_{10}E_4$ fraction of $\gamma=30\%$ through the dynamics simulation at different time steps.

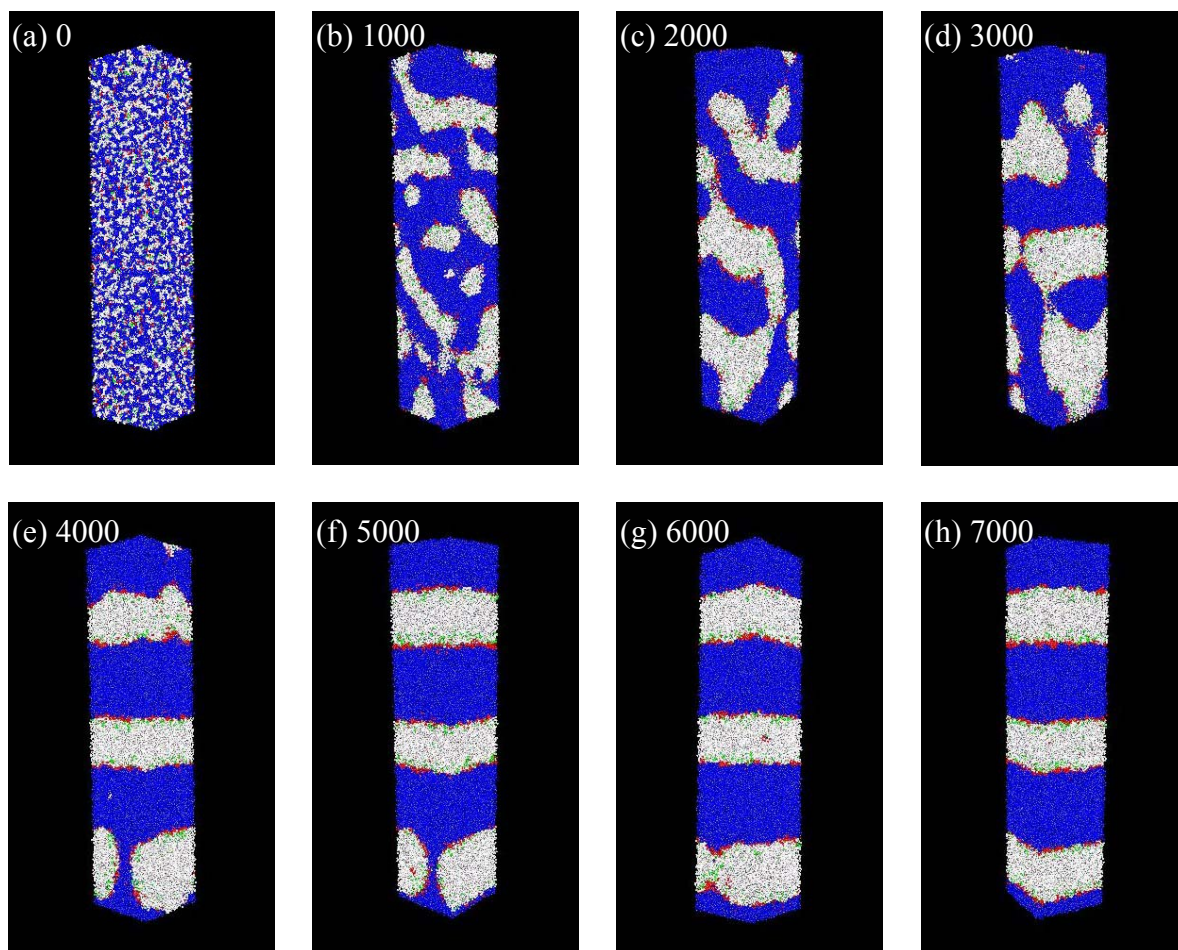
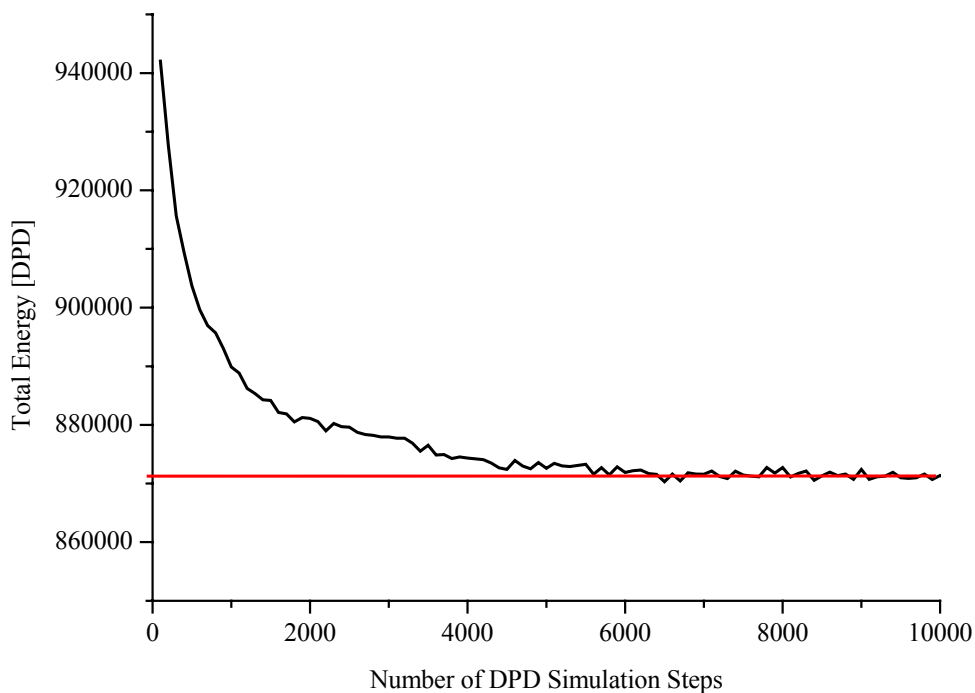


Figure 44 shows the total energy (kinetic and potential energy) of the system progressing with the simulation time. The red line in Figure 44 indicates the average total energy of the system after reaching the thermodynamic equilibrium. The devolution of the total energy with the number of simulation steps shows clearly the way from the absolutely chaotic state at the beginning of the simulation (arbitrary bead distribution) into the thermodynamic equilibrium (L_α phase).

Figure 44. Total energy [DPD units] of the system shown in Figure 43.

The simulation starts with the most unfavored configuration and the highest total energy which drops until the equilibrium is reached at about 6500 simulation steps. Figure 43 (g) shows the system after 6000 steps and the lamellar phase is already formed but still not quite distinct. After 7000 simulation steps (Figure 43 (h)) a well defined L_{α} phase is formed which agrees nicely with the total energy that equilibrated.

3.2.1.4 The Boosting Effect – Addition of PEP5-PEO5

The experimental phase diagrams in Figure 37 and 41 show that the three phase region changes to the one phase region at a fraction of **3** of $\gamma=13.2\%$. The so-called X-point where the one phase region and the three-phase region coincide is a landmark of the efficiency of a surfactant. The addition of small amounts of a poly (ethylene propylene)-*block*-poly (ethylene oxide) block copolymer to the ternary surfactant/water/oil system leads to a shift of the X-point to lower fractions³⁴. The polymer used in the present study is PEP5-PEO5 with $5000\text{g}\cdot\text{mol}^{-1}$ of each the ethylene oxide and the alkyl chain.

The surfactant fraction γ as defined in Equation 31 has been modified to take the polymer into account. Now the total “surfactant” fraction γ is the fraction of the surfactant **3** and the polymer **7**, as shown in Equation 51.

$$\gamma = \frac{m(\text{C}_{10}\text{E}_4) + m(\text{PEP5PEO5})}{m(\text{C}_{10}\text{E}_4) + m(\text{PEP5PEO5}) + m(n - \text{decane}) + m(\text{water})} \quad 51$$

The ratio of polymer (PEP5-PEO5) and surfactant (C_{10}E_4) δ describes the amount of surfactant that has been substituted by the polymer and is shown in Equation 52:

$$\delta = \frac{m(\text{PEP5PEO5})}{m(\text{C}_{10}\text{E}_4) + m(\text{PEP5PEO5})} \quad 52$$

Figure 45 shows the shift of the X-point in the experimental phase diagram with the addition of the polymer **7**. The substitution of 5% of C_{10}E_4 by PEP5-PEO5 moves the X-point from $\gamma=13.2\%$ ($\delta=0\%$, no polymer) to $\gamma=8.75\%$ ($\delta=5\%$).

In the simulations carried out at a fraction of **7** of $\delta=5\%$ the bicontinuous phase first appeared at a total surfactant fraction of $\gamma=10\%$. At lower fractions, as before for the ternary system, a simple phase separation was observed. The simulated X-point of $\gamma=10\%$

is in good agreement with the experimental value of $\gamma=8.75\%$ and the boosting-effect has been reproduced very well by the computer simulation.

Figure 45. Experimental phase diagram of $C_{10}E_4$ and PEP5-PEO5 in water and n-decane³⁴.

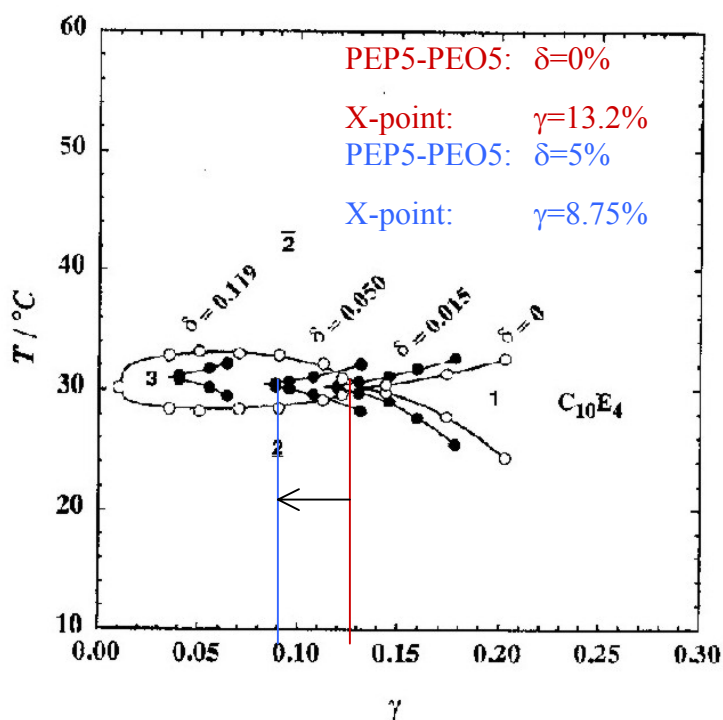


Table 4. Comparison of the X-point fraction: Experiment vs. DPD Simulation.

	$\delta=0\%$	$\delta=5\%$	$\Delta\gamma \delta=0\% \rightarrow \delta=5\%$
$\gamma \text{ exp.}^{34}$	13.2%	8.75%	-4.45%
$\gamma \text{ sim.}$	15%	10%	-5%
error for γ	1.8%	1.25	0.45

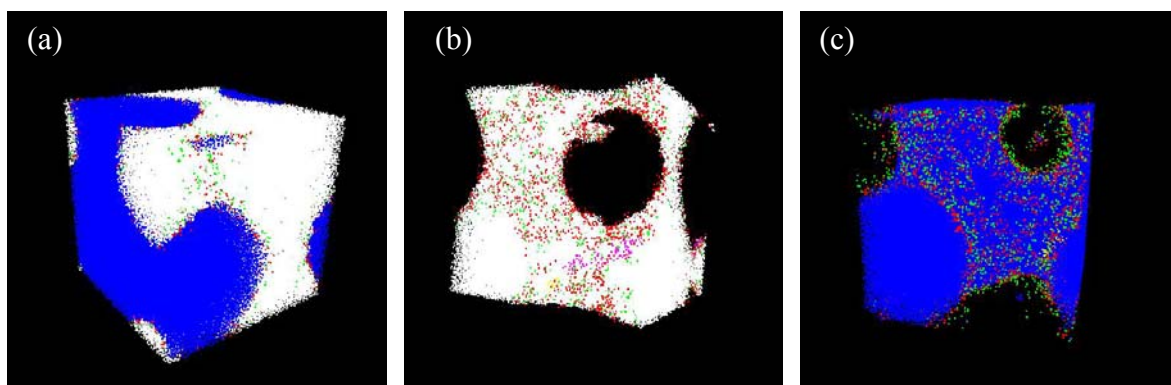
Table 4 shows the comparison of the experimental X-point shift to the simulated. The difference between the simulated and the experimental value for γ for $\delta=0\%$ is 1.8%,

and for $\delta=5\%$ is 1.25. The X-point shifted 4.45% in the experimental investigations and 5.5% in the DPD simulations which is a difference of 0.45%. The overall errors are between 1.8% and 0.45% which represents a remarkable agreement.

Figure 46 shows the structure of the bicontinuous microemulsion formed with $\gamma=10\%$ and $\delta=5\%$: surfactant ($C_{10}E_4$: alkyl chain beads – green, ethylene oxide beads – red; PEP5PEO5: alkyl chain beads – pink, ethylene oxide beads – yellow; water beads: blue; n-decane beads: white).

The shape of the bicontinuous phase has changed in comparison to the structure found in the absence of the polymer as shown in Figure 39 and 40. While the microemulsion of the ternary system shows oil tubes in the water phase, the microemulsion formed by the quaternary system shows as well oil tubes in water as water tubes in oil.

Figure 46. Bicontinuous Phase at a total “surfactant” fraction of $\gamma=10\%$ and a polymer fraction of $\delta=5\%$. (a) shows the bicontinuous microemulsion with water and oil and (b) with water masked and (c) with oil masked.

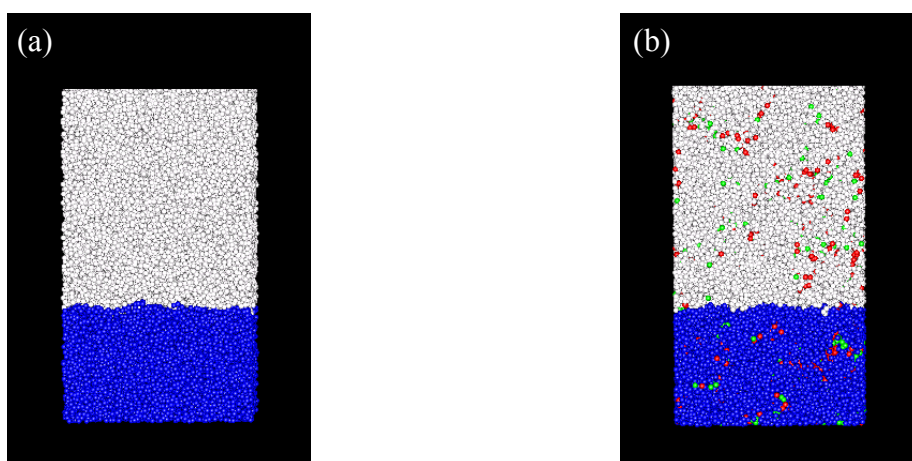


3.2.1.5 Mechanism of the Boosting Effect

The mechanism of the boosting-effect as discussed in the literature is based on two different factors: (1) the replacement of surfactant molecules by the bigger polymer molecules which would not depend significantly on the kind of polymer and (2) the modification of the structure of the bicontinuous microemulsion by smoothing the interface³⁴.

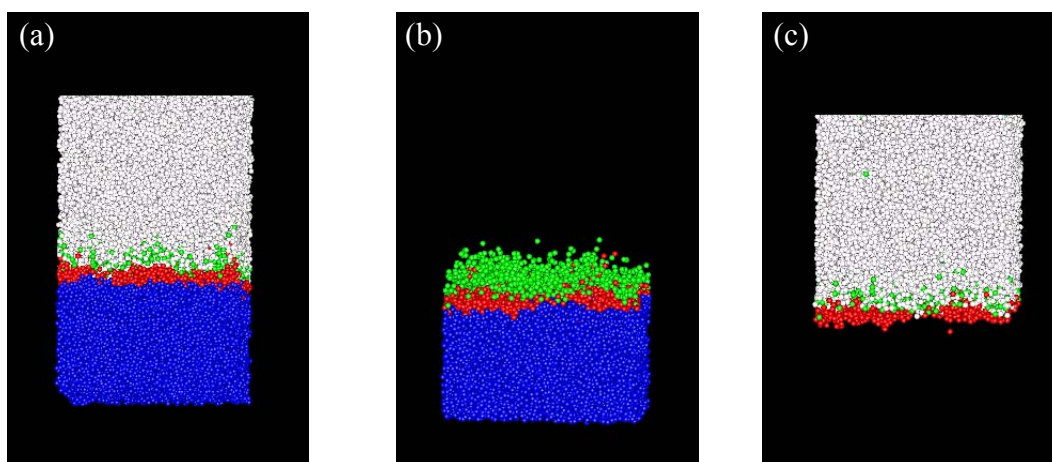
The replacement of the surfactant by the polymer was examined by the simulation setup shown in Figure 47. Figure 47 (a) shows the water and oil layers without any surfactant. To determine the number of $C_{10}E_4$ molecules at the critical micelle fraction, $C_{10}E_4$ molecules were added to the system gradually. Figure 47 (b) shows the system with the surfactant distributed statistically in the water and oil phase.

Figure 47. (a) Water (blue) and oil (white) layers without surfactant. (b) Water and oil layers with the surfactant molecules at the beginning of the calculation.



After the equilibrium was reached the surfactant molecules are located at the water – oil interface. When the number of molecules has reached 400 the interface seems to be completely filled with $C_{10}E_4$ molecules and the first few molecules are in the oil phase. Figure 48 shows the simulation result at a number of 300 $C_{10}E_4$ molecules. All three Figures 48 (a), (b) and (c) show no surfactant molecules in the water or oil phase.

Figure 48. 300 molecules $C_{10}E_4$ with (a) water and oil phase, (b) only water phase and (c) only oil phase visible.



With increasing the number of $C_{10}E_4$ molecules to 400 a single micelle or aggregate is formed with a varying number of surfactant molecules from 2 to 5 (Figure 49). Figure 49 (b) shows a micelle with a few surfactant molecules in the oil phase and Figure 49 (c) shows that there are no molecules in the water phase.

The addition of polymer PEP5-PEO5 molecules to the surfactant – water – oil system as shown in Figure 49 should demonstrate the replacement of surfactant by the polymer. Figure 50 shows the simulation result after the addition of 3 PEP5PEO5 molecules which equals a fraction of $\delta=18\%$ and is therefore more than the PEP5PEO5 fraction necessary for the boosting-effect. The simulations showed that the addition of 3

polymer molecules did not change the number of molecules in the water or oil phase. Figure 50 (b) shows that a few surfactant molecules are located in the oil phase, while the polymer molecules are all three at the interface.

Figure 49. 400 molecules $C_{10}E_4$ with (a) water and oil phase, (b) only water phase and (c) only oil phase visible.

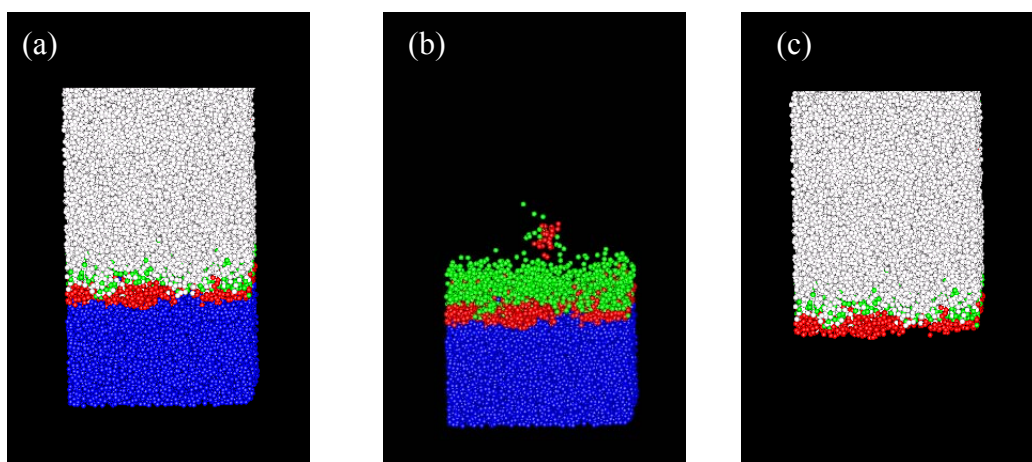
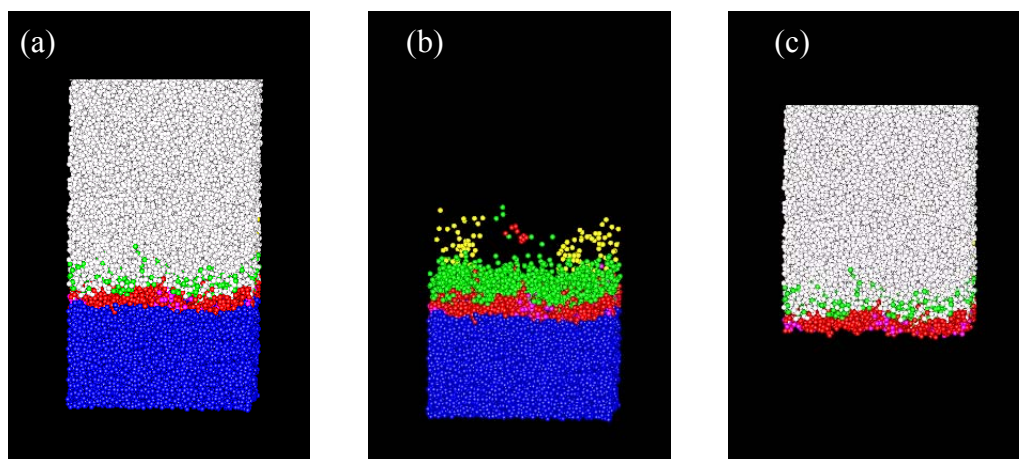


Figure 50. 400 molecules $C_{10}E_4$, 3 molecules PEP5PEO5 with (a) water and oil phase, (b) only water phase and (c) only oil phase visible.



Hence, the replacement of surfactant molecules by polymer molecules at the interface does not seem to play a major role in the boosting-effect.

The modification of the structure of the bicontinuous microemulsion by smoothing the interface by the polymer seems to be the more important part of the mechanism. Figure 51 shows the bicontinuous microemulsion structures at different concentrations. All figures were made by multiplying one box, as shown in Figure 39, to make the structure clearer. The green structure indicates the bicontinuous microemulsion phase (just the surfactant and polymer) of the system with $\gamma=10\%$ and $\delta=5\%$ which is the “boosted” system. The polymer is always shown in red.

Figure 51. Comparison of bicontinuous-structures at different concentrations.

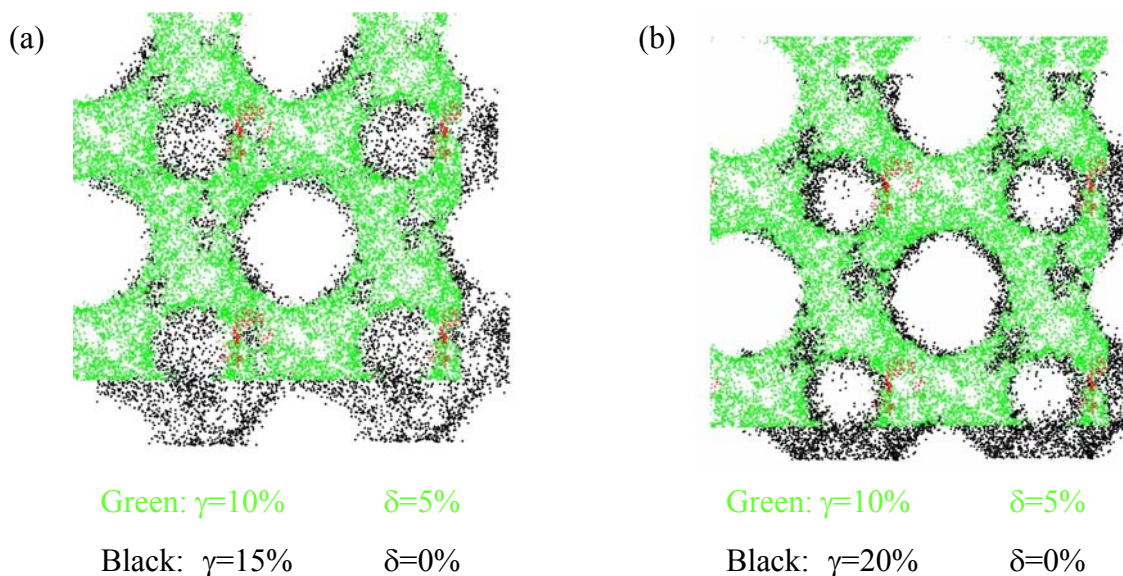


Figure 51 (a) shows the boosted structure in green and the bicontinuous microemulsion phase at a surfactant fraction of $\gamma=15\%$ ($\delta=0\%$) (black) where the bicontinuous microemulsion occurs first. The differences in the structures is obvious. The green structure, containing polymer, is better defined as the polymer free structure (black)

and the “holes” are bigger. The black structure at $\gamma=20\%$ (Figure 51 (b)) resembles the green structure better and the “holes” are of similar size which indicates that the structure at $\gamma=20\%$ ($\delta=0\%$) equals the structure with $\gamma=10\%$ and $\delta=5\%$. It is more surfactant needed to obtain the same structure.

The simulation results shown in Figure 48, 49 and 50 as well as the structural study shown in Figure 51 suggest that the smoothing of the interface plays the major role in the boosting-effect and not the replacement of surfactant molecules by the polymer.

3.2.1.6 Addition of PPO5-PEO5

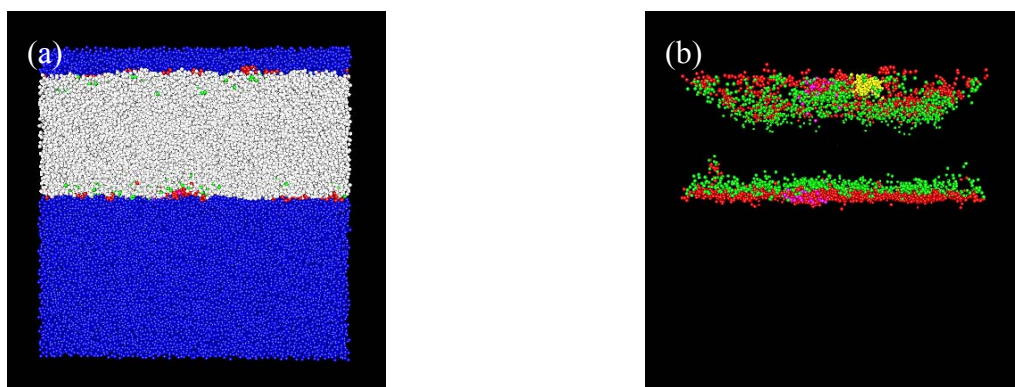
The boosting-effect has experimentally not been observed with poly (ethylene oxide) – *block* – poly (propylene oxide) copolymers³⁶. According to these experiments the boosting-effect should also not occur in the DPD computer simulations if the polymer PEP5-PEO5 is being substituted by a PPO5-PEO5 block copolymer due to the higher hydrophilicity of the propylene oxide in comparison to the alkyl chain.

To investigate the structural behavior of the $C_{10}E_4$ – water – n-decane system with addition of a poly (ethylene oxide) – *block* – poly (propylene oxide) copolymer simulations were carried out with $\delta'=5\%$ of a copolymer with 114 ethylene oxide units and 85 propylene oxide units substituting the alkyl chain of the PEP5-PEO5. The bicontinuous phase did not appear at lower surfactant fractions than $\gamma=15\%$ with the PPO5-PEO5 polymer as observed for the PEP5-PEO5. At lower fractions than $\gamma=15\%$ a simple phase separation was found.

Figure 52 shows the phase separation of the modified system with $\gamma=10\%$ and a PPO5-PEO5 polymer fraction of $\delta'=5\%$ which corresponds to the fraction of the first bicontinuous microemulsion phase in the PEP5-PEO5 system. The $C_{10}E_4$ alkyl chain beads are green, the $C_{10}E_4$ ethylene oxide beads are red, the PPO5-PEO5 propylene oxide beads are pink and the PPO5-PEO5 ethylene oxide beads are yellow. The water beads are as

always blue and the n-decane beads white. In opposite to the alkyl chain of the PEP5-PEO5 which was stretched out into the oil phase (Figure 50) the propylene oxide chain of the PPO5-PEO5 diblock sticks to the surface (yellow).

Figure 52. Phase structure at a surfactant fraction of $\gamma=10\%$ and a PPO5-PEO5 polymer fraction of $\delta'=5\%$. (a) shows the whole system and (b) the system with water masked and oil masked.



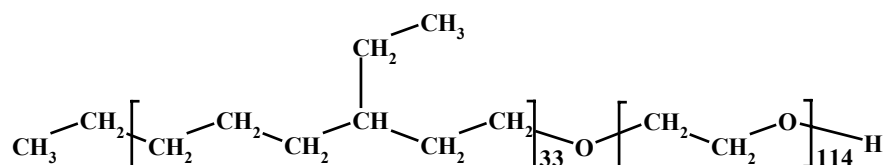
The DPD simulations reproduced the experiments and did not give a boosting effect for the PPO5-PEO5. This proves the DPD method to be sensible for this kind of polymer and the aggregation behavior.

3.2.2 Poly (ethylene butylene)-*block*-poly (ethylene oxide) in Water and Methyl Cyclohexane

3.2.2.1 Simulation Conditions

The diblock copolymer contains an alkyl chain, 3725 gmol^{-1} , which includes 67 ethylene and 33 butylene units statistically distributed. The hydrophilic ethylene oxide part of this polymer contains 114 ethylene oxide units and has a molar mass of 5033 gmol^{-1} (Figure 53).

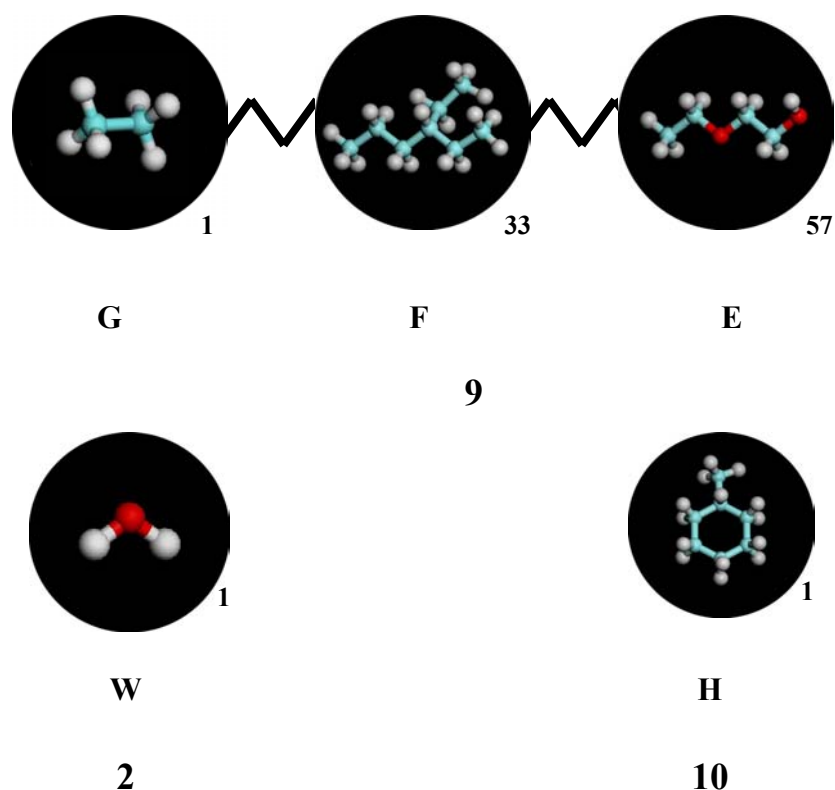
Figure 53. Poly (ethylene butylene)-*block*-poly (ethylene oxide) (9) with 67 ethylene, 33 butylene and 114 ethylene oxide units.



9

Figure 54 shows the DPD-particles (beads) for the investigated system. Water (2) as well as the oil methyl cyclohexane (10) is always represented by one bead. The polymer is divided into two parts, the hydrophobic and the hydrophilic chains, which are themselves represented by several beads.

In this investigation the beads were chosen to be bigger as in the investigations before to prove the variability of the method in the bead size.

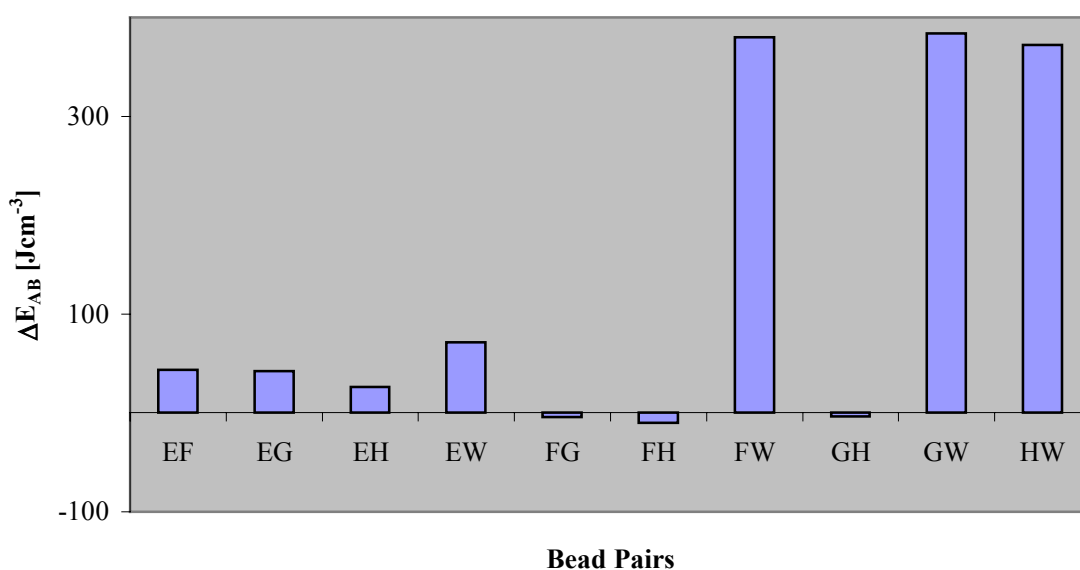
Figure 54. Schematic representation of the simulation model.

The differential pair interaction energies ΔE_{AB} were obtained by Monte Carlo simulations⁷⁶ and are diagrammed in Figure 55, where the x-coordinate shows the different bead pairs and the y-coordinate shows the energy ΔE_{AB} in Jcm^{-3} . The energies for pairs of equal beads were very close to 0 and therefore estimated as such. Figure 21 makes the differences in the behavior of different bead pairs visible. All hydrophobic beads (**F**, **G**, **H**) have high positive values with water (**W**) due to their repulsive behavior. The hydrophilic beads (**E**) have lower positive interaction energies and mix therefore better with water. In contrary the hydrophobic beads of the polymer (**G**, **F**) have slightly negative energies with the oil beads (**H**).

The fact that the ethylene oxide bead (**E**) has a slightly higher interaction energy with water than with oil points seems to be inconsistent with its hydrophilic behavior. However, the interaction energies of the hydrophobic part (**F**, **G**) with water (**W**) is higher

by orders of magnitude and causes a strong repulsion, while the interactions of the ethylene oxide (E) with water (W) and oil (H) are of similar magnitude.

Figure 55. Pair interaction energies ΔE_{AB} in Jcm^{-3} for all bead pairs of the poly ethylene butylene poly ethylene oxide, methyl cyclohexane, water system.



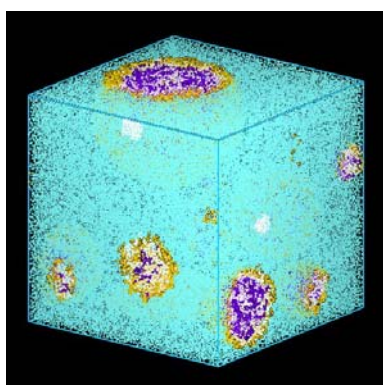
All simulations were carried out at 300K and a box side length of about 35nm with a DPD density of $\rho_{\text{DPD}}=3$, which equals a normal density of $\rho=1 \text{ gcm}^{-3}$. Simulations of all water/oil ratios at a certain polymer concentration of 0.12mol% were achieved. All simulations were carried out with an arbitrary bead distribution in the box at the beginning of the calculation.

3.2.2.2 Results

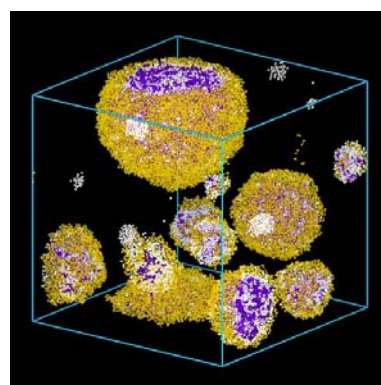
The theoretical phase diagram of such a polymer/water/oil mixture as shown in Figure 5 shows three regions of distinguishable phases^{1,109}: the o/w-microemulsion (o/w), where oil droplets are covered with the polymer and dissolved in the large water phase, the opposite, a w/o-microemulsion with water droplets dissolved in the large oil phase and the bicontinuous phase (L_3) at equal fractions of water and oil.

The simulation results of the microemulsion formation of $C_{10}E_4$ in n-decane and water were in exceptional agreement with the experiment. It was experimentally impossible to investigate microemulsions of the system: Poly (ethylene butylene)-*block*-poly (ethylene oxide) (**9**) diblock copolymer in water (**2**) and methyl cyclohexane (**10**). Therefore a theoretical study of the phase behavior was carried out to determine if a microemulsion formation with such a polymer is in principle possible. The experimental problems could be the effect of insufficient kinetics in the formation process.

Figure 56. o/w-emulsion at a polymer concentration of 0.12mol% and a water/oil ratio of 8:1.



(a)

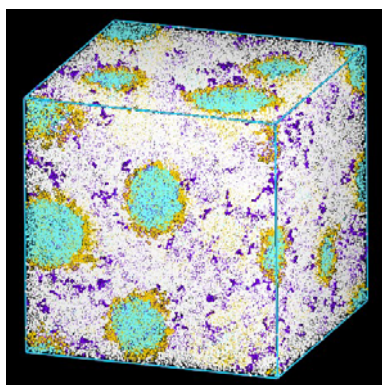


(b)

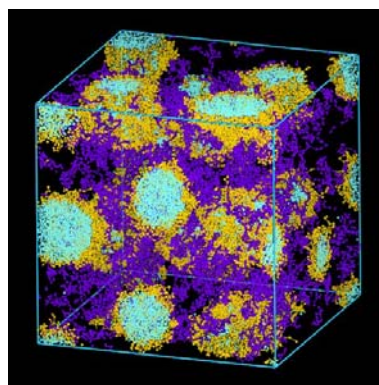
Figure 56 shows the result of the simulation carried out at a water/oil ratio of 8:1. At this ratio oil droplets (methyl cyclohexane beads - white) form in the water phase (water beads – blue) with the polymer (alkyl chain beads – purple, ethylene oxide beads – yellow) at the interface. In Figure 56 (b), where the water was removed in the visualization, the differences in the behavior of the alkyl chain and the ethylene oxide chain are visible. While the alkyl chain is sprawled out into the oil, the ethylene oxide chain remains at the interface.

As shown in the theoretical phase diagram as well as in Figure 57 an emulsion of the w/o-type is formed at an excess of oil. In Figure 57 (a) the simulation result with a polymer concentration of 0.12mol% and a water/oil ratio of 1:8 is visualized with all components. In Figure 57 (b) the oil was made invisible and it shows as mentioned before the sprawled alkyl chain while the ethylene oxide remains at the interface and builds a rim around the water droplet.

Figure 57. w/o-emulsion at a polymer concentration of 0.12mol% and a water/oil ratio of 1:8.



(a)

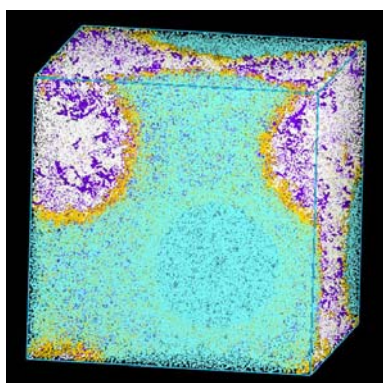


(b)

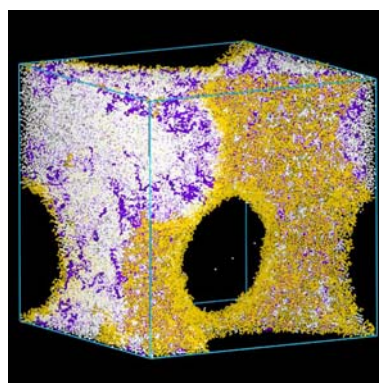
At equal concentrations of water and oil the simulation shows the formation of a bicontinuous phase as shown in Figure 58. In Figure 58 (b) the water was removed and the tube like structure, as depicted in Figure 5 (b), is visible. The box size is too small to show the whole structure as in Figure 5 (b) but the agreement is still distinct.

To my knowledge and from personal communication with J. Venzmer³⁷ the formation of a microemulsion could not be observed experimentally, while the formation of a bicontinuous microemulsion phase with Dissipative Particle Dynamics suggests that the structures found in the simulations are microemulsions. The fact that DPD is based on a thermodynamic model, which in principle should not allow the formation of a kinetically stabilized phase, supports the proposal of the existence of a microemulsion rather than an emulsion. The formation of a microemulsion in the simulation can be explained with the starting point geometry. The completely homogeneous distribution of all beads at the beginning of the calculation is energetically very unfavorable and therefore the system quickly falls into an energy minimum. This is not comparable with the experimental starting point, where the kinetics of the polymers is probably too slow to build a microemulsion.

Figure 58. Bicontinuous emulsion at a polymer concentration of 0.12mol% and a water/oil ratio of 1:1.



(a)



(b)

3.3 Self-Aggregation at the Water-Air Surface

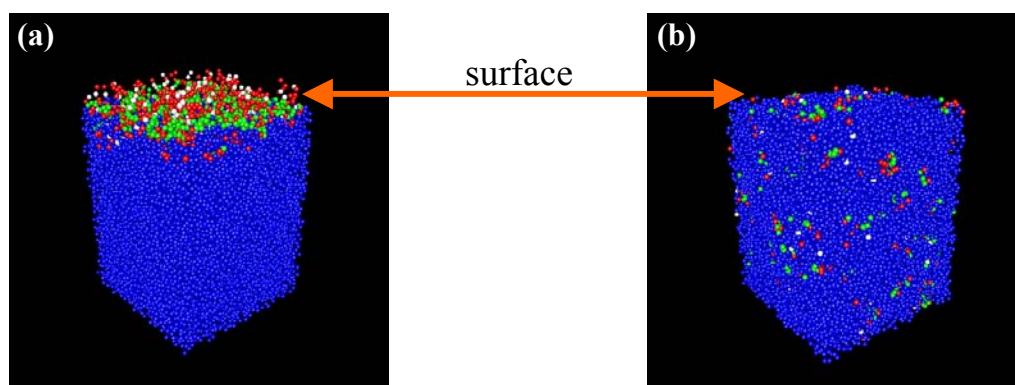
3.3.1 Simulation of the Surface Tension of $C_{10}E_4$, $C_{12}E_5$ and $C_{12}E_6$

3.3.1.1 Simulation Conditions

Another interesting observation of the self-aggregation of amphiphilic surfactants is the behavior at the water-air interface.

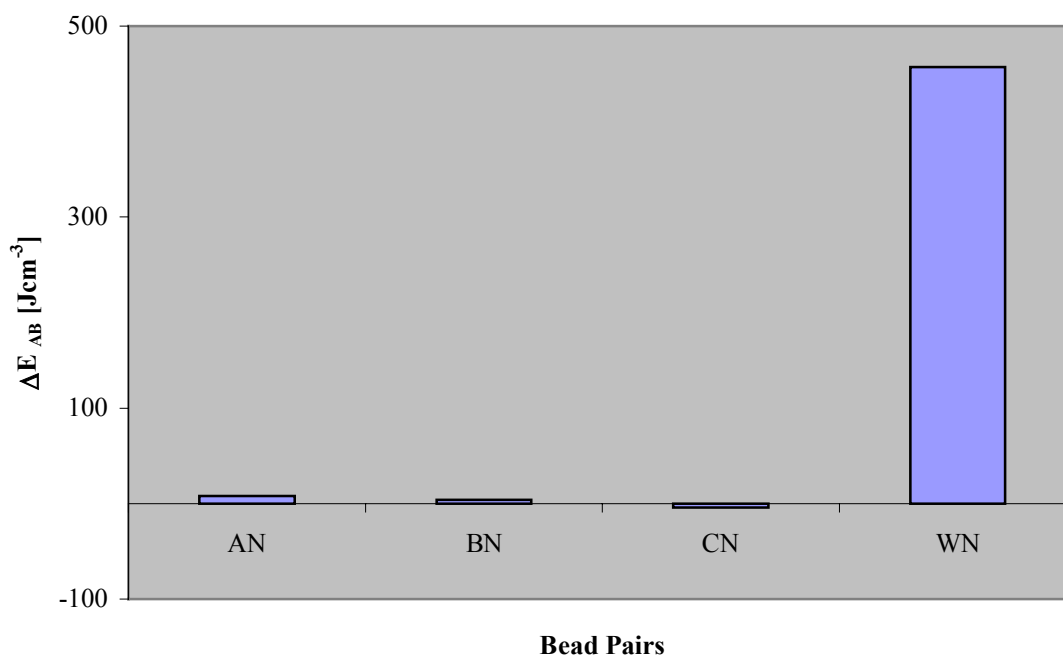
The calculation of the surface tension with Dissipative Particle Dynamics makes the introduction of air necessary. The air beads are represented by N_2 molecules. The interaction parameters a_{ij} with the surfactants have been calculated as described above in the Theory section while the interaction between water and air has been assumed to be highly repulsive in order to create a surface. The air-air interactions were regarded to be non-existent according to the ideal gas theory. The remaining interactions are the same as used in the calculations for the phases in water. For all bead pairs a coordination number of 6.5 was estimated as obtained by Monte Carlo simulations⁷⁶.

Figure 59. Starting configurations with surfactants (a) at the air/water surface and (b) in the water phase.



All simulations were carried out at 300K and a box side length of about 11.5nm x 11.5nm x 28.6nm with a DPD density of $\rho_{\text{DPD}}=3$, which equals a normal density of $\rho=1\text{gcm}^{-3}$ and were started with separated water and air layers. For all concentrations two simulations have been carried out. One with the surfactant distributed in the water (Figure 59 (b)) and one with the surfactant at the air/water surface (Figure 59 (a)) at the beginning of the calculation. After a certain number of simulation steps both starting configurations always led to the same simulation result which is the thermodynamic equilibrium. In Figure 59 the water and surfactant beads have the same colors as already explained in Figure 20. The air beads are not shown in this view.

Figure 60. Pair interaction energies ΔE_{AB} in Jcm^{-3} for the interaction of air with water and the surfactant molecules.



The structures of v(4), C_{12}E_5 (5) and C_{12}E_6 (6) and the DPD model are shown in Figure 17 and 16. The pair interaction energies are the same as in Figure 18 for the surfactants with water. The interaction energies of air with the surfactants and water are

shown Figure 60. The interaction energies of the surfactant beads (**A**, **B**, **C**) with the air beads (**N**) are almost zero due to the almost non-existing interaction.

3.3.1.2 Calculation of the Surface Tension

For the simulation of the surface tension and the *critical micelle concentration* (*cmc*) the concentration has been increased constantly.

For the simulations at concentrations below the *critical micelle concentration* (*cmc*) all surfactant molecules were adsorbed at the air – water surface. Figure 61 shows the thermodynamic equilibrium of 100 $C_{10}E_4$ molecules in the box. Figure 61 (a) shows the whole system and (b) the system without the water. The view of the surface (Figure 61 (c)) shows that the surface is not yet completely filled with $C_{10}E_4$ molecules. The simulations for $C_{12}E_5$ and $C_{12}E_6$ gave analogous results for concentrations below the critical micelle concentration.

With reaching the *critical micelle concentration* the surface is completely covered with surfactant molecules and with exceeding the *cmc* micelles are formed in the water phase. Figure 62 (a) shows the system in the thermodynamic equilibrium with 400 $C_{10}E_4$ molecules in the solution which is significantly above the *cmc* indicated by the surfactant molecules in the water phase. In Figure 62 (b) the water phase was taken out of the view. Figure 62 (c) shows the surface which is almost completely covered in comparison to Figure 61 (c), where the surface was not completely covered with $C_{10}E_4$ molecules. The simulations for $C_{12}E_5$ and $C_{12}E_6$ gave analogous results for concentrations above the critical micelle concentration.

The simulation results showed the first aggregation in the water phase for $C_{10}E_4$ at 300 molecules, for $C_{12}E_5$ and $C_{12}E_6$ at 200 molecules.

Figure 61. Simulation results of $C_{10}E_4$ with a concentration below the *cmc* (100 molecules).

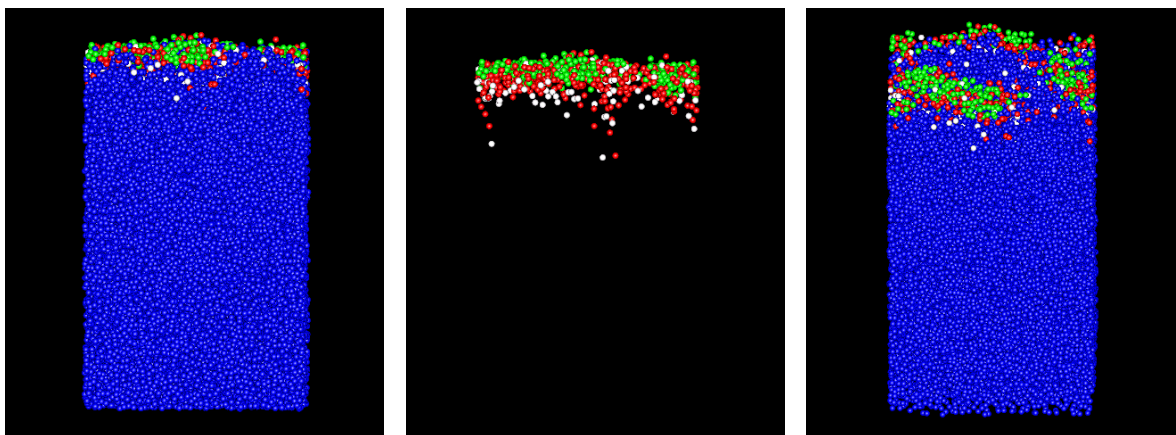
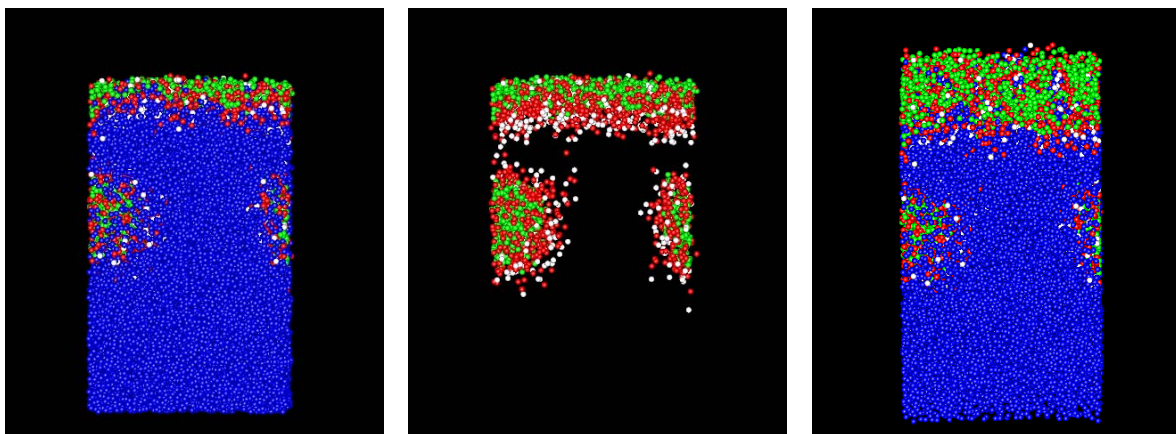


Figure 62. Simulation results of $C_{10}E_4$ with a concentration above the *cmc* (400 molecules).



The corresponding graphs of the calculated surface tension in dependence of the surfactant concentration are shown in Figure 63. For all three surfactants $C_{10}E_4$, $C_{12}E_5$ and $C_{12}E_6$ the surface tension drops as long as the surface is not completely covered with molecules. For $C_{12}E_5$ and $C_{12}E_6$ the gradient of the surface tension becomes zero at 200 molecules and for $C_{10}E_4$ at 300 molecules which agrees nicely with the observation made in the structures for the molecules where the first micelle formation was found to be at the same concentrations. The variation of the surface tension after reaching the *cmc* is due to a

slightly different number of molecules at the surface. For $C_{10}E_4$ the *cmc* was found to be at 300 molecules and varies for higher concentrations between about 290 and 310 molecules at the surface. Analogous investigations were made for $C_{12}E_5$ and $C_{12}E_6$.

Figure 63. Graph of the calculated surface tension of $C_{10}E_4$, $C_{12}E_5$ and $C_{12}E_6$ in DPD units.

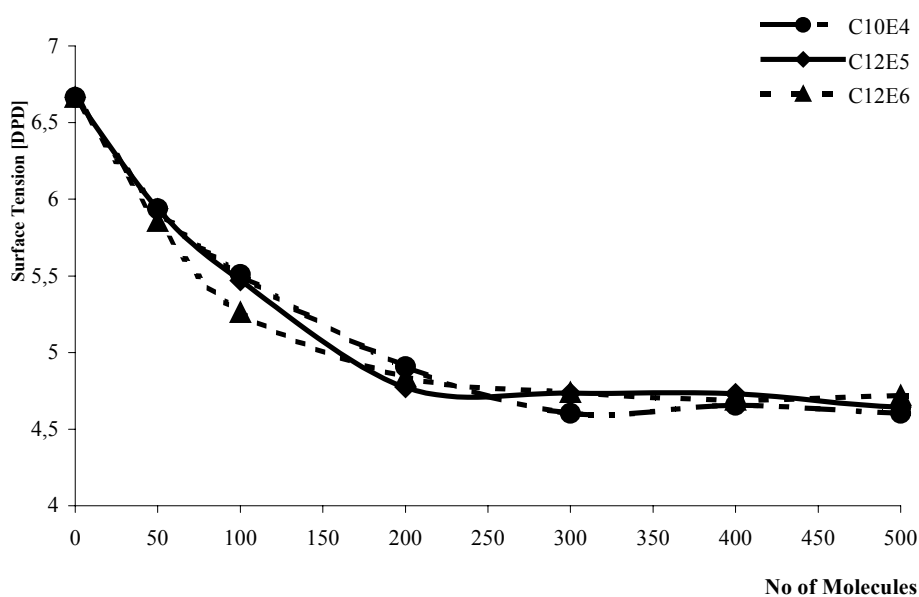


Figure 64 shows a schematic graph of the surface tension in Figure 63 where just two points for each molecule were plotted: The surface tension without any surfactant and the surface tension at the *cmc*. The comparison of the three different surfactants shows that $C_{12}E_5$ and $C_{12}E_6$ give nearly the same result for the *cmc* and the corresponding surface tension. $C_{10}E_4$ has a higher *critical micelle concentration* and a lower corresponding surface tension.

Figure 64. Schematic graph of the calculated surface tension of $C_{10}E_4$, $C_{12}E_5$ and $C_{12}E_6$ in DPD units.

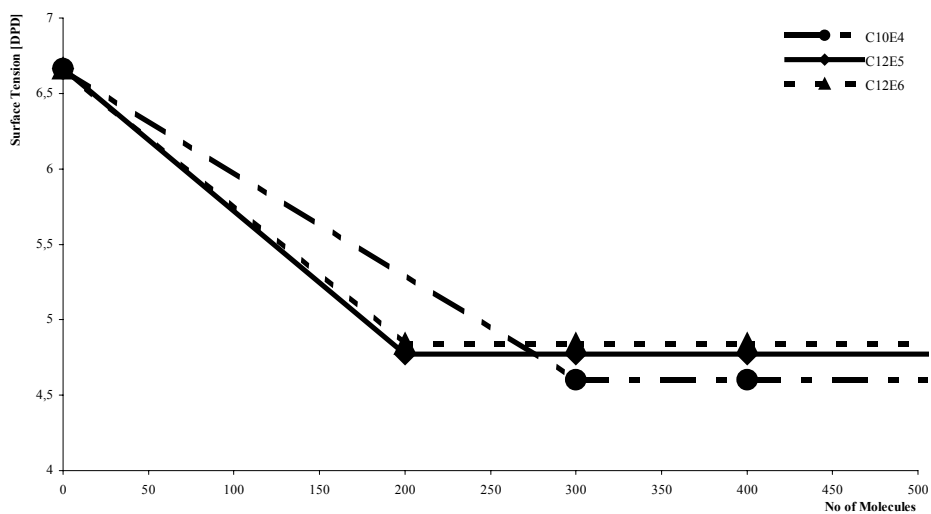
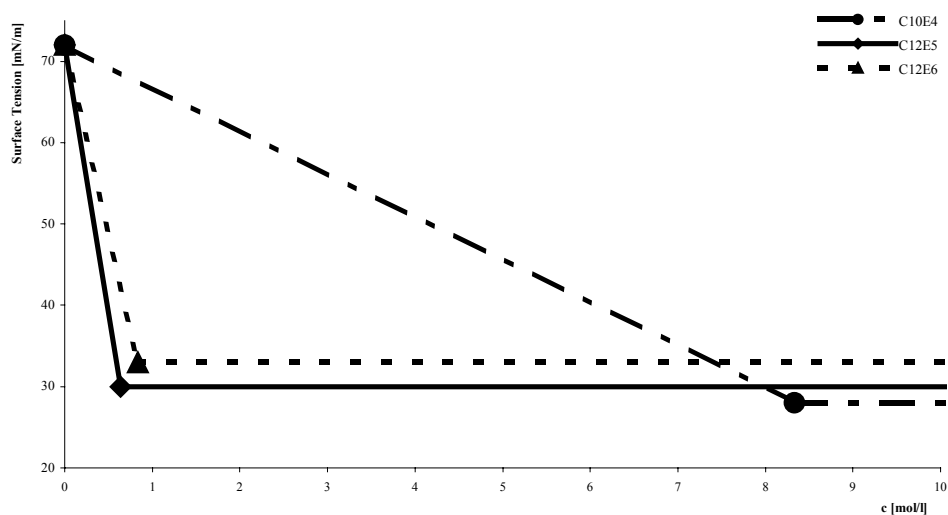


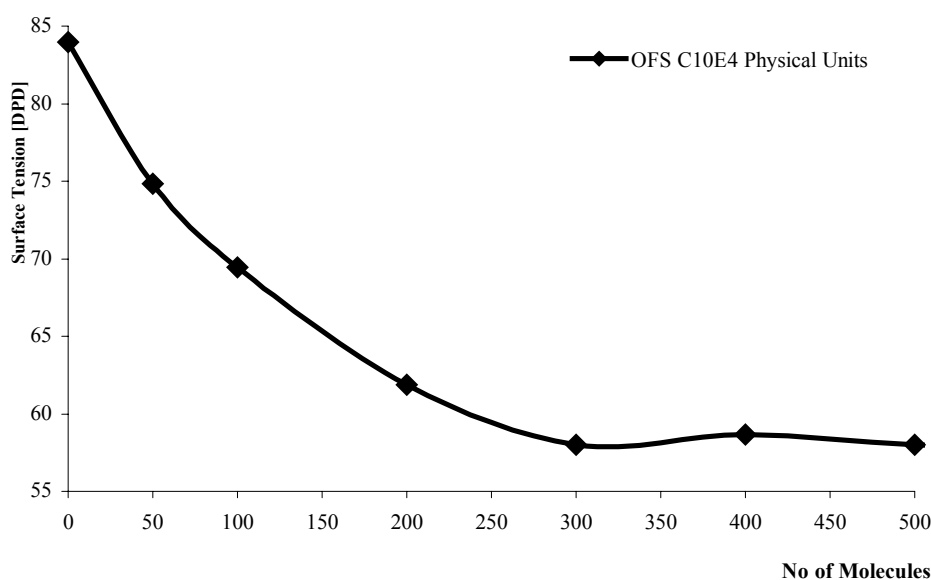
Figure 65. Schematic graph of the experimental surface tension of $C_{10}E_4^{110}$, $C_{12}E_5^{111}$ and $C_{12}E_6^{110}$.



The experimental schematic graph of the surface tension of the three surfactants is shown in Figure 65. It shows the same characteristics as the simulated graph in Figure 64. $C_{10}E_4$ has a clearly higher *cmc* with a lower surface tension than $C_{12}E_5$ and $C_{12}E_6$ which have a very similar *cmc* and surface tension.

The calculated results in Figure 64 and the experimental result in Figure 65 are qualitatively in good agreement.

Figure 66. Calculated Surface Tension of $C_{10}E_4$ after conversion to physical units.



The surface tension calculated with Dissipative Particle Dynamics σ_{DPD} in DPD units can be converted to physical units $[mN m^{-1}]^{44}$. Figure 66 shows the calculated surface tension of $C_{10}E_4$ as shown in Figure 63 after the conversion to physical units. The experimental surface tension of pure water¹¹⁰ is $72 mN m^{-1}$. The value calculated with DPD after conversion is $84 mN m^{-1}$. The experimental surface tension of $C_{10}E_4$ at the *cmc*¹¹⁰ is $28 mN m^{-1}$ and the calculated one $57 mN m^{-1}$. The calculated surface tension of water without any surfactant is in very good agreement with the experimental value. The

decrease of the surface tension in the simulations is not as high as in the experiment. It is still in acceptable agreement due to the very small simulation box and the many simplifications and negligences of the simulation model. Figure 64 and 65 proves that the experiments are qualitatively very well reproduced and Figure 66 shows that even the quantitative agreement is appropriate.

3.3.1.3 Calculation of the Minimum Area per Molecule

To support these results qualitatively the minimum area per molecule was calculated for C₁₀E₄, C₁₂E₅ and C₁₂E₆ and compared with the experimental values as published. For C₁₂E₅ and C₁₂E₆ experimental values were available and both showed a very good agreement with the experimental values (Table 5). The area on the interface used by a single surfactant molecule at the *cmc* is the minimum area per molecule. It is a characteristic value for the surfactant. The minimum area per molecule for C₁₀E₄ was calculated to 0.435 nm², for C₁₂E₅ to 0.4378 nm² and for C₁₂E₆ to 0.656 nm². The experimental values are 0.501 nm² for C₁₂E₅¹¹¹ and 0.67 nm² for C₁₂E₆³².

Table 5. Minimum area per Molecule at the air/water surface of C₁₀E₄, C₁₂E₅ and C₁₂E₆. The experimental values are put in parentheses.

Surfactant	Minimum Area per Molecule
C ₁₀ E ₄	0.435 nm ²
C ₁₂ E ₅	0.438 nm ² (0.501 nm ²) ¹¹¹
C ₁₂ E ₆	0.656 nm ² (0.67 nm ²) ³²

4 Summary

The mesoscopic simulation technique Dissipative Particle Dynamics has been previously proved to simulate the phase behavior of amphiphilic surfactants in water and interfacial tensions of surfactant-water-oil systems in good agreement with the experimental results. The investigated systems were either amphiphiles with distinct strong hydrophilic and hydrophobic parts (DDAO) or the parameter calculation was not discussed ($C_{12}E_6$ in water).

This work showed that the parameter calculation used is suitable for even more complicated systems. The application of Dissipative Particle Dynamics studies of amphiphilic surfactants in aqueous solution has been successfully extended to the complicated poly (ethylene oxide) *-block-* poly (propylene oxide) *-block-* poly (ethylene oxide) triblock copolymers. The computationally achieved phase diagram of $EO_{13}PO_{30}EO_{13}$ in water at 300K was in remarkable agreement with the experimental phase diagram and showed the micellar, hexagonal, lamellar and inverse micellar phase.

The less complicated surfactants $C_{10}E_4$, $C_{12}E_5$ and $C_{12}E_6$ have been investigated with DPD to yield structural data of the observed phases. I have successfully applied Dissipative Particles Dynamics to simulate the self-assembly of $C_{10}E_4$ and $C_{12}E_5$ in water. It was possible to distinguish between the isotropic L_1 and L_2 phases as well as the lamellar L_α phase. The simulated bilayer thickness of $C_{10}E_4$ was $\epsilon_{sim}=4.9nm$ which is in good agreement with the experimental value of $\epsilon_{exp}=5.0nm\pm 0.5nm$. The micellar aggregation number for $C_{10}E_4$ was calculated to 53 ± 10 molecules. The bilayer thickness and aggregation number for $C_{12}E_5$ and $C_{12}E_6$ were calculated as well. $C_{12}E_5$ gave a simulated bilayer thickness of $\epsilon_{sim}=6.3nm$ in comparison to an experimental value of $\epsilon_{exp}=6.0nm$ and a micellar aggregation number of 98 ± 14 . The simulated bilayer thickness of $C_{12}E_6$ was $\epsilon_{sim}=7.7nm$ and the simulated micellar aggregation number was 79 ± 16 which is very close to the experimental value of 87. This structural investigation proved that the DPD method

is not just suitable to reproduce the phase behavior of amphiphilic surfactants and polymers qualitatively but also quantitatively.

The DPD simulation of microemulsion systems has not been compared in the literature with experimental results but was applied on model surfactants. The Dissipative Particles Dynamics method to simulate the self-assembly of $C_{10}E_4$ in water has been successfully used. It was possible to distinguish between the w/o, o/w and bicontinuous microemulsions as well as the lamellar L_α . The simulation results of $C_{10}E_4$ in water and n-decane are in good agreement with the experimental phase diagram.

The X-point shift has been found at a concentration very close the experimental value. The simulation of the quaternary system $C_{10}E_4$ /PEP5-PEO5/water/n-decane did also match the experimental results very well and the boosting-effect was found computationally with DPD. The possibility to easily modify the polymer as well as the surfactant to observe the influence of these changes to the so-called X-point opens up a great opportunity to many industrial applications. The X-point characterizes the efficiency of a surfactant in washing processes. The simulation results of the X-point shift from $\gamma=15\%$ ($\delta=0\%$) to $\gamma=10\%$ ($\delta=5\%$) are in remarkable agreement with the experimental values. The boosting-effect could not be observed by adding a PPO5-PEO5 diblock copolymer which agrees with the experimental results where these systems also did not show an X-point shift.

It was now possible to get a detailed insight into the mechanism of the boosting-effect with this novel computer simulation technique. Experiments suggested that the mechanism of the boosting-effect is more likely based on the modification of the structure of the bicontinuous microemulsion phase by smoothing the interface caused by the polymer. The replacement of surfactant molecules by the bigger polymer molecules which would not depend significantly on the kind of polymer is not important. The computer simulations support the assumption that the change of the bicontinuous microemulsion structure caused by the polymer molecules play the major role in the mechanism and that the replacement of surfactant molecules by the polymer is not as important.

It was also possible to calculate the experimentally unknown phase behavior of poly (ethylene butylene)-*block*-poly (ethylene oxide) diblock copolymer in water and methyl cyclohexane. The three different phases found like oil-in-water, water-in-oil droplets and a bicontinuous microemulsion phase, as well as the character of the thermodynamic model, indicate the formation of a microemulsion in this polymer/water/oil system. The DPD method has been applied to an experimentally uninvestigated system for the first time and produced interesting results. With these new insights in the phase behavior of the polymer – water – oil system many new applications are possible.

The introduction of the air beads into the DPD methods opens up a wide range of new applications. For the first time the surface tension has been calculated with Dissipative Particle Dynamics while the systems published in the literature just dealt with interfacial tension between two condensed phases. The shape of the experimental surface tension diagram of C₁₀E₄, C₁₂E₅ and C₁₂E₆ at the water – air interface has been reproduced with DPD. In the simulated as well as in the experimental graphs C₁₀E₄ has a clearly higher *cmc* with a lower surface tension than C₁₂E₅ and C₁₂E₆ which have very similar *cmc* and surface tension. The conversion of the DPD surface tension to physical units shows an acceptable agreement. Together with the qualitative agreement of experiments and simulations the quantitative comparison makes predictions of surface tension of unknown surfactants and polymers possible.

All calculation results are in remarkable agreement with the experimental data. In the present work the applications of the method have been extended significantly. The simulation of simple surfactant-water systems has been used to obtain structural information. Oil has been added and even microemulsion formations of ternary and quaternary systems have been observed. A completely new field – the DPD calculation of the surface tension – has been opened by the introduction of air beads.

The DPD method proved to be a reliable tool to get a better understanding of the nanostructure of self-assemblies and structural information. It was even possible to investigate an experimentally unknown system and the method is therefore applicable to

support the often complicated experiments or even to obtain experimentally unavailable data. With this method it is easily possible to predict the properties of compounds and in this way to avoid expensive experiments by suggesting promising candidates for certain industrial applications. To our knowledge DPD is a unique method to simulate mesoscopic structures on a relatively long time scale based on an intermolecular interaction level.

5 Outlook

Amphiphilic systems are still of great interest for many applications e.g. in cosmetics, food or paint and varnish industry. The simulation of these system has developed immensely in the last decade. Due to the increasing power of computer hard and software this development is going to improve even quicker in the future. The treatment of bigger systems and longer simulation time opens up a wide range of new tasks.

To continue the present work many different topics are possible. For example the recently published introduction of charges¹¹² and Coulomb interactions in the DPD model extends the simulations from nonionic surfactants to the wide range of ionic surfactants and the influence of salts. The effect of salt addition to microemulsion systems e.g. is a field of great interest with many applications which could so far not been investigated with mesoscopic computer simulations.

A completely new field of interest is the self- aggregation of nano particles in the condensed phase and the interaction with polymers, surfactants and lipids. The investigation of latter has come into focus of recent research. Dissipative Particle Dynamics studies have focused in the past on material science and the introduction of problems from bio and life science to DPD is an interesting new area with a great potential.

This work proved the parameter calculation and the DPD simulation with them to be reliable. Hence, one can now predict the self-assembly and properties of nonionic amphiphilic surfactant and polymer system in the condensed phase and at the surface. The modification of known systems and their effect on the behavior can be investigated easily and without expensive experiments.

Dissipative Particle Dynamics is a reliable tool for mesoscopic simulations and has, with the implementation of new features, a great potential for many research studies in the academic and industrial field.

6 Appendix

6.1 Hard- and Software

All simulations were carried out on a Linux cluster with 32 AMD Athlon MP 1600+ dual processors. The DPD software used is a development of AlCove Molecular Dynamics GmbH based of the code of Frenkel¹ with major modifications. The DPD parameters were calculated as described in the theory section with a software as well developed by AlCove Molecular Dynamics GmbH.

6.2 Concentration Conversions

Due to the different number of molecules in one bead the DPD concentration need to scaled according to this number. The DPD concentration $c_{DPD}(I)$ of a component I is the product of the mole percent $n\%(I)$ of this component, the number of water molecules in such a bead $K(I)$ and the total number of beads N in the simulation box (Equation 53):

$$c_{DPD}(I) = n\%(I) \cdot K(I) \cdot N \quad 53$$

The relation between the calculated volume of water $V_c(W)$ and the calculated volume $V_c(I)$ of the other beads $K(I)$ is defined by Equation 54:

$$K(I) = \frac{V_c(I)}{V_c(W)} \quad 54$$

6.3 Abbreviations and Variables

Table 6. Variables and constants of DPD unit conversion.

Variable	Definition	Value [units]
\tilde{v}_i	estimated velocity	-
g	out-of-plane vibration	-
ξ	fiction coefficient	-
α	oil weight fraction	-
γ	surfactant weight fraction	-
δ	polymer weight fraction	-
ρ_{DPD}	DPD density	3
σ_{DPD}	DPD surface tension	DPD units
σ_{exp}	reversible surface work	-
ϵ_{exp}	experimental bilayer thickness	-
ρ_{local}	local density function	-
σ_{phys}	Calculated surface tension	mN m ⁻¹
ϵ_{sim}	simulated bilayer thickness	-
A	area	-
A	surface area	-
a, b, c	box side lengths	[Å]
A_{box}	box surface area	[Å ²]
$a_{DPD}, b_{DPD}, c_{DPD}$	DPD box side lengths	-
a_i	acceleration of particle i	-
au	atomic mass unit	1.66054 · 10 ⁻²⁷ kg
b	bond	-
BD	Brownian Dynamics	-
$c_{DPD}(I), c_{DPD}(J), \dots$	DPD concentration of component I, J, ...	-
cmc	critical micelle concentration	-

Appendix

<i>COMPASS</i>	Condensed-Phase Optimized Molecular Potentials for Atomistic Simulation Studies	-
<i>DDAO</i>	dodecyl dimethyl amine oxide	-
<i>DPD</i>	Dissipative Particle Dynamics	-
E_{AB}	pair contact energy	-
E_{total}	total potential energy	-
E_{inter}	non-bond potential (inter molecular energy)	-
E_{intra}	bond potential (intra molecular energy)	-
<i>ESR</i>	electron spin resonance	-
F	free energy	-
F_C	conservative force	-
F_D	dissipative force	-
F_i	force of particle i	-
F_{inter}	inter molecular force	-
F_{intra}	intra molecular force	-
F_{mix}	free mixing energy	-
F_R	random force	-
F_S	harmonic spring force	-
f_v	free energy density of DPD liquid	-
G	Gibb's free energy	-
H	enthalpy	-
H	hexagonal phase	-
<i>IR</i>	infra red	-
k	dimensionless compressibility	-
$K(A), K(B), \dots$	relation between the volume of water and the volume of other beads	-
k_B	Boltzmann constant	$1.38066 \cdot 10^{-23} \text{ J K}^{-1}$
K_D	proportional constant	-
K_S	spring constant	-
k_T	isothermal compressibility	-
L'	bicontinuous phase	-
L_α	lamellar phase	-
L_1	isotropic phase (micellar)	-

Appendix

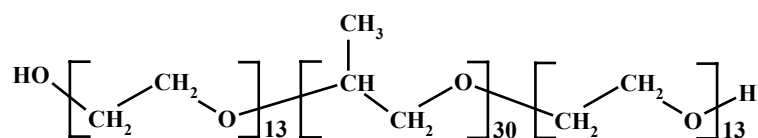
L_2	isotropic phase	-
L_3	bicontinuous microemulsion	-
LD	Langevin Dynamics	-
m	average mass of all beads	[g]
$m(A), m(B), \dots$	mass of bead A, B, ...	[g]
MC	Monte Carlo	-
MD	Molecular Dynamics	-
m_i	mass of particle i	-
n	total number of beads	-
n	numerical density of the molecules	-
$n\%(I), n\%(J), \dots$	mol percent of component I, J, ..	-
N_A, N_B, \dots	number of monomers in molecule A, B, ..	-
NMR	nuclear magnetic resonance	-
n_{steps}	number of simulation steps	-
o/w	oil in water	-
p	pressure	-
$P(E_{AB})$	probability function of pair interaction energies	-
$QSAR$	Quantitative–Structure–Activity–Relationship	-
R	gas constant	$8.31451 \text{ J K}^{-1} \text{ mol}^{-1}$
r_c	cut-off radius in the DPD simulation	[Å]
r_i	distance vector; coordinates of particle i	-
S	entropy	-
T	temperature	298 K
t	time	-
$t(n_{step})$	simulation time of n_{step} simulation steps	[s]
t_{DPD}	DPD simulation time	-
t_{step}	time step size	0.05
$V(smallest)$	molecular volume of smallest bead	[Å ³]
$V(W)$	experimental molecular volume of water	30 Å^3
V_{box}	box volume	[Å ³]
$V_c(A), V_c(B), \dots$	calculated volume of bead A, B, ...	[Å ³]

Appendix

$V_c(W)$	calculated volume of water	[Å ³]
v_i	velocity of particle i	-
w	work	-
w/o	water in oil	-
Z	coordination number	-
γ_{DPD}	dissipative coefficient	-
ΔE_{AB}	differential pair interaction energy	-
Δt	time step	-
θ	torsion angle	-
θ_{DPD}	random variable	-
λ	predictor-corrector facto	-
ρ	density of the DPD fluid	-
ρ_{DPD}	DPD density	-
σ	amplitude of statistical noise	-
σ_{DPD}	DPD surface tension	-
φ	bond angle	-
$\varphi_A, \varphi_B, \dots$	mole fraction of component A, B, ...	-
χ	Flory-Huggins interaction parameter	-
ω^D	variable of the friction coefficient	-
ω^R	variation of the random force with the distance	-

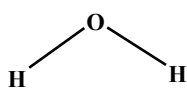
6.4 Molecules

- (1) Poly (ethylene oxide)-*block*-poly (propylene oxide)-*block*-poly (ethylene oxide):
EO₁₃PO₃₀EO₁₃



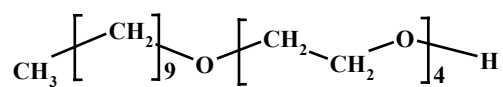
1

- (2) Water



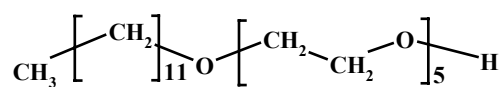
2

- (3) *n*-decyl tetraoxyethylene glycol ether:
C₁₀E₄



3

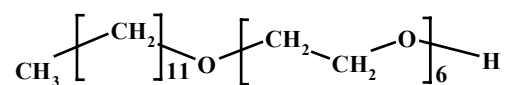
- (4) *n*-dodecyl pentaoxyethylene glycol ether:
C₁₂E₅



4

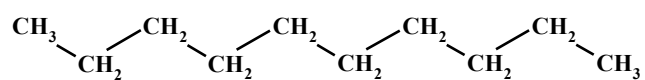
(5) *n*-dodecyl hexaoxyethylene glycol ether:

C₁₂E₆



5

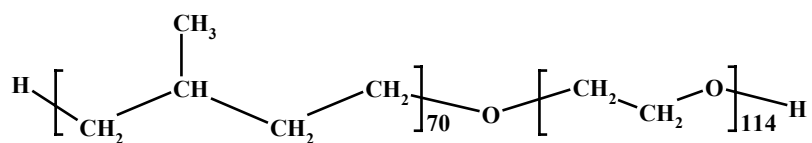
(6) *n*-decane



6

(7) Poly (ethylene propylene)-*block*-poly (ethylene oxide)

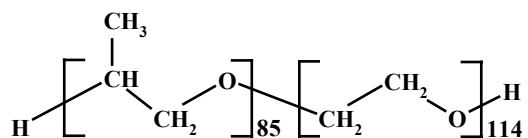
PEP5-PEO5



7

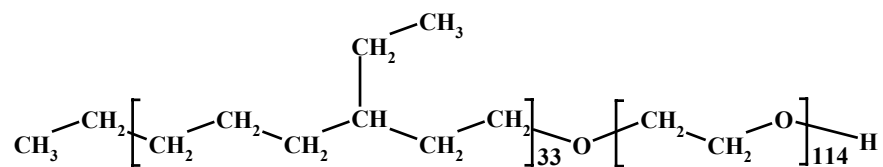
(8) Poly (propylene oxide)-*block*-poly (ethylene oxide)

PPO5-PEO5



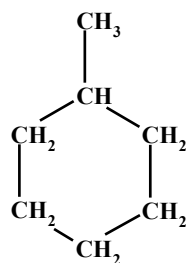
8

(9) Poly (ethylene butylenes)-*block*-poly (ethylene oxide)



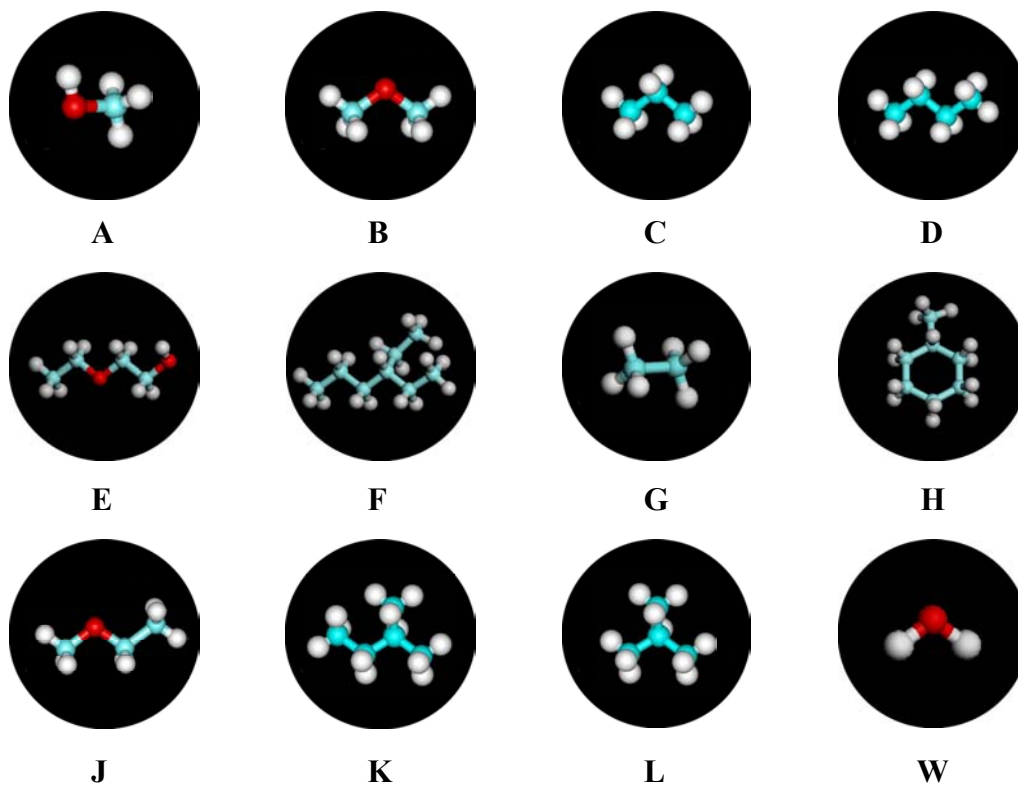
9

(10) Methyl cyclohexane

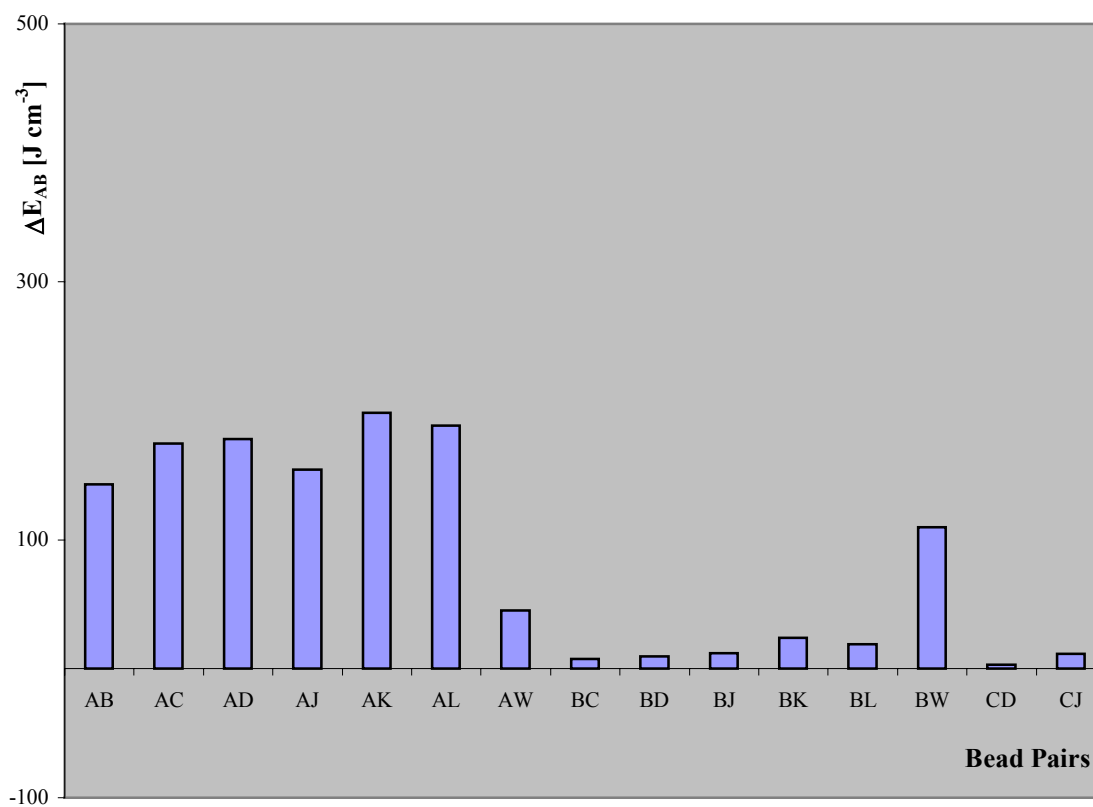


10

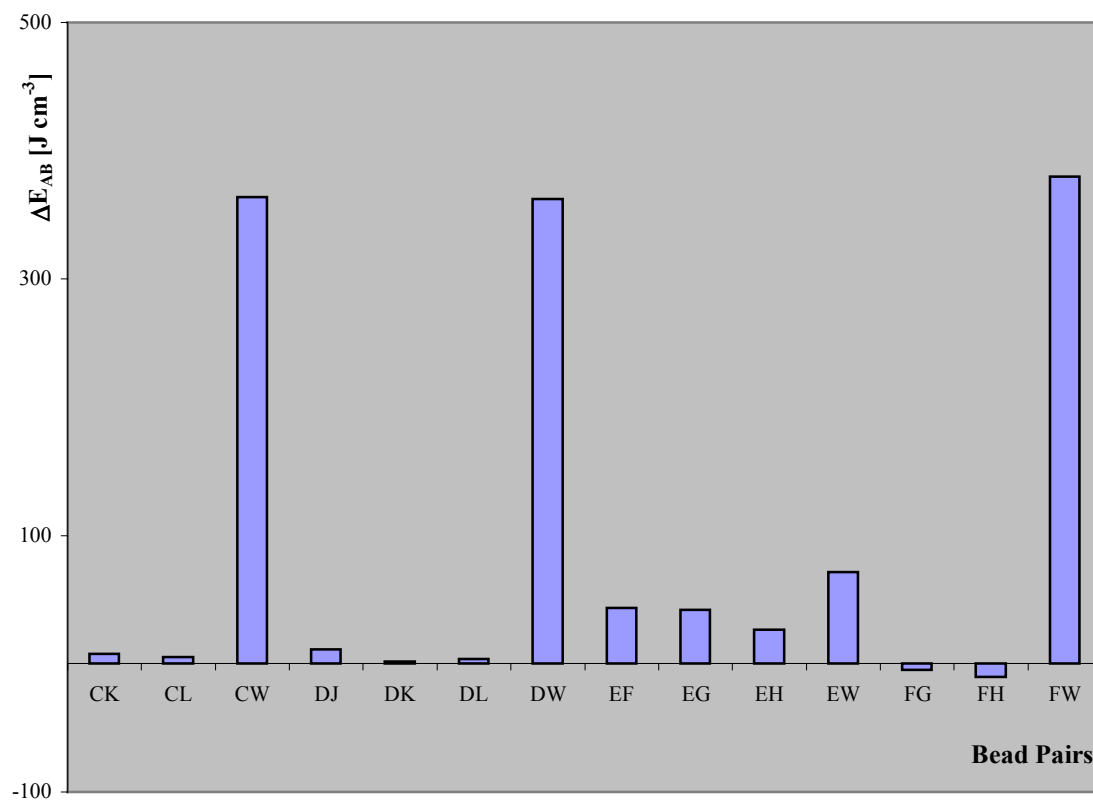
6.5 Beads and Interaction Energies



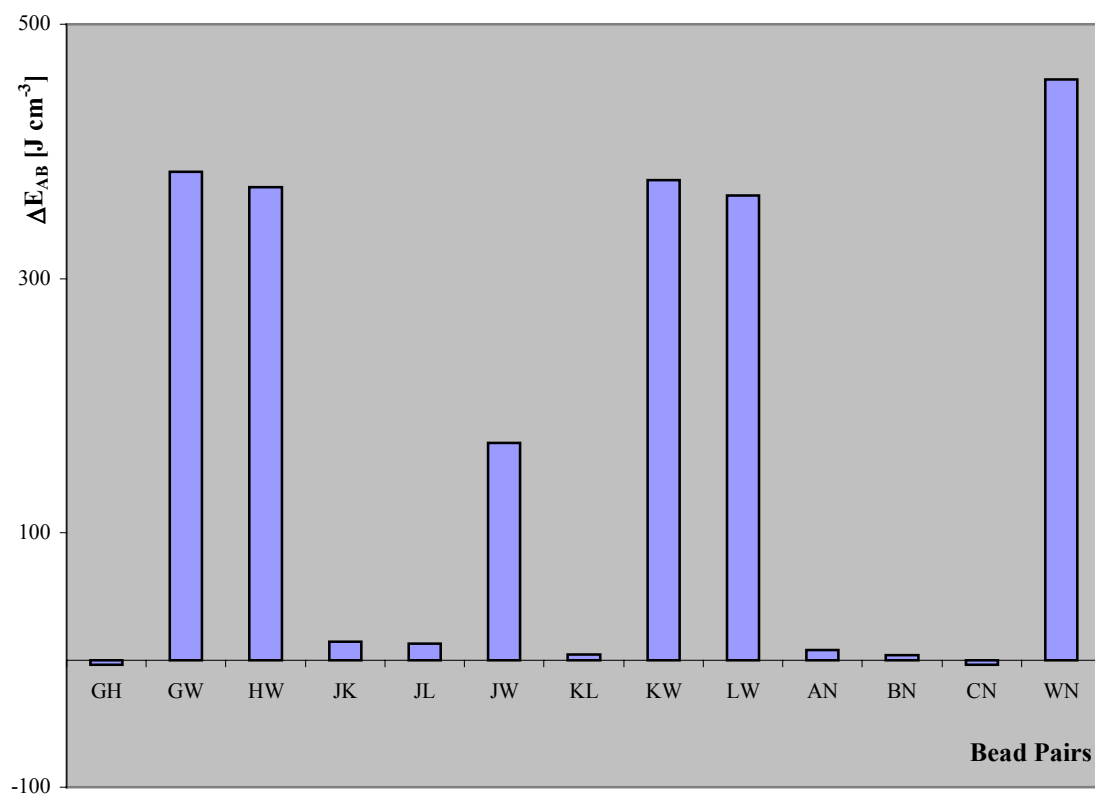
Differential Bead Pair Interaction Energies ΔE_{AB}



Differential Bead Pair Interaction Energies ΔE_{AB}



Differential Bead Pair Interaction Energies ΔE_{AB}



6.6 List of Figures

Figure 1.	Schematic DPD-model of an amphiphilic polymer in water.	9
Figure 2.	Pair interaction energy calculation.	25
Figure 3.	Coordination Number Calculation Z_{AB} .	28
Figure 4.	Phase behavior of surfactants in aqueous solution at different concentrations.	35
Figure 5.	Theoretical phase behavior of a water-oil-surfactant system at a constant surfactant concentration ¹ .	38
Figure 6.	Electron microscopy picture of bicontinuous microemulsion ¹ .	39
Figure 7.	Phase behavior of a water-oil-surfactant system at constant water/oil ratio.	40
Figure 8.	Forces at the surface and in the volume phase.	41
Figure 9.	Schematic adsorption of surfactants at the surface.	42
Figure 10.	Schematic graph of the surface tension.	43
Figure 11.	Structure of poly (ethylene oxide) -block- poly (propylene oxide) -block- poly (ethylene oxide) $EO_{13}PO_{30}EO_{13}$ (1).	45
Figure 12.	DPD-model of poly (ethylene oxide)- <i>block</i> -poly (propylene oxide)- <i>block</i> -poly (ethylene oxide) $EO_{13}PO_{30}EO_{13}$ (1) in water (2).	46
Figure 13.	Pair interaction energies ΔE_{AB} in Jcm^{-3} for all bead pairs of the $EO_{13}PO_{30}EO_{13}$ - water system.	47

Figure 14.	EO ₁₃ PO ₃₀ EO ₁₃ (1) experimental phase diagram and simulation results at 300K at (a) 20wt%, (b) 50wt%, (c) 70wt% and (d) 90wt% polymer in water.	50
Figure 15.	Simulation results at 60 wt% EO ₁₃ PO ₃₀ EO ₁₃ . (a) shows the L' phase with water and (b) without.	51
Figure 16.	Structure of C ₁₀ E ₄ (3) and C ₁₂ E ₅ (4).	52
Figure 17.	Schematic representation of the simulation model for C ₁₀ E ₄ (3) and C ₁₂ E ₅ (4).	53
Figure 18.	Pair interaction energies ΔE_{AB} in Jcm ⁻³ for all bead pairs of the C ₁₀ E ₄ , C ₁₂ E ₅ and C ₁₂ E ₆ - water system.	53
Figure 19.	Experimental phase diagram of C ₁₀ E ₄ (3) in water ²⁹ .	54
Figure 20.	Simulation results at a C ₁₀ E ₄ concentration of (a) 35wt%, (b) 75wt% and (c) 95wt%.	55
Figure 21.	Formation of the lamellar phase at 75wt% C ₁₀ E ₄ at different simulation times.	56
Figure 22.	Total energy [DPD Units] of the system shown in Figure 21.	57
Figure 23.	Snapshot of the bilayer of C ₁₀ E ₄ at a surfactant concentration of 75wt%.	58
Figure 24.	Experimental phase diagram of C ₁₂ E ₅ in water ³⁰ .	59
Figure 25.	Simulation results at a C ₁₂ E ₅ concentration of (a) 40wt%, (b) 70wt%, and (c) 95wt%.	60
Figure 26.	Simulation results at a C ₁₂ E ₅ concentration of (a) 40wt%, and (b) 70wt%.	60
Figure 27.	Formation of the micellar phase at 40wt% C ₁₂ E ₅ at different simulation times.	61

Figure 28.	Total energy [DPD Units] of the system shown in Figure 27.	62
Figure 29.	Schematic draw of the C ₁₀ E ₄ bilayer.	64
Figure 30.	Snapshot of the C ₁₀ E ₄ micelle at a surfactant concentration of 35wt%.	65
Figure 31.	Schematic representation of the simulation model for C ₁₀ E ₄ (3), water (2) and n-decane (6).	67
Figure 32.	Structure of PEP5-PEO5 (7).	68
Figure 33.	Schematic representation of the simulation model of 7.	68
Figure 34.	Structure of poly (propylene oxide) – <i>block</i> - poly (ethylene oxide) PPO5-PEO5 (8).	69
Figure 35.	DPD-model of poly (propylene oxide) – <i>block</i> - poly (ethylene oxide) PPO5-PEO5 (8).	69
Figure 36.	Pair interaction energies ΔE_{AB} in Jcm ⁻³ for the bead pairs of the C ₁₀ E ₄ , n-decane, water, PEP5-PEO5 and PPO5-PEO5 system.	70
Figure 37.	Experimental phase diagram of C ₁₀ E ₄ in water and n-decane ³⁴ .	73
Figure 38.	Phase separation of water and n-decane at a C ₁₀ E ₄ fraction of $\gamma=7.5\%$ (a) and $\gamma=12.5\%$ (b).	73
Figure 39.	Bicontinuous Phase at a polymer fraction of $\gamma=15\%$. (a) shows the bicontinuous microemulsion phase with water and (b) without.	74
Figure 40.	Bicontinuous Phase at a surfactant fraction of $\gamma=20\%$. (a) shows the bicontinuous microemulsion with water and oil and (b) with water masked and (c) and (d) with oil masked.	75
Figure 41.	Experimental phase diagram of C ₁₀ E ₄ in water and n-decane ³⁵ .	76

Figure 42.	Lamellar L_{α} phase at a $C_{10}E_4$ fraction of $\gamma=30\%$. (a) shows the L_{α} phase with water and oil and (b) with water masked and (c) with oil masked.	77
Figure 43.	Formation of the lamellar L_{α} phase at a $C_{10}E_4$ fraction of $\gamma=30\%$ through the dynamics simulation at different time steps.	78
Figure 44.	Total energy [DPD units] of the system shown in Figure 43.	79
Figure 45.	Experimental phase diagram of $C_{10}E_4$ and PEP5-PEO5 in water and n-decane ³⁴ .	81
Figure 46.	Bicontinuous Phase at a total “surfactant” fraction of $\gamma=10\%$ and a polymer fraction of $\delta=5\%$. (a) shows the bicontinuous microemulsion with water and oil and (b) with water masked and (c) with oil masked.	82
Figure 47.	(a) Water (blue) and oil (white) layers without surfactant. (b) Water and oil layers with the surfactant molecules at the beginning of the calculation.	83
Figure 48.	300 molecules $C_{10}E_4$ with (a) water and oil phase, (b) only water phase and (c) only oil phase visible.	84
Figure 49.	400 molecules $C_{10}E_4$ with (a) water and oil phase, (b) only water phase and (c) only oil phase visible.	85
Figure 50.	400 molecules $C_{10}E_4$, 3 molecules PEP5PEO5 with (a) water and oil phase, (b) only water phase and (c) only oil phase visible.	85
Figure 51.	Comparison of bicontinuous-structures at different concentrations.	86

Figure 52.	Phase structure at a surfactant fraction of $\gamma=10\%$ and a PPO5-PEO5 polymer fraction of $\delta'=5\%$. (a) shows the whole system and (b) the system with water masked and oil masked.	88
Figure 53.	Poly (ethylene butylene)- <i>block</i> -poly (ethylene oxide) (9) with 67 ethylene, 33 butylene and 114 ethylene oxide units.	89
Figure 54.	Schematic representation of the simulation model.	90
Figure 55.	Pair interaction energies ΔE_{AB} in Jcm^{-3} for all bead pairs of the poly ethylene butylene poly ethylene oxide, methyl cyclohexane, water system.	91
Figure 56.	o/w-emulsion at a polymer concentration of 0.12mol% and a water/oil ratio of 8:1.	92
Figure 57.	w/o-emulsion at a polymer concentration of 0.12mol% and a water/oil ratio of 1:8.	93
Figure 58.	Bicontinuous emulsion at a polymer concentration of 0.12mol% and a water/oil ratio of 1:1.	94
Figure 59.	Starting configurations with surfactants (a) at the air/water surface and (b) in the water phase.	95
Figure 60.	Pair interaction energies ΔE_{AB} in Jcm^{-3} for the interaction of air with water and the surfactant molecules.	96
Figure 61.	Simulation results of $C_{10}E_4$ with a concentration below the <i>cmc</i> (100 molecules).	98
Figure 62.	Simulation results of $C_{10}E_4$ with a concentration above the <i>cmc</i> (400 molecules).	98
Figure 63.	Graph of the calculated surface tension of $C_{10}E_4$, $C_{12}E_5$ and $C_{12}E_6$ in DPD units.	99

Figure 64.	Schematic graph of the calculated surface tension of $C_{10}E_4$, $C_{12}E_5$ and $C_{12}E_6$ in DPD units.	100
Figure 65.	Schematic graph of the experimental surface tension of $C_{10}E_4^{10}$, $C_{12}E_5^{11}$ and $C_{12}E_6^{110}$.	100
Figure 66.	Calculated Surface Tension of $C_{10}E_4$ after conversion to physical units.	101

6.7 List of Tables

Table 1.	Possibilities of Coordination numbers Z .	27
Table 2.	Experimental investigation methods of mesophases ⁴ .	37
Table 3.	Structural data of the surfactants $C_{10}E_4$, $C_{12}E_5$ and $C_{12}E_6$. The experimental values are put in parentheses.	66
Table 4.	Comparison of the X-point fraction: Experiment vs. DPD Simulation.	81
Table 5.	Minimum area per Molecule at the air/water surface of $C_{10}E_4$, $C_{12}E_5$ and $C_{12}E_6$. The experimental values are put in parentheses.	103
Table 6.	Variables and constants of DPD unit conversion.	110

7 References.

- ¹ H.-D. Dörfler, *"Grenzflächen und kolloid-disperse Systeme"*, Springer Verlag, Berlin (2002).
- ² M. J. Rosen, *Surfactants and Interfacial Phenomena"*, 2nd Ed., Wiley, New York, (1989).
- ³ D. J. Mitchell, G. J. T. Tiddy, L. Waring, T. Bostock, M. P. McDonald, *J. Chem. Soc. Faraday Trans. I*, (1983), **79**, 975.
- ⁴ R. Nagarajan, *Langmuir*, (2002), **18**, 31.
- ⁵ R. Miller, V. B. Fainerman, H. Möhwald, *J. Colloid Interface Sci.*, (2002), **247**, 193.
- ⁶ P. Alexandridis, U. Olsson, B. Lindman, *Langmuir*, (1998), **14**, 2627.
- ⁷ G. Gompper, D. Richter, R. Strey, *J. Phys.: Condens. Matter*, (2001), **13**, 9055.
- ⁸ G. J. T. Tiddy, *Phys. Rep.*, (1980), **57 (1)**, 3.
- ⁹ C. Tanford, *"Hydrophobic Effect: Formation of Micelles and Biological Membranes"*, 2nd Ed., Krieger Publishing Company, Malabar, (1991).
- ¹⁰ S. J. Marrink, D. P. Tieleman, A. R. van Buuren, H. J. C. Berendsen, *Faraday Discuss.*, (1996), **103**, 1.
- ¹¹ C. E. Fairhurst, S. Fuller, J. Gray, M. Holmes, G. J. T. Tiddy, *"Lyotropic Surfactant Liquid Crystals"* in *"Handbook of Liquid Crystals"*, Vol. 3, Wiley-VCH, Weinheim, (1998).
- ¹² A. Wallqvist, D. G. Covell, *J. Biophys.*, (1996), **1**, 6000.
- ¹³ D. van Belle, S. J. Wodak, *J. Amer. Chem. Soc.*, (1993), **115**, 647.
- ¹⁴ D. Everet, *"Basic Principles of Colloid Chemistry"*, The Royal Society of Chemistry, London, (1998).
- ¹⁵ M. Kahlweit, R. Strey, P. Firman, D. Haase, J. Jen, R. Schomäcker, *Langmuir*, (1988), **4**, 499.

-
- ¹⁶ B. Smit, A. G. Schlijper, L. A. m. Rupert, N. M. van Os, *J. Phys. Chem.*, (1990), **94**, 6933.
- ¹⁷ S. Bandyopadhyay, M. Tarek, M. L. Lynch, M. L. Klin, *Langmuir*, (2000), **16**, 942.
- ¹⁸ R. Allen, S. Bandyopadhyay, M. L. Klein, *Langmuir*, (2000), **16**, 10552.
- ¹⁹ D. Frenkel, B. Smit, "*Dissipative Particle Dynamics*" in "*Understanding Molecular Simulation*", 2nd Ed., Academic Press, San Diego, (2002).
- ²⁰ R. D. Groot, T. J. Madden, *J. Chem. Phys.*, (1998), **108 (20)**, 8713.
- ²¹ N. A. Spanley, *Europhys. Lett.*, (2000), **49 (4)**, 534.
- ²² C. M. Wiljmans, B. Smit, R. D. Groot, *J. Chem. Phys.*, (2001), **114 (17)**, 7644.
- ²³ S.-L. Yuan, Z.-T. Cai, G.-Y. Xu, Y.-S. Jiang, *Colloid Polym Sci*, (2003), **281**, 1069.
- ²⁴ R. D. Groot, *Langmuir*, (2000), **16**, 7493.
- ²⁵ E. Ryjkina, H. Kuhn, H. Rehage, F. Müller, J. Peggau, *Angew. Chem. Int. Ed.*, (2002), **41 (6)**, 983.
- ²⁶ K. Malka, S. Schlick, *Macromolecules*, (1997), **30**, 456.
- ²⁷ P. Alexandridis, U. Olsson, B. Lindman, *Macromolecules*, (1995), **28**, 7700.
- ²⁸ J. C. Lang, R. O. Morgan, *J. Chem. Phys.*, (1980), **73 (11)**, 5849.
- ²⁹ C. Stubenrauch, S. Burauer, R. Strey, *Liquid Crystals*, (2004), **31 (1)**, 39.
- ³⁰ A. Tonegawa, K. Ohno, H. Matsuura, K. Yamada, T. Okuda, *J. Phys. Chem. B*, (2002), **106**, 13211.
- ³¹ B. Medhage, M. Almgren, J. Asins, *J. Phys. Chem.*, (1993), **97**, 7753.
- ³² K. Sharma, C. Rodgers, R. M. Palepu, A. K. Rakshit, *J. Colloid Interface Sci.*, (2003), **268**, 482.
- ³³ R. Strey, R. Schomäcker, D. Roux, F. Nallet, U. Olsson, *J. Chem. Soc. Faraday Trans. I*, (1990), **86**, 2253.
- ³⁴ B. Jakobs, T. Sottmann, R. Strey, J. Allgaier, L. Willner, D. Richter, *Langmuir*, (1999), **15**, 6707.
- ³⁵ C. Stubenrauch, C. Frank, R. Strey, *Langmuir*, (2002), **18 (13)**, 5027.
-

- 36 R. Strey, unpublished results.
- 37 J. Venzmer, Degussa company, research department.
- 38 S. Yamamoto, Y. Maruyama, S.-a. Hyodo, *J. Chem. Phys.*, (2002), **116 (13)**, 5842.
- 39 S. Yamamoto, S.-a. Hyodo, *Polym. J.*, (2003), **35 (6)**, 519.
- 40 M. Venturoli, B. Smit, *Phys. Chem. Comm.*, (1999), **10**, 45.
- 41 L. Rekvig, M. Kranenburg, J. Vreede, B. Hafskjold, B. Smit, *Langmuir*, (2003), **19**, 8195.
- 42 L. Rekvig, M. Kranenburg, B. Hafskjold, B. Smit, *Europhys. Lett.*, (2003), **63 (6)**, 902.
- 43 L. Rekvig, B. Hafskjold, B. Smit, *J. Chem. Phys.*, (2004), **120 (10)**, 4897.
- 44 A. Maiti, S. McGrother, *J. Chem. Phys.*, (2004), **120 (3)**, 1594.
- 45 F. Goujon, P. Malfreyt, S. J. Tildesley, *Chem. Phys. Chem.*, (2004), **5**, 457.
- 46 W. Dzwinel, D. A. Yuen, *Int. J. Mod. Phys. C.*, (2000), **11 (1)**, 1.
- 47 J. B. Gibson, K. Chen, S. Chynoweth, *J. Colloid Interface Sci.*, (1998), **206**, 464.
- 48 W. Dzwinel, W. Alda, *Int. J. Modern. Phys. C*, (2000), **25 (6)**, 361.
- 49 W. Dzwinel, D. A. Yuen, *Int. J. Modern. Phys. C*, (2000), **11 (5)**, 1037.
- 50 P. Español, *Europhys. Lett.*, (1997), **39 (6)**, 605.
- 51 P. Español, M. Serrano, *Int. J. Modern. Phys. C*, (1997), **8 (4)**, 899.
- 52 E. G. Flekkøy, P. Coveney, G. de Fabritiis, *Phys. Rev. E*, (2000), **62 (2)**, 2140.
- 53 J. Koelman, P. Hoogerbrugge, *Europhys. Lett.*, (1993), **21**, 363.
- 54 P. Hoogerbrugge, J. Koelman, *Europhys. Lett.*, (1992), **19**, 155.
- 55 S. Jury, P. Blandon, M. Cates, S. Krishna, M. Hagen, N. Ruddock, P. Warren, *Phys. Chem. Chem. Phys.*, (1999), **1**, 2051.
- 56 P. Español, *Phys. Rev. E.*, (1996), **53 (2)**, 1572.
- 57 P. Español, P. Warren, *Europhys. Lett.*, (1995), **30**, 191.

-
- 58 W. H. Press, S. A. Teukolsky, W. T. Vetterling, B. P. Flannery, *"Numerical recipes in C, The Art of Scientific Computing"*, Cambridge University Press, 2nd Ed., London, UK, (1992).
- 59 D. Fincham, D. M. Heyes, *CCP5 Quarterly*, (1982), 6410.
- 60 N. S. Martys, R. D. Mountain, *Phys. Rev. E*, (1999), **59 (3)**, 3733.
- 61 C. A. Marsh, J. M. Yeomans, *Europhys. Lett.*, (1997) **37 (8)**, 511.
- 62 R.D. Groot and P.B. Warren, *J. Chem. Phys.*, (1997), **107**, 4423.
- 63 K. E. Novik, P. V. Coveney, *J. Chem. Phys.*, (1998), **109 (18)**, 7667.
- 64 M. P. Allen, D. J. Tildesley, *"Computer Simulations of Liquids"*, Oxford University Press, (2002).
- 65 H. Stetter, *"Analysis of discretization methods for ordinary differential equations"*, Springer, Berlin (1973).
- 66 W. K. den Otter, J. H. R. Clarke, *J. Mod. Phys. C.*, (2000), **11**, 1179.
- 67 J. P. R. B. Walton, d. J. Tildesley, J. S. Rowlinson, J. R. Henderson, *Mol. Phys.*, (1983), **48**, 1357.
- 68 R. D. Groot, K. L. Rabone, *Biophys. J.*, (2001), **81**, 725.
- 69 B. M. Forest, U. W. Sutter, *J. Chem. Phys.*, (1995), **102 (18)**, 7256.
- 70 P. Flory, *"Principles of Polymer Chemistry"*, Cornell University Press, Ithaca, New York, (1953).
- 71 J. Bicerano, *"Prediction of Polymer Properties"*, Marcel Dekker, 2nd, New York, (1996).
- 72 C. Fan, B. Olafson, M. Blanco, H. Hsu, *Macromolecules*, (1992), **25**, 3667.
- 73 H. Sun, *J. Phys. Chem. B*, (1998), **102**, 7338.
- 74 H. Sun, D. Rigby, *Spectrochimica Acta (A)*, (1998), **53**, 1301 B.
-

-
- 75 H. Sun, P. Ren, J. R. Fried, *Computational and Theoretical Polymer Sci.*, (1998), **8**
(1/2), 229.
- 76 M. Blanco, *J. Comput. Chem.*, (1991), **12**, 237.
- 77 S. H. Jacobson, D. J. Gordon, G. V. Nelson, A. Balazs, *Adv. Mat.*, (1992), **4**, 198.
- 78 U. Burtkert, N. L. Allinger, "*Molecular Mechanics*", American Chemical Society,
Washington DC, (1982).
- 79 F. Jensen, "*Introduction to Computational Chemistry*", Wiley, (1999).
- 80 J. E. Lennard-Jones, *Proc. Roy. Soc.*, (1924), **106**, A463.
- 81 G. R. McNamara, G. Zanetti, *Phys. Rev. Lett.*, (1988), **61**, 2332.
- 82 R. Benzi, S. Succi, M. Vergassola, *Phys. Rep.*, (1992), **222**, 145.
- 83 S. Chen, G. D. Doolen, *Ann. Rev. Fluid Mech.*, (1998), **30**, 329.
- 84 U. Frisch, B. Hasslacher, Y. Pomeau, *Phys. Rev. Lett.*, (1986), **56**, 1505.
- 85 P. J. Love, P. V. Coveney, B. M. Boghosian, *Phys. Rev. E.*, (2001), **64**, 021503.
- 86 S. F. Edwards, M. Muthukumar, *Macromolecules*, (1984), **17**, 586.
- 87 D. L. Ermak, "*Brownian Dynamics techniques and their application to dilute
solutions*", Rapport d'activité scientifique du CECAM, (1976), p. 66.
- 88 D. L. Ermak, H. Buckholtz, *J. Comput. Phys.*, (1980), **35**, 169.
- 89 S. He, H. A. Scheraga, *J. Chem. Phys.*, (1998), **108**, 271.
- 90 R. D. Groot, T. J. Madden, D. J. Tildesley, *J. Chem. Phys.*, (1999), **110** (19), 9739.
- 91 P. C. Hohenberg, B. I. Halperin, *Rev. Mod. Phys.*, (1977), **49**, 435.
- 92 M. Chaikin, T. C. Lubensky, "*Principles of Condensed Matter Physics*",
(1994)Cambridge University Press, Cambridge, 464.
- 93 B. A. C. van Vlimmeren, J. G. E. M. Fraaije, *Comp. Phys. Comm.*, (1996), **99**, 21.
- 94 N. M. Maurits, J. G. E. M. Fraaije, *J. Chem. Phys.*, (1997), **106** (16), 6730.
-

- ⁹⁵ J. G. E. M. Fraaije, B. A. C. van Vlimmeren, N. M. Maurits, M. Postma, O. A. Evers, C. Hoffmann, P. Altevogt, G. Goldbeck-Wood, *J. Chem. Phys.*, (1997), **106** (8), 4160.
- ⁹⁶ N. M. Maurits., J. G. E. M. Fraaije, *J. Chem. Phys.*, (1997), **107** (15), 5879.
- ⁹⁷ N. M. Maurits, B. A. C. van Vlimmeren, J. G. E. M. Fraaije, *Phys. Rev. E.*, (1997), **56** (1), 816.
- ⁹⁸ B. A. C. van Vlimmeren, N. M. Maurits, A. V. Zvelindovsky, G. J. A. Sevink, G. E. M. Fraaije, *Macromolecules*, (1999), **32**, 646.
- ⁹⁹ S. L. Guo, T. J. Hou, X. J. Xu, *J. Phys. Chem. B*, (2002), **106**, 11397.
- ¹⁰⁰ D. W. Krevelen, *"Properties of Polymers: Their Correlation with chemical Structure, Their Numerical Estimation and Prediction from Additive Group Contributions"*, (1990), 3rd Ed. Elsevier, Amsterdam.
- ¹⁰¹ A. F. Barton, *"Handbook of Solubility Parameters and Other Cohesion Parameters"*, (1983), CRC Press, Boca Raton, FL.
- ¹⁰² P. Alexandridis, D. Zhou, A. Khan, *Langmuir*, (1996), **12**, 2690.
- ¹⁰³ A. Caragheorghopol, H. Caldaran, I. Dragutan, H. Joela, W. Brown, *Langmuir*, (1997), **13**, 6912.
- ¹⁰⁴ Y. N. Degtyarev, S. Schlick, *Langmuir*, (1999), **15**, 5040.
- ¹⁰⁵ K. Zhang, A. Khan, *Macromolecules*, (1995), **28**, 3807.
- ¹⁰⁶ P. Alexandridis, U. Olsson, B. Lindman, *J. Phys. Chem.*, (2003), **100**, 280.
- ¹⁰⁷ R. Ianova, B. Lindman, P. Alexandridis, *Langmuir*, (2000), **16**, 3660.
- ¹⁰⁸ P. Alexandridis, R. Ianova, B. Lindman, *Langmuir*, (2000), **16**, 3676.
- ¹⁰⁹ R. Strey, *Chem. Tech. Lab.*, (1992), **40**, 213.
- ¹¹⁰ Y. J. Nikas, S. Puvvada, D. Blankshtein, *Langmuir*, (1992), **8**, 2680.

References

- ¹¹¹ M. J. Rosen, A. W. Cohen, M. Dahanayake, X.-Y. Hua, *J. Phys. Chem.*, (1982), **86**, 541.
- ¹¹² R. D. Groot, *J. Chem. Phys.*, (2003), **118 (24)**, 11265.

Curriculum Vitae

Sarah Gwendolyn Schulz

Nationality: German

Date and Place of Birth: February 10 1978, Duisburg, Germany

Work Experience

January 2003 – Present

*AICove -Molecular Dynamics- GmbH, Gladbeck,
Germany*

Research Scientist

Responsible for the implementation of the project “Specific Property Adjustment of Siloxanes and Polymers with Dissipative Particle Dynamic und Molecular Dynamics Simulations“ for the Degussa AG, Essen, Germany.

April 2001 – September 2001

McMaster University, Hamilton, Ontario, Canada

Summer Student

Physical organic chemistry

Supervisor: Prof. Nick H. Werstiuk, PhD

Independent research on the preparation and experimental as well as simulated ultraviolet photoelectron spectroscopy of bicyclo[4.2.0]oct-7-en-2-one.

January 1999 – June 2000

Schülerhilfe, Heiligenhaus, Germany

Part-Time Coaching Teacher

Coaching and tutorials for high-school students age 10 to 19. Teaching in groups of 3 to 6 students in Mathematics, Physics and Chemistry.

Education

November 2002 – Present

University Duisburg-Essen, Campus Essen

Ph.D. Student in Chemistry

Supervisors: Dr. Hubert Kuhn, Prof. Dr. Günter Schmid

Industry Scholarship from AlCove -Molecular Dynamics- GmbH, Gladbeck, Germany

Working as a theoretical chemist with various simulation methods like Dissipative Particle Dynamics (DPD), Molecular Dynamics (MD), Molecular Mechanics (MM), Monte Carlo (MC) and Quantum Mechanics (QM). Application of these methods to investigate phase behavior, self-assemblies, formation of microemulsions and surface properties of amphiphilic polymers and surfactants.

October 1997 – September 2002

Gerhard-Mercator-University Duisburg

Diplom Chemie

Diplom Chemiker Degree in Chemistry (1.3).

Thesis in Theoretical Chemistry:

Supervisor: Prof. Volker Buß, PhD

"CASPT2-Calculations of the Stability and the Spectroscopic Properties of Chiral Cyclohexadienes"

Involved *ab initio* calculations of the UV/VIS- and Circular Dichroism Spectra with the new CASPT2 method.

September 2000 - April 2001

Master University, Hamilton, Ontario, Canada

Full-time exchange student in Chemistry

DAAD-scholarship

Senior Thesis (A):

Supervisor: Prof. Nick H. Werstiuk, PhD

“The Preparation and Ultraviolet Photoelectron Spectroscopy of Transient Strained Cyclic Cumulenes”

Simulation of photoelectron spectra with *ab initio* methods and experimental ultraviolet photoelectron spectra. Involved synthesis and purification (HPLC, GC) of strained cyclic cumulenes and subsequent NMR studies of compounds synthesized. Included computational investigation of the topology of the electron density of the cyclic cumulenes with Bader's theory Atoms in Molecules (AIM). Project included Organic Chemistry, Physical Chemistry and Theoretical Chemistry.

August 1988 – June 1997

Immanuel-Kant-Gymnasium ,Heiligenhaus

Abitur (2.2)

August 1984 – July 1988

Wilhelm-Busch-Grundschule, Ratingen-Hösel

Awards

September 29 2003

Poster Prize Award

Bayreuth Polymer Symposium 03 (BPS03),
41. Hauptversammlung der Kolloidgesellschaft,
Bayreuth, Germany
„The Phase Behavior of Amphiphilic Polymers: A
Dissipative Particles Dynamics Study“

May 19 2004

Presentation Award

18. Darmstädter Molecular Modeling Workshop
Computer-Chemie-Centrum Erlangen, Germany
“Dissipative Particle Dynamics – Simulations of
Phospholipid Structures”

Publications

Sarah G. Schulz, Ulf Frieske, Hubert Kuhn, Günter Schmid, Reinhard Strey, Felix Müller, Christian Mund, Joachim Venzmer

"Dissipative Particle Dynamics Simulation of Mesophases."

Phys. Chem. Chem. Phys. (2004), *submitted*

Sarah G. Schulz, Ulf Frieske, Hubert Kuhn, Günter Schmid, Felix Müller, Christian Mund, Joachim Venzmer

" The Simulation of the Self-Assembly and Surface Tension of the Non-Ionic Surfactant C10E4, C12E5 and C12E6 with Dissipative Particle Dynamics."

Langmuir (2004), *submitted*

S. G. Schulz, U. Frieske, H. Kuhn, G. Schmid, F. Müller, C. Mund, J. Venzmer

"Mesoscale Computer Simulations on the Phase Behavior of the Non-Ionic Surfactant C12E5"

Tenside Surfactants Detergents, **41 5** (2004), 230

S. G. Schulz, H. Kuhn, G. Schmid, C. Mund, J. Venzmer

„The Phase Behavior of Amphiphilic Polymers: A Dissipative Particle Dynamics Study.“

Colloid and Polymer Science (2004), published online October 9th 2004, *in press*

S. G. Schulz, H. Kuhn, G. Schmid

„Molecular Modeling Computer Simulations of Organic Polymers: A Novel Computer Simulation Technique to Characterize Nanostructured Materials.“

Mat. Res. Soc. Symp. Proc., **Vol. 788** (2004), L10.5, 635

S. G. Schulz, H. Kuhn, F. Müller

„A Novel Computer Simulation Technique to Characterize Microemulsions – A Dissipative Particle Dynamics Study“

Jorn. Comp. Esp. Deterg., **34** (2004), 113

S. G. Schulz, H. Kuhn

„Computer Simulations of Shampoos, Crèmes and Detergents”

Asia Pacific Personal Care Magazine, January 2004

Poster

September 27 2004

„Auftragsforschung Molecular Modeling in der chemischen Industrie“

Dechema Workshop “Molecular Modelling für chemisch-technische Anwendungen”, Frankfurt am Main, Germany

September 29 2003

„The Phase Behavior of Amphiphilic Polymers: A Dissipative

Particles Dynamics Study“

Poster Prize Award

Bayreuth Polymer Symposium 03 (BPS03),

41. Hauptversammlung der Kolloidgesellschaft, Bayreuth, Germany

May 27 2003

„Molecular Modeling Computer Simulations of Polymers: Dissipative Particle Dynamics Study of Interfacial Properties of Diblock Copolymers“

17. Darmstädter Molecular Modeling Workshop
Computer-Chemie-Centrum Erlangen, Germany

Lectures

*November 25 2004**

“The Application of Dissipative Particle Dynamics in Industrial Research”

Georg-Simon-Ohm Fachhochschule Nürnberg,
Nürnberg, Germany

November 17 2004

“Dissipative Partikel Dynamik: Eine mesoskopische Methode zur Simulation von Polymerstrukturen”

Arbeitskreis “Computersimulation an
Polymerwerkstoffen”

Deutsches Kunststoff Institut, Darmstadt, Germany

*July 1 2004**

“An Introduction to Dissipative Particle Dynamics – Theory, Examples and Applications”

Institut Européen des Membranes, Montpellier,
France

*June 28 2004**

“Results of Nanoscale Coarse-Grained Simulations with DPD”

BASF AG, Polymer Physics, Ludwigshafen,
Germany

June 23 2004

“Molecular Modeling Simulations of Polymers: A Novel Technique to Characterize Nanostructures.”

6th World Surfactants Congress, CESIO 2004, Berlin,
Germany

* Invited Lectures

- May 19 2004*** “Dissipative Particle Dynamics – Simulations of Phospholipid Structures”
Presentation Award 18. Darmstädter Molecular Modeling Workshop
Computer-Chemie-Centrum Erlangen, Germany
- April 30 2004*** “Dissipative Particle Dynamics Study of Surfactants: A Novel Computer Simulation Technique to Develop New Detergents and Formulations.”
18. Vortragstagung der GDCh-Fachgruppe
Waschmittelchemie, Königswinter, Germany
- March 25 2004*** “A Novel Computer Simulation Technique to Characterize Microemulsions: A Dissipative Particle Dynamics Study.”
CED Annual Meeting, Barcelona, Spain
- February 10 2004*** “Investigation of Microemulsion Systems With Dissipative Particle Dynamics.”
Wissenschaftliches Kolloquium der Arbeitsgruppe
von Prof. Strey, Physikalische Chemie, Universität
Köln, Germany
- February 5 2004**** “A Dissipative Particle Dynamics Study: The Prediction of the Self-Assembly of Amphiphilic Polymers.”
Forschungszentrum Jülich GmbH, Institut für
Festkörper-forschung; Jülich, Germany

* Invited Lectures

- December 8 2003**** “A Dissipative Particle Dynamics Study of the Self-Assembly of Organic Polymers”
Chemistry Department Seminar, McMaster University, Hamilton, ON, Canada
- December 4 2003*** “Molecular Modeling Computer Simulations of Organic Polymers: A Novel Computer Simulation Technique to Characterize Nanostructured Materials.”
Materials Research Society (MRS) Fall Meeting 2003, Boston, MA, USA
- September 25 2003**** “Einsatz neuer Molecular Modeling Techniken bei der Erforschung und Entwicklung von Polymeren in der Industrie.”
Wirtschaftsforum 10 – Anwendung von Computer unterstütztem Molekül-Design (CAMD) in der Industrie, Universität Duisburg-Essen, IHK zu Essen, Essen, Germany
- September 2 2003**** „The Chemical-Technical Application of Surfactants with Special Regards to Molecular Chemistry”
Cosmetic & Household Ingredients Exhibition, Moscow, Russia
- May 19 2003**** „Development of New Surfactants with Mesoscopic Computer simulations“
University Duisburg-Essen Stand Presentation, Achema 2003, Frankfurt, Germany

* Invited Lectures

May 16 2003**

„Dissipative Particle Dynamic-Simulations of Microemulsions“

Kolloquium of the Graduiertenkolleg „Structure-Dynamic-Relations in Microstructured Systems“, Universität Dortmund, Germany

April 14 2003

„Dissipative Particle Dynamic Simulations of the Phase Behavior of Amphiphilic Polymers“

Status seminar of the project „Gezielte Eigenschaftseinstellung von Siloxanen und Polymeren durch Dissipative Partikel Dynamik und Molekül Dynamik Simulationen“, degussa AG, Essen, Germany

January 31 2003

“Calculation of Phase Properties of Amphiphilic Polymers Using a New Molecular Modeling Technique”

University Duisburg-Essen FET, Workshop Interdisciplinary Material Sciences Seminar, Geldern, Germany

March 17 2001

“The Preparation and Ultraviolet Photoelectron Spectroscopy of Transient Strained Cyclic Cumulenes”

Chemistry 4G06 Seminars, McMaster University, Hamilton, Ontario, Canada

* Invited Lectures

Selbständigkeitserklärung

Hiermit erkläre ich, dass ich bei der Ausarbeitung der beigefügten Dissertation „The Phase Behavior of Amphiphilic Surfactants and Polymers: A Dissipative Particle Dynamics Study“ keine anderen als die angegebenen Mittel benutzt habe und das wörtlich übernommene Ausführungen als solche gekennzeichnet sind.

Sarah Gwendolyn Schulz

Essen den 17. Dezember 2004
